Earth and Planetary Sciences ETDs

Electronic Theses and Dissertations

6-1-2011

Formation conditions of plagioclase-bearing type I chondrules in CO chondrites : a study of natural samples and experimental analogs

Molly Wick

Follow this and additional works at: https://digitalrepository.unm.edu/eps_etds

Recommended Citation

Molly J. Wick

Candidate

DEPARTMENT OF EARTH AND PLANETARY SCIENCE

Department

This thesis is approved, and it is acceptable in quality and form for publication:

Approved by the Thesis Committee:

Rhian Jones,
Chairperson

Adrian Brearley

Jane Selverstone

Charles Shearer

Formation Conditions of Plagioclase-bearing Type I Chondrules in CO Chondrites: A Study of Natural Samples and Experimental Analogs

BY

Molly J. Wick

B.S., Geology, University of Minnesota, 2008

THESIS

Submitted in Partial Fulfillment of the
Requirements for the Degree of

Master of Science

Earth and Planetary Science

The University of New Mexico
Albuquerque, New Mexico

August, 2010

ACKNOWLEDGMENTS

Formation Conditions of Plagioclase-bearing Type I Chondrules in CO Chondrites: A Study of Natural Samples and Experimental Analogs

BY

Molly J. Wick

ABSTRACT OF THESIS

Submitted in Partial Fulfillment of the
Requirements for the Degree of

Master of Science

Earth and Planetary Science

The University of New Mexico
Albuquerque, New Mexico

August, 2010

Formation Conditions of Plagioclase-bearing Type I Chondrules in CO Chondrites:

A Study of Natural Samples and Experimental Analogs

by

Molly J. Wick

B.S., Geology, University of Minnesota, 2008

M.S., Earth and Planetary Sciences, University of New Mexico, 2010

ABSTRACT

Chondrites are samples from undifferentiated asteroids that contain components that formed in the early solar system. One of the components found in chondrites is chondrules, which are small igneous spherules that formed from the melting of precursor dust ball assemblages during very short, high-temperature events in the solar nebula. Chondrules typically contain olivine and pyroxene, a glassy mesostasis, Fe-Ni metal, and sulfides. Type I chondrules contain FeO-poor and volatile-poor mineral assemblages. Approximately 10% of type I chondrules, including type IA, IAB, and IB textures, also contain igneous plagioclase. While dynamic cooling experiments have put constraints on the formation conditions of chondrules based on olivine and pyroxene textures and morphologies, plagioclase has not been produced in previous experimental chondrule analogs. In this study, we investigated common chondrule textures in CO chondrites and determined mineral and bulk compositions for plagioclase-bearing type I chondrules in CO chondrites. We also performed one-atmosphere dynamic cooling experiments in order to establish formation conditions for type I chondrules. We attempted to optimize

conditions for plagioclase nucleation and growth by conducting experiments at slow cooling rates, low quench temperatures, in the presence of a Na-rich atmosphere, and with anorthite seeds present in the starting material. Experimental run products closely resemble textures of type I chondrules in ordinary and carbonaceous chondrites. Olivine is commonly poikilitically enclosed in euhedral low-Ca pyroxene. Ca-pyroxene appears as overgrowths on larger low-Ca pyroxene grains. Compositions of olivine, pyroxene, and mesostasis from experimental charges are also very similar to those observed in natural chondrules. Therefore, peak temperatures (1500 - 1600°C) and slow cooling rates (5 - 25°C/hr) used are plausible conditions for type I chondrule formation. These conditions are also predicted by the shock wave model for chondrule formation. While our experiments were conducted at conditions that we considered optimized for plagioclase crystallization, plagioclase was not observed in any experiment. Defining the conditions necessary for plagioclase nucleation may place important constraints on chondrule thermal histories.

TABLE OF CONTENTS

LIST OF FIGURES

LIST OF TABLES

CHAPTER 1:

INTRODUCTION

Chondrules, the major component of chondrites, are an invaluable source of information about the conditions that prevailed where and when the components of chondrites formed in the solar nebula, 4.6 billion years ago. Chondrules are millimeter-sized igneous spherules that formed during very short, high-temperature events that melted dust aggregates in the solar nebula. By studying the textures and crystallization history of chondrules, valuable information can be gained about conditions of chondrule formation such as peak temperatures, cooling rates, oxygen fugacity, and precursor chemistry.

The main constituents of chondrules are olivine, pyroxene, metal, sulfides, and a glassy mesostasis. Approximately ten percent of chondrules in the Ornans-like carbonaceous chondrite group (CO chondrites) contain igneous plagioclase grains as well. However, plagioclase has not been reproduced experimentally (e.g., Lofgren, 1989). Its presence could put significant constraints on how chondrules formed. In this study, we describe common chondrule textures in CO chondrites and mineral and bulk compositions for plagioclase-bearing type I chondrules in CO chondrites. We have also conducted dynamic cooling experiments for the purpose of constraining conditions under which common porphyritic textures are formed in type I chondrules in CO chondrites, and examined the conditions under which igneous plagioclase crystallizes in a chondrule-forming setting. Overall, this study contributes to a better understanding of conditions that prevailed in the early solar nebula.

Overview of the geologic processes recorded by chondrites

The solar system was formed by the gravitational collapse of a dust-rich molecular cloud. Figure 1 shows current ideas about processes that occurred in the protoplanetary disk (or solar nebula) that surrounded the Sun during the early stages of solar system formation. The disk was turbulent and probably lasted for a few million years. During this time, Ca- and Al-rich inclusions (CAIs) were some of the first materials to condense out of the solar nebula in the hot region very close to the Sun. CAIs contain minerals (corundum, hibonite, perovskite, grossite, melilite, etc.) that are predicted to condense in an equilibrium condensation sequence at the temperature and pressure of the solar nebula (Brearley and Jones, 1998). Subsequent to their formation, CAIs were then transported by disk winds away from the Sun, and then fell back into the chondrule-forming region in the midplane of the disk.

Figure 1: Generalized figure of processes occurring in the early solar system. After Scott & Krot, 2005.
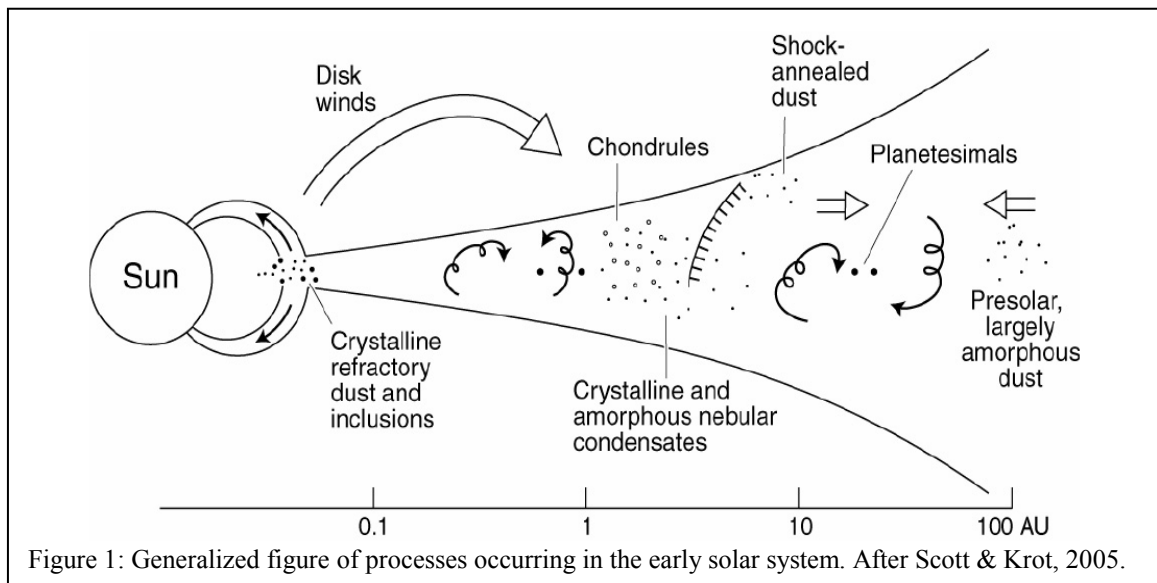
Formation of chondrules, sub-millimeter-sized spherical objects, occurred about 2 million years after CAI formation (Kita et al., 2000). Chondrules were likely a major

constituent of nebular solids in the inner solar system, as they represent 15 to 80 volume percent of chondrite meteorites (Brearley & Jones, 1998). Chondrules formed from precursor dust ball assemblages during very short, high-temperature events in the solar nebula. These events occurred over a period of at least 1.3 million years, based on Pb-Pb dating of CR chondrules (Amelin et al., 2002). The most likely cause of chondrule-forming events is the passage of a shock front through dense regions of nebular dust at distances greater than 1AU from the sun (e.g. Desch and Connolly, 2002; Connolly and Love, 1998). The ambient pressure of the nebula in the regions where chondrules and CAIs formed was probably about 10^{-6} to 10^{-3} bars (Alexander et al., 2008).

Chondrules and CAIs, along with other nebular condensates and dust were accreted into small planetesimals of a few kilometers in diameter, the largest of which would experience runaway growth from accumulation of local material in their "feeding zones" (Chambers, 2004). This planetesimal formation occurred over a time as short as 0.1 to 1 Myr. As planetesimals grew larger, gravitational interactions among planetesimals resulted in a chaotic scattering of bodies at increasing velocities. The presence of the asteroid belt as opposed to the presence of a planet in the region currently separating the terrestrial planets from the gas giants, was probably due to gravitational interactions with Jupiter. As larger bodies accreted, they would inevitably enter unstable orbital resonances with Jupiter or Saturn, and gravitational interactions would then send the body flying either into the inner solar system towards the Sun or out of the solar system, prohibiting the formation of one planet in that region. The resulting configuration of the solar system, which was in place by 5 Myr to 100 Myr after initial gravitational

collapse of the protosun, is the result of the survival of the largest planetesimals and chance gravitational interactions with Jupiter and Saturn.

Some bodies in the asteroid belt melted and differentiated, resulting in bodies that have a silicate mantle and an iron metal core. Heat sources for this process include heat generated by impacts and the decay of short-lived radiogenic nuclides present in the early solar system, such as ^{26}Al. Hafnium-tungsten dating of differentiated meteorites indicates that metal-silicate separation of all differentiated bodies was completed within 30 Myr after CAI formation (e.g. Yin et al., 2002; Kleine et al., 2002), and differentiation of smaller bodies hundreds of km in diameter requires much less time (Kleine et al., 2002). Hafnium-tungsten dating of iron meteorites gives an age of core formation for some asteroids of ~1.5 Myr after CAI formation (Kleine et al., 2005). Hence, the early stages of planetary accretion occurred while chondrule formation was still occurring.

Accretion of material at later stages resulted in the formation of parent bodies that never experienced enough heat to melt, perhaps because less heat was available after much of the short-lived radiogenic nuclide decay had already occurred (Kunihiro, et al., 2003). Undifferentiated meteorites (chondrites) are derived from such bodies. Geologic processing on chondrite parent bodies included thermal metamorphism, aqueous alteration, or both, within a few tens of million years after accretion (Brearley & Jones, 1998). These secondary processes, as well as processes that occurred before chondrite accretion, are recorded in the mineralogy, textures, and isotopic compositions of chondrite components.

Since the early stages of solar system formation, asteroids have continuously experienced both collisions and gravitational interactions with the gas giant planets, which altered their orbital paths. Some of this material encounters the orbital path of Earth, where it falls as meteorites. For CO chondrites, such collisions occurred around 20 – 50 million years ago (Scherer & Schultz, 2000). By studying the physical and chemical properties of these meteorites, we can determine conditions (such as temperature, pressure, oxygen fugacity, composition of dust, isotopic heterogeneities, etc.) that prevailed in the early solar nebula, as well as the conditions of alteration that chondrites experienced subsequent to solar system formation.

Chondrite classification

Chondrites are classified according to their chemical and physical properties. Figure 2 shows a current representation of the classification of chondrites, which are divided into three main classes: carbonaceous, ordinary, and enstatite. Chondrite classes are defined according to properties that include average refractory lithophile element to Si abundance ratios of bulk chondrites, bulk chondrite oxygen isotope compositions, refractory inclusion abundances, and matrix to chondrule abundance ratios (Krot et al., 2003). Chondrite groups are classified based on the relative abundances and sizes of chondrite components: chondrules, FeNi-metal, calcium-aluminum-rich inclusions (CAIs), amoeboid olivine aggregates, and matrix (Krot et al., 2003). Chondrites in a given group tend to have similarly sized components. Average chondrule size varies from 0.02 to 1 mm from group to group. CAIs in different groups also have varying compositions. For example, in CV chondrites, plagioclase-pyroxene-rich CAIs are

common, while they are rare or absent in other types of chondrites (Scott & Krot, 2003). Chondrite groups are also classified based on chemical composition and chemical properties (Krot et al., 2003).

Figure 2: Chondrite classification scheme. After Weisberg et al., 2006.
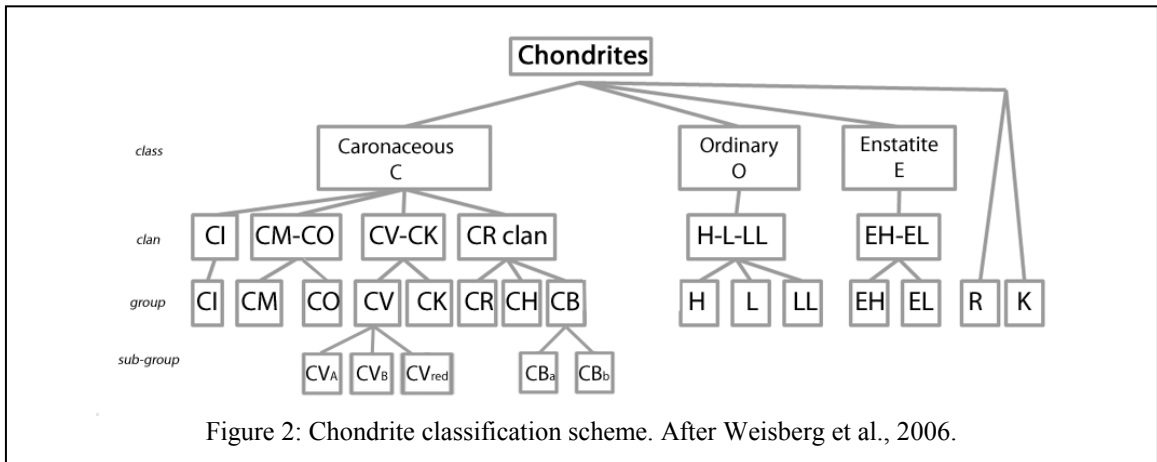
Bulk compositions of all chondrites are similar to the composition of the solar photosphere, with varying depletions in volatile and moderately volatile elements, depending on the group. Each group's elemental abundance pattern is unique and well constrained. For example, relative to CI chondrites, which have the closest bulk composition to the solar photosphere, carbonaceous chondrites are enriched in refractory lithophile elements and depleted in volatile elements. In addition to bulk elemental abundance patterns, there are isotopic signatures within each group associated with oxygen as well as nitrogen and for some chondrite groups, carbon. The oxygen isotopic compositions plotted on a three-isotope diagram show a distinct range for each chondrite group, though some ranges do overlap. Oxidation states of various chondrite groups are also well defined and vary among groups (Krot et al., 2003).

The differences among chondrite groups could be attributed to compositional heterogeneities in the solar nebula during formation of chondrite components. For example, formation of a chondrite component (CAI, chondrule, etc) of a given size, texture, and composition requires specific conditions in the solar nebula. To create the wide variety of these properties that is observed requires heterogeneous conditions and compositions throughout the solar nebula where they formed. Because we see these variations from chondrite group to chondrite group, heterogeneities must have persisted to the time when asteroids accreted.

It is important when studying chondrites to distinguish between nebular processes that formed the components of chondrites and the planetary processes that subsequently altered chondrites. Chondrite parent bodies experienced different amounts of alteration since accretion, including thermal metamorphism and aqueous alteration. The degree and type of alteration is described in terms of petrologic type (Van Schmus & Wood, 1967). If a chondrite has been thermally metamorphosed, its petrologic type describes the extent of metamorphism, increasing from petrologic type 3 to petrologic type 6. This thermal metamorphism could have also been associated with the presence of fluids. If a chondrite has been aqueously altered, its petrologic type decreases with increasing alteration, from 3 down to petrologic type 1. A specimen that is very minimally altered has a petrologic type of 3, and is considered the most primitive, or the most representative of nebular materials.

This study focuses on CO chondrites, which are a group of largely unequilibrated (not thermally metamorphosed) carbonaceous chondrites. While all CO chondrites are

petrologic type 3, they experienced different degrees of thermal metamorphism on their

parent body, and range in petrologic subtype from 3.0 to 3.8 (e.g., Scott and Jones, 1990;

Chizmadia et al., 2002). During thermal metamorphism, FeO and MgO were redistributed

throughout CO chondrites. The petrologic subtypes of meteorites are determined by the

extent of this exchange. In addition, CO chondrites experienced metasomatism, i.e.

reaction with a Na-rich fluid, which resulted in the replacement of primary plagioclase

and chondrule mesostasis glass by nepheline (nephelinization) (Figure 3). This is likely to

have occurred on the parent body, as the grain size and occurrence of secondary nepheline

in CO chondrites correlates with petrologic subtype (Tomeoka & Itoh, 2004).
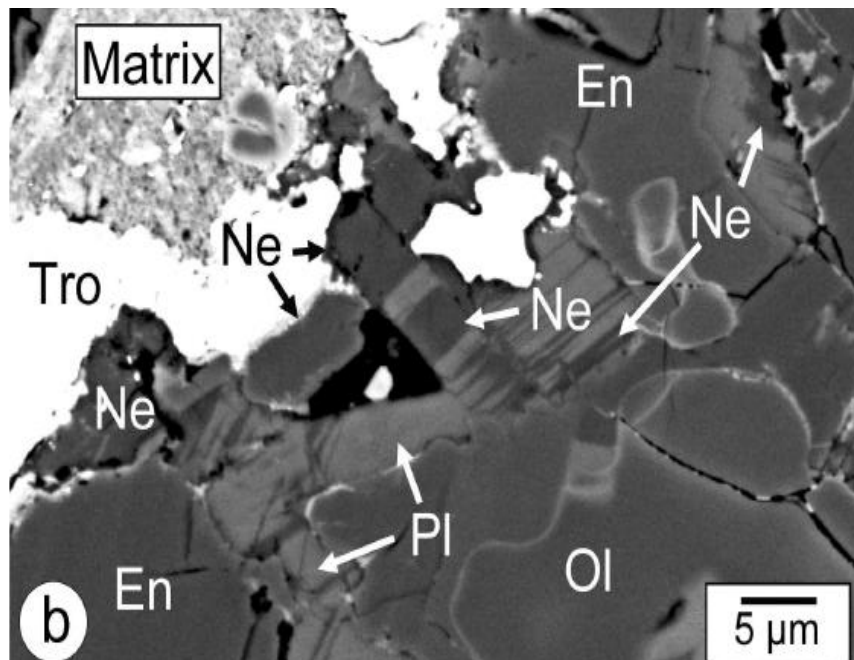
Figure 3: BSE image showing nephelinitization in a type I chondrule in Kainsaz (CO3.2). Thin, dark lamellae of nepheline (Ne) are replacing the lighter plagioclase (Pl). Olivine = Ol, Enstatite = En, Troilite = Tro. After Tomeoka & Itoh, 2004.

Chondrule classification and properties

  Chondrules generally contain olivine, pyroxene, metal, sulfide, and mesostasis, a glassy interstitial phase (Hewins et al., 2005). In the least equilibrated chondrites, chondrule types are defined based on the Fe/(Fe+Mg) ratio of olivine and pyroxene, by their volatile-element composition, and by their textures. Type I chondrules are FeO- and volatile-poor (mg# for olivine and low-Ca pyroxene is generally > 90), often contain high contents of Fe,Ni metal, and some contain FeS. Type II chondrules are FeO-rich, volatile-rich and contain small amounts of metal phases (mg# < 90) (Scott & Krot, 2003, Brearley & Jones, 1998). Furthermore, silica-poor chondrules, rich in olivine, are referred to as type A, and silica-rich chondrules with abundant pyroxene are referred to as type B. Therefore for example, a type IAB chondrule is an FeO- and volatile-poor chondrule containing olivine and pyroxene. Chondrules containing high bulk Al content are called Al-rich chondrules or plagioclase-rich chondrules (PRCs) (Hewins, 1997; Tronche et al., 2007).

  Chondrules also exhibit a wide range of textures, by which they can also be classified: P represents porphyritic, B represents barred, and R represents radial textures. These terms are paired with P and O for pyroxene and olivine, respectively, for example, PO for porphyritic olivine texture (Hewins, 1997). This study focused on type I porphyritic chondrules in unequilibrated chondrites. Type I porphyritic chondrules exhibit a wide range of textures that can vary from chondrule to chondrule as well as from chondrite to chondrite. Figure 4 illustrates a range of type I chondrule textures including

9
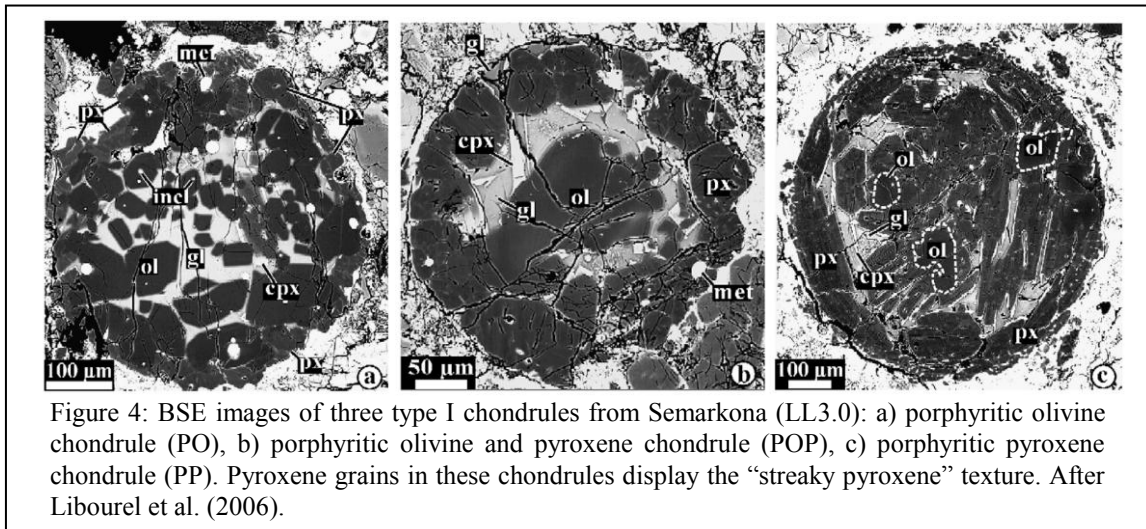
Figure 4: BSE images of three type I chondrules from Semarkona (LL3.0): a) porphyritic olivine chondrule (PO), b) porphyritic olivine and pyroxene chondrule (POP), c) porphyritic pyroxene chondrule (PP). Pyroxene grains in these chondrules display the "streaky pyroxene" texture. After Libourel et al. (2006).

PO, POP, and PP observed in Semarkona, an ordinary chondrite (LL3.0) (Libourel et al., 2006).

As illustrated in the examples above, olivine phenocrysts are often observed throughout the chondrules while pyroxene is often concentrated at the edges of chondrules, and mesostasis is concentrated at the center (e.g. Libourel et al., 2006). In chondrules with substantial amounts of pyroxene, olivine is commonly poikilitically enclosed in pyroxene. Ca-pyroxene occurs as overgrowths on large low-Ca pyroxene grains.

Specifically relevant to the experimental study described in this thesis, some type I chondrules contain low-Ca pyroxene that exhibits a lamellar, streaky texture in backscattered electron (BSE) images (Jones, 1994). This texture is present in chondrules in Figure 4, and is also illustrated in Figure 5. In Semarkona chondrules investigated by Jones (1994), lamellae are similar in width and parallel to twinning observed optically, but it was not possible to determine if twin planes and streaky lamellae are coincident.

Minor chemical zoning of MnO and FeO were observed, however it was not determined if zoning corresponded with the lamellae observed in BSE images (Jones, 1994).

Figure 5: Lamellar texture of low-Ca pyroxene in a type I chondrule from Semarkona. After Jones, 1994.

Origin of chondrule diversity

The cause for the diversity of chondrule types and textures is an important question that could help constrain conditions of the solar nebula during chondrule formation. Potential causes for differences in chondrule compositions include initial compositional heterogeneities in the solar nebula (Jones, 1990), reduction reactions in the solar nebula (Jones, 1990), and open-system behavior during the chondrule-forming event (Cohen et al., 2004).

Different regions in the solar nebula with distinct dust compositions could produce two chondrule groups with distinct compositions (i.e., type I and type II chondrules). These regions could be the result of condensation of chondrule precursors in regions of differing oxygen fugacity (Jones, 1990). The mechanism to create distinct regions of differing oxygen fugacity during condensation of precursor dust is unclear, as

11

is the mechanism to disperse the compositionally different chondrules throughout the nebula after chondrule formation, but before chondrite accretion.

Another potential way to create the distinct compositional groups is by reduction reactions. For example, reduction of type II material has been proposed to form type I chondrules. While a simple one-step reduction process would not account for differences in bulk Fe content between type IA and type II chondrules, Jones (1990) illustrated with a simple calculation that through reduction, loss of Fe and volatilization of SiO_2 and Na_2O, a type I bulk chondrule composition could be derived from a type II chondrule starting composition.

Open-system behavior during chondrule formation has also been suggested by Cohen et al. (2004) to account for the compositional differences between type I and type II chondrules. In an open system, exchange and equilibration with the surrounding vapor or dust via evaporation and/or condensation could change a chondrule's bulk composition. Cohen et al. (2004) showed that by experimentally melting a CI-like composition in a canonical nebular environment, charges of both type IA and type IIA composition are produced through progressive evaporation of FeO and SiO_2, with increasing melting times. However, type IB and type IIB chondrules could not be produced in this manner, and these chondrule types were attributed to a starting material enriched in SiO_2 (Cohen et al., 2004).

In addition to potentially resulting in two types of chondrules, open-system behavior could also result in other compositional trends observed in type I chondrules. For example, Libourel et al. (2006) use open system behavior involving equilibration of a

gas rich in SiO_2 with the melt to explain pyroxene crystallization at chondrule peripheries, as well as mesostasis compositions that are inconsistent with the crystallization histories of type I chondrules. It is likely that most chondrules did not experience formation in a closed system, and various amounts of exchange and equilibration with the surrounding nebula took place, resulting in compositional heterogeneities among the resulting chondrules.

Previous experiments to reproduce chondrule textures

Numerous experimental studies have been carried out to constrain the thermal histories of chondrules. These experiments have reproduced the textures observed in chondrules including porphyritic and barred textures. An important conclusion of many chondrule analog experiments is that the textures observed depend on heterogeneous nucleation, which occurs when pre-existing nuclei are present at the start of cooling. These nuclei come from precursor material that has not been completely dissolved in the melt. The number of nuclei remaining in the melt depends on the heating time, and the peak temperature (Lofgren, 1989; Hewins et al., 2005).

This is illustrated in Figure 6, which shows the results of dynamic crystallization experiments on a type I chondrule composition performed by Lofgren (1989) at various melting temperatures. Longer heating times and higher peak temperatures both reduce the number of nuclei present during cooling, and thus both affect the final observed textures. For example, the experiment heated to a melting temperature of 1550°C and cooled at 5°C/hr contains many nearly euhedral olivine grains, whereas the experiment heated to 1600°C and cooled at 100°C/hr contains fewer elongate bars of olivine. It is difficult to

distinguish between the effects of differences in heating times and peak temperatures by examining textures in natural samples, as both factors contribute to the number of nuclei in the melt at the onset of crystallization.

Homogeneous nucleation occurs if precursor grains are completely melted and no nuclei are present at the onset of cooling. Homogeneous nucleation results from stable nuclei forming due to random structural fluctuations in the melt. The probability for stable nuclei to form via homogeneous nucleation increases with decreasing temperature below the liquidus, until temperatures are low enough that diffusion of elements to the nuclei is limited. Changing the cooling rate of a chondrule can affect how far the

Figure 6: Photomicrographs of experiments performed at a variety of temperatures and cooling rates. At higher melting temperatures and higher cooling rates, textures are more dendritic than porphyritic. Charges are about 4mm in diameter. After Lofgren (1989).
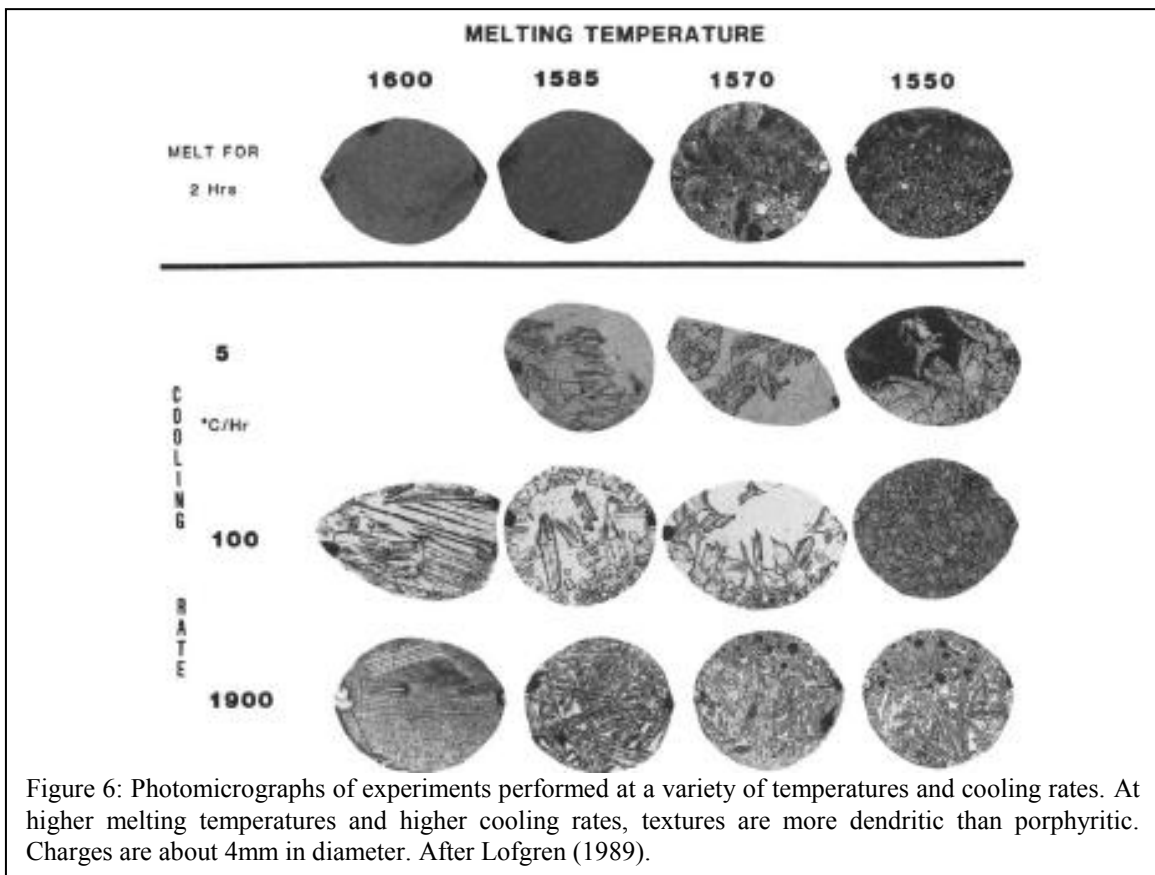
temperature falls below the liquidus of the melted droplet before nucleation commences, which is the amount of supercooling the chondrule experiences.

In the cases of both heterogeneous and homogeneous nucleation, the amount of supercooling also determines the crystal growth rates, which affect the resulting texture. At increased supercooling due to faster cooling rates the drive for crystal growth is large, resulting in fast crystal growth rates, and more dendritic textures (Lofgren, 1989). At small amounts of supercooling due to slower cooling rates, the drive for crystal growth is smaller, resulting in slow crystal growth that resembles equilibrium crystal growth. This is also illustrated in Figure 6, which shows that at faster cooling rates (increasing towards the bottom of the figure) the resultant textures are more dendritic. For example, at a peak temperature of 1585°C, at a cooling rate of 5°C/hr the crystals are euhedral, whereas at a cooling rate of 1000°C/hr, the crystals are elongate to spherulitic. According to these results, porphyritic textures should be expected at slow cooling rates, which promote equilibrium growth, and with lower peak temperatures or shorter heating times, which preserve pre-existing nuclei.

These previous experiments have been used to constrain the conditions experienced by chondrules during their formation. Peak temperatures of chondrule-forming events estimated from textures produced experimentally and compared to natural samples are in the range of 1500 - 1900°C (e.g. Hewins et al., 2005). Experiments have been conducted simulating chondrule formation at cooling rates of 5 to 3000°C/hour (Hewins et al., 2005). However, the range of cooling rates that most chondrules

experienced is considered to be more limited, probably closer to 10 to 1000°C/hour (Hewins et al., 2005).

Plagioclase in type I chondrules

Importance of understanding plagioclase crystallization in type I chondrules

The focus of this thesis is primary igneous plagioclase in type I chondrules. Primary plagioclase is a common phase in type I ferromagnesian chondrules in CO chondrites. Roughly 10% of chondrules in the CO chondrite Kainsaz contain plagioclase (Jones, 1997). However, fewer plagioclase-bearing type I chondrules are observed in other groups such as the CV chondrites and ordinary chondrites (OCs) (Jones, 1997). Understanding plagioclase crystallization in chondrules could play an important role in constraining conditions prevailing in the early solar nebula, and it could also contribute to the relative importance of open-system formation versus closed-system formation for chondrules. It could also help constrain what the precursor materials for chondrules were, and play an important role in chronological studies of the early solar system.

There is a current discussion in the chondrule literature debating whether chondrules formed as closed or open systems. In a closed system, all components of the initial bulk composition are retained in the chondrule during the melting event. In an open system, exchange and equilibration with the surrounding vapor via evaporation and/or condensation could change a chondrule's bulk composition. The behavior of sodium, a moderately volatile element, is important to this discussion. Sodium zoning profiles in olivine grains in type I chondrules in Semarkona (LL3.0) were studied by both Alexander et al. (2008) and Borisov et al. (2008). If evaporation of sodium occurred at high

16

temperatures, the expected signature would be an absence of Na in the cores of olivine grains, with an increase in Na content towards the rims of olivine grains as Na condenses back into the melt as the ambient temperature falls. However, Na is found at the cores of olivine grains and has core-to-rim zoning profiles similar to Cr, Mn, and Ca, indicating that Na is primary and that very little Na evaporated during the time when the chondrule was molten. Since primary plagioclase in CO3 chondrules typically has compositions around An_{80} (Jones 1995), Na was clearly present during crystallization. Studies concerning Na retention in chondrules have indicated that at high oxygen fugacity and with fast heating and cooling times, Na is retained more easily in chondrule melts (Yu et al., 2005; Borisov et al., 2008; Lewis et al., 1993). However, in the case of type I chondrules containing plagioclase, oxygen fugacity is typically very low; these chondrules are highly reduced, with oxygen fugacities (fO_2) just below the iron-wüstite buffer. Also cooling times for these chondrules could be long because of the presence of large (10-100μm) grains of plagioclase, which would not be expected to crystallize until the temperature fell to about 1150 to 1250 ˚C, according to modeling of a type I chondrule starting composition using MELTS software (Ghiorso & Sack, 1995 and Asimow & Ghiorso, 1998). Formation of chondrules in a region with a very high solid density has been invoked to preserve Na in chondrules (Lewis et al., 1993; Alexander et al., 2008; Borisov et al., 2008). If this is true, then we can investigate the implications for a very high solid-density nebula. High solid-densities could provide a link between chondrule formation and planetesimal accretion, since such regions in the nebula could be self-gravitating (Alexander et al., 2008; Hewins et al., 2005). Self-

17

gravitating regions of the nebula would maintain distinct reservoirs for specific chondrule populations in the turbulent solar nebula, helping explain the wide variety of chondrule oxygen isotopic compositions (Hewins et al., 2005), and differences between chondrule populations in different chondrite groups. In short, understanding the presence of plagioclase, and moderately volatile elements like Na in chondrules is fundamental to understanding broader questions relating to the conditions of chondrule formation.

The presence of plagioclase in type I chondrules might provide clues to the nature and composition of chondrule precursor materials. For example, if plagioclase-bearing chondrules have a high Ca and/or Al content in their bulk compositions, this could suggest the starting material for plagioclase-bearing chondrules contained a significant CAI component. Investigation of the compositions of plagioclase-bearing type I chondrules in CO chondrites could provide insight into the composition and nature of the chondrule precursor grains, which can help constrain what materials were present in the chondrule-forming region in the solar nebula.

The presence of primary plagioclase in chondrules is also of significance for chronologic studies of the early solar system. Plagioclase contains significant amounts of Al but very minimal amounts of Mg and thus is an important phase used for dating in the short-lived radioisotope ^{26}Al/^{26}Mg system (e.g. Huss et al., 2001). For chronological studies, it is important to understand whether the plagioclase is primary or secondary, as well as the timing of its crystallization. By studying and understanding plagioclase crystallization, good candidates for ^{26}Al studies can be identified.

Previous experimental studies of plagioclase crystallization:

Understanding how plagioclase-bearing chondrules formed could lead to further insights about crystallization of the entire suite of chondrules and the conditions at the time and place in the solar nebula where they formed. While the importance of understanding the role of plagioclase in chondrules is clear, chondrule plagioclase has not previously been studied. Formation parameters such as peak temperatures, cooling rates, and bulk compositions for plagioclase-bearing chondrules in CO chondrites have yet to be defined.

Most experimental and textural studies of chondrules have focused on olivine and pyroxene, including almost all of the experimental studies of chondrules referenced above. Experiments investigating olivine and pyroxene crystallization are often quenched at temperatures higher than those at which plagioclase would be expected to appear, and also have compositions that may not nucleate plagioclase. In any case, plagioclase has not been observed or studied thus far in chondrule-based experimental studies.

However, even if conditions such as composition and quench temperature are addressed in experiments, plagioclase may be difficult to nucleate in chondrule analogues. In chondrule analog dynamic cooling experiments on a PO composition performed by Lofgren (1989), plagioclase was the final phase expected to nucleate, based on the relevant phase diagram. However, plagioclase was absent in all experiments, even those annealed at temperatures as low as 800°C for periods up to a week. Experimental studies on plagioclase crystallization in a basaltic composition showed very unpredictable nucleation of plagioclase crystals over a range of times and temperatures (Gibb, 1974:

Figure 7: Plagioclase nucleation experiments, after Gibb (1974). Solid symbols represent run products containing glass + plagioclase, and open symbols represent run products containing glass only. On the left are the results of heating experiments in which a basaltic composition with plagioclase on the liquidus was raised to within 30°C degrees of the run temperature, allowed to equilibrate with the furnace atmosphere for 10-20 hours, and then raised to the heating temperature shown for the time shown. On the right are the results of cooling experiments, in which the composition was raised to 1200°C to equilibrate with the furnace atmosphere and then cooled to the temperature shown as fast as possible, then left to equilibrate for the time shown. Experiments were run at 1 atmosphere in the absence of water.

Figure 7). According to Lofgren (1983), plagioclase nucleates only upon itself or

similarly complex tectosilicates, while olivine will nucleate on multiple substrates.

Plagioclase has been produced and studied experimentally in other contexts.

Plagioclase textures have been studied experimentally by Lofgren (1974) using a

plagioclase-composition gel starting material combined with 10 wt. % H_2O at 5 kbar

pressure. Textures ranged from tabular to acicular to skeletal to spherulitic with

increasing degrees of supercooling, and compared well to those observed in natural

basalts formed in a range of conditions. The most important differences between these

experiments and chondrules are that chondrules are considered to crystallize at low

pressures and in the absence of water. Plagioclase has also been produced in 1-

atmosphere dynamic cooling experiments on quartz-normative Apollo 15 basalt compositions (e.g. Grove and Bence, 1977, Grove and Walker, 1977). In these experiments, olivine and low-Ca pyroxene crystallize at high temperature, and plagioclase and Ca-pyroxene crystallize later as a groundmass-aggregate. Grove and Bence (1977) found that the plagioclase appearance temperature (and hence, plagioclase nucleation) is increasingly suppressed at faster cooling rates: At cooling rates of 150°C/hr, plagioclase appears 160°C below its predicted equilibrium appearance temperature, while at cooling rates of 0.5°C/hr, the appearance temperature is suppressed only by 60°C (Grove and Bence, 1977). The most significant difference between these experiments and chondrules is that the Apollo 15 basalt compositions are very rich in Fe and low in Mg compared to bulk compositions of type I chondrules. Further experiments are needed in order to define what conditions are needed for plagioclase to crystallize in chondrule-forming conditions.

Goals of this study:

This study aims to provide further understanding of the conditions under which type I chondrules formed. We describe the occurrence of primary plagioclase in natural type I chondrules in terms of chondrule bulk composition, phase compositions, and textures, and compare plagioclase-bearing and plagioclase-free chondrules. Our studies of natural chondrules focus on the CO3.2 chondrite, Kainsaz. Even though Kainsaz is thermally metamorphosed, there are very few pristine CO chondrites available, and the petrology of Kainsaz chondrules has been studied extensively by Berlin (2009), therefore the relatively minor secondary alteration and metamorphism can be distinguished from primary processes relatively well. We also present the results of dynamic cooling

chondrule analog experiments that aim to constrain conditions under which type I

chondrules formed, as well as investigate the parameters that could influence the

crystallization of plagioclase.

CHAPTER 2:

METHODOLOGY

Natural Samples

Thin sections of Kainsaz (section number USNM 2486-5) and ALHA77307 (section number 40) were obtained from The Smithsonian Institution and the Johnson Space Center Antarctic meteorite collection, respectively. Thin sections were analyzed on the scanning electron microscope and the electron microprobe, both in the Department of Earth and Planetary Sciences at the University of New Mexico. Imaging was done on the JEOL 5800LV Scanning Electron Microscope (SEM) at an accelerating voltage of 20 kV. Compositional analyses were obtained using wavelength-dispersive spectrometry (WDS) on the JEOL 8200 Electron Probe Microanalyzer (EPMA) at an accelerating voltage of 15 kV and a beam current of 20 nA. All analyses were made using a 1μm beam except those of glass or mesostasis, which were made using a 10μm beam, and some analyses of feldspar, which were made using a 5μm beam. ZAF data corrections were used. In general, peak counting times for major elements were 15 sec, peak counting times for minor elements (Na, K, Ti, Mn, Cr, and Fe in silicates) were 20 sec, and background counting times were twice peak counting times. A Co-Fe peak overlap correction was done for metal analyses. Typical mineral standards appropriate for silicate analyses were used for WDS analyses. Typical detection limits (in wt. %) for elements analyzed are as follows: SiO_2: ~0.03, TiO_2: ~ 0.03, Al_2O_3: ~0.02, Cr_2O_3: 0.02-0.05, FeO: 0.02-0.08, MnO: ~0.02, MgO: ~0.02, CaO: 0.01-0.04, Na_2O: 0.01-0.04, K_2O: 0.01-0.02.

X-ray maps of plagioclase-bearing type I chondrules were collected in order to perform modal recombination analysis (MRA) to determine bulk chondrule compositions. Maps were collected at an accelerating voltage of 15 kV and a beam current of 20 nA. Silicon and Mg were collected using energy dispersive spectrometry (EDS) or WDS while Al, Ca, Fe, S, and Na were all collected using only WDS. Dwell times were 25 to 60 μsec per pixel, and resolution was 0.5 to 2 μm per pixel.

Modal recombination analysis was performed using monochromatic x-ray maps. Adobe Photoshop was used to apply black masks to the x-ray maps surrounding the chondrules. These images were then imported into the Lispix program, an image analysis program provided by the National Institute of Standards and Technology. The phase tool was used to assign a range of brightness of the pixels on a given x-ray map to a specific phase. These phases were then combined to form a final image showing each phase in the chondrule, and the modal proportions of each phase were determined based on the relative number of pixels assigned to each phase.

The weighted proportions (X) of each phase (i) were then determined. First, the density of each phase (ρ_i) was determined by calculating the percent end-member for solid solution phases, and using the density given by Deer et al. (1992) for that composition. The density proportion of the bulk silicate was then calculated by summing the density of each phase multiplied by its modal proportion ($[\Sigma\rho_i x_i]$). The weighted proportions (X) were then calculated by multiplying the density of the phase (ρ), by the proportion of pixels (x) in the total and dividing this by the density proportion ($[\Sigma\rho_i x_i]$) of the silicate. For example for olivine:

$$X_{ol} = (\rho_{ol} * x_{ol}) / [\Sigma\rho_i x_i]$$

After the weighted modal proportions of each phase were determined, they were combined with average phase compositions (from electron microprobe analyses at points throughout each phase in the chondrule) to determine the bulk composition. For example, the concentration of oxide (j) in the bulk composition is given by the sum of the weighted proportion (X) of each phase (i) times the concentration (C) of oxide (j) in each phase (i):

$$C_j{}^{bulk} = \Sigma(X_i * C_i)$$

The primary source of error for determining bulk compositions using this method comes from the selection of one cross sectional cut through the chondrite for compositional information (Hezel, 2007). Compositional heterogeneities are expected throughout the chondrule in three dimensions, so we cannot be sure that the cross section is representative of the entire chondrule.

Experiments

A powder was prepared as a starting material for experiments. The composition of this starting material was calculated from an average of the bulk silicate compositions of two natural plagioclase-bearing type I chondrules, a pyroxene-rich plagioclase-bearing chondrule and an olivine-rich plagioclase-bearing chondrule. This composition is shown in Table 1. Details of individual chondrule compositions are given in the Results section.

The equilibrium crystallization sequence was modeled for our bulk composition, as well as the determined bulk compositions of natural type I chondrules using MELTS software (Ghiorso & Sack, 1995 and Asimow & Ghiorso, 1998).

Table 1:	Starting Material (wt. %)	Normative Minerals	Wt % Norm
SiO_2	53.12		
Al_2O_3	3.60	Plagioclase	10.78
Cr_2O_3	0.45	Diopside	7.03
MnO	0.14	Hypersthene	56.98
MgO	37.21	Olivine	23.68
FeO	0.95	Magnetite	0.07
CaO	3.58	Chromite	0.97
Na_2O	0.24		
Total	99.47		

Composition of starting material is based on an average of two chondrules, KMW2 and KMW13 (see Results section). Normative mineralogy is shown at the right.

A dry powder starting material for experiments was prepared from oxides using the procedures described by Edgar (1973). SiO_2 was added as powdered quartz which we heated at 1200°C for one hour to remove moisture. CaO was prepared from $CaCO_3$ by heating it for five hours at 500°C, and then for two hours each at 1000°C and 1250°C to decompose the carbonate. Iron was added as Fe_2O_3 that was heated at 1000°C for two hours to remove moisture. MgO was added as MgO powder heated for one hour at 1200°C to remove moisture. Na_2O was added as Na_2O powder heated at 750°C for one hour to remove moisture. These oxides were weighed out and mixed in their correct proportions. Cr_2O_3 and MnO were added in the form of solutions (1000µg/g) prepared as standards for ICP-OES analyses. A solution containing REEs (10µg/g of Ce, Dy, Er, Eu, Gd, Ho, La, Lu, Nd, Pr, Sm, Sc, Tb, Th, Tm, Yb, and Y) was added to the mixture to obtain a concentration of 100 times the La concentration of CI chondrites, in order to have measurable amounts of REE to investigate REE partitioning in the future. Solutions

were allowed to evaporate and the final oxide mixture was ground under acetone for one hour to homogenize.

Experiments exp24 and exp25 were "seed experiments." The starting material for these experiments contained natural anorthite seed crystals, which were obtained from Professor Carl Agee. Crystalline anorthite (close to endmember anorthite composition) was ground to a grain size of <3μm to ~80μm. A small amount of this powder was added to the starting material used in previous experiments. The anorthite-bearing starting material mixture was then ground lightly to homogenize the starting material.

The oxide mix starting material was pressed into 2 - 3 mm pellets, along with alcohol, which was used as a binder. For most experiments, Re ribbon was wrapped around each pellet in order to suspend the pellet from the sample holder, which consisted of a hook of Pt wire. Figure 8 shows the basic experimental set up and an image of an

Figure 8: At left, a schematic diagram of the experimental set-up, after Lewis et al., (1993). At right, a photograph of a sample pellet suspended from the sample holder. A thermocouple sits inside the
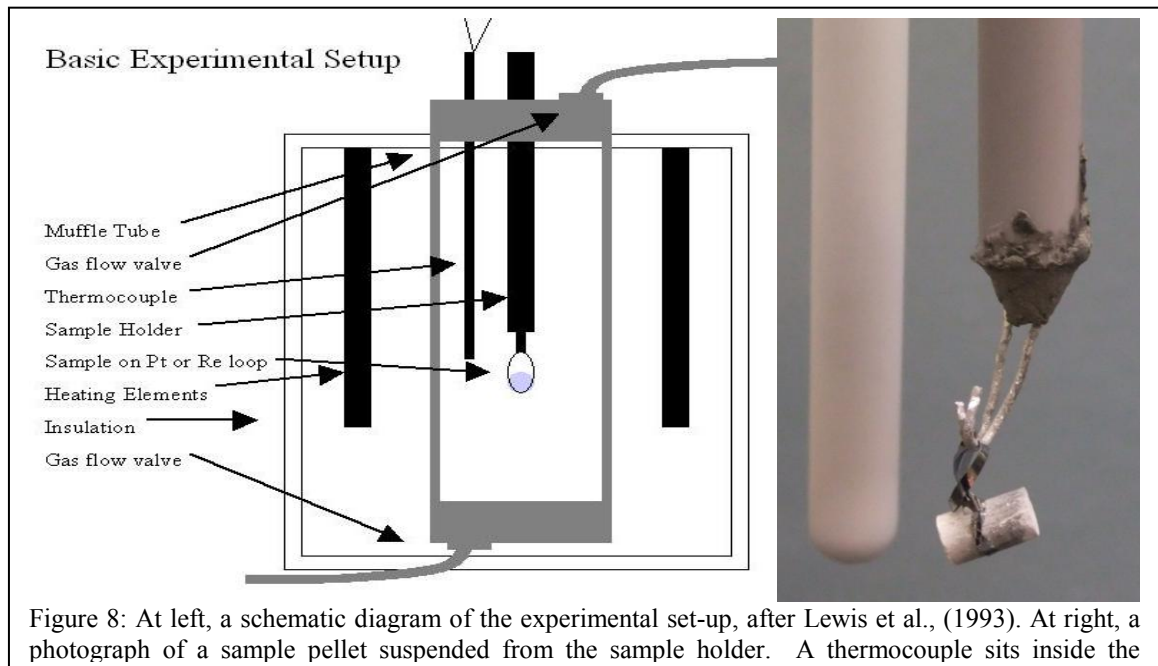
example pellet suspended from the sample holder. Re ribbon was used to prevent Fe-loss from the sample, which is a common problem when Pt wire or foil is used.

Two experiments were conducted in the presence of a Na-rich atmosphere. In these runs, a 1-cm square pocket of Pt foil was constructed by folding Pt foil in half and crimping the edges. Sample material was loaded into the pocket as two pressed pellets. The Pt pocket was hung from the sample holder in the hotspot of the furnace. Below the sample, a ceramic crucible hung from Pt wire. Within the ceramic crucible, another Pt crucible held $Na_2O \cdot SiO_2$ powder. An illustration of this set-up is shown in Figure 9. During the experiment the $Na_2O \cdot SiO_2$ powder melted. The initial composition of the Na-rich melt was 16.9 wt. % Na_2O. During the course of the experiment, Na evaporated from this sodium-rich silicate melt and provided a Na-rich atmosphere around the sample in the Pt pocket. In our first set of experiments with the $Na_2O \cdot SiO_2$ powder, we observed that $Na_2O \cdot SiO_2$ melt has a very low viscosity and tends to creep along any Pt wire or foil it is in contact with. This led to contamination of the sample pellet. The solution to this problem was to construct the set-up shown in Figure 9, in which any creep of the melt was halted by the ceramic crucible that held the Pt crucible with the Na-rich melt. Since the sample in these experiments was in contact with the Pt foil, Fe loss did occur.

Experiments were run in two different Deltech vertical muffle furnaces, one that controlled fO_2 with H_2 and CO_2 gases (furnace one), and one that controlled fO_2 with CO and CO_2 gases (furnace two). Most experiments were conducted in furnace one.

28
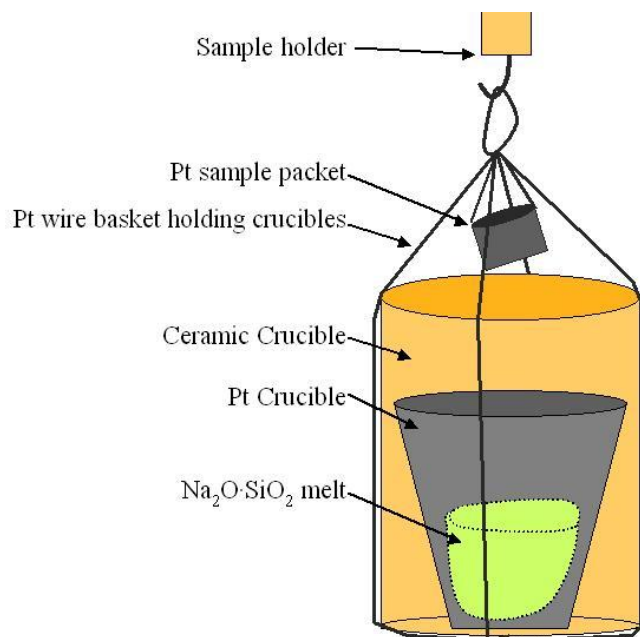
Figure 9: Illustration of sample set-up for Na-rich atmosphere experiments.

Temperatures were controlled by a Eurotherm temperature controller with a type B

thermocouple. Temperatures were calibrated against the melting points of gold and

palladium (1064.2°C, and 1554.9°C, respectively). Oxygen fugacity, controlled by gas

mixing, was held at the iron-wüstite (IW) buffer for all experiments.

For most experiments, in furnace one, we used the following set-up. The sample

holder was inserted into the furnace in most cases at room temperature, however in

several runs the sample was inserted when the furnace was warm, at 300°C to 600°C.

Oxygen fugacity was controlled by a mixture of CO_2 and H_2 gases flowing through the

furnace. Carbon dioxide gas was turned on and flowed through the furnace during

heating. The furnace was initially heated manually to 300°C. The temperature was then

ramped at 900°C/hour using the temperature controller to a peak temperature of 1600°C.

Hydrogen was added to the gas mixture at a temperature of 550°C, and the CO_2/H_2 ratio

was adjusted at 600°C and 650°C, increasing H_2 to a final fO_2 at the IW buffer. The

29

purpose of these adjustments was to prevent graphite precipitation in the muffle tube while also preventing the Re ribbon (holding the sample pellet) from oxidizing at low temperature. Once the sample reached 1600˚C, it was held there for 18 minutes before cooling began according to various programmed cooling rates ranging from 5ºC/hr to 25ºC/hr. At the final temperature (1000˚C, 800˚C, or 650˚C), the H_2 gas was turned off and the sample was removed immediately from the muffle tube and quenched in air. Several high temperature quench experiments were also conducted with the same procedure to heat the sample to 1600ºC as described above. These experiments were then melted for a period of around 10 minutes and immediately removed from the furnace to quench.

Experiments nexp22 and exp23 were conducted in furnace two, during a period of time when furnace one was not operational. Furnace two had a slightly different set-up. In this furnace, a mixture of CO and CO_2 gases controlled oxygen fugacity. The sample was inserted at a temperature of 900˚C. After insertion, both gases were turned on and adjusted to their correct ratios for an oxygen fugacity at the IW buffer. The peak temperature in these experiments was 1500˚C, the maximum temperature at which we could control the temperature at heating and cooling rates we required. The furnace was heated to the peak temperature at a rate of 200ºC/hr. The sample remained at the peak temperature for 18 minutes and was then either quenched by removal from the furnace, or cooled at a rate of 25˚C/hour to a minimum temperature of 900˚C before it was quenched.

Run products were mounted in epoxy plugs and polished. When possible, run products were cut parallel to the vertical direction during the experiment to examine any

effects of gravitational settling. The plugs were then polished with subsequently finer

slurries to a minimum of 0.5μm for microprobe analysis. Scanning electron microscopy

and electron microprobe analysis of experimental runs was conducted in the same fashion

as discussed above for natural samples.

CHAPTER 3:

RESULTS

Natural Sample Results

       We focused our study of natural samples on type I chondrules in the Kainsaz

CO3.2 chondrite. For Kainsaz, we investigated textures of plagioclase-free type I

chondrules, and compositions and textures of plagioclase-bearing type I chondrules. We

measured mineral compositions for nine plagioclase-bearing chondrules, and determined

bulk compositions of six of these. We also studied olivine and pyroxene textures of type I

chondrules in ALHA77307 (CO3.0). ALHA77307 has not experienced the low degree of

thermal metamorphism that Kainsaz has. However, it has experienced aqueous alteration

that has altered the mesostasis phases of type I chondrules, which makes it difficult to

identify or study mesostasis phases like glass and plagioclase in this chondrite.

Plagioclase-free chondrules: Textures from Kainsaz and ALHA77307

       Type I chondrules are the most abundant type of chondrule in CO chondrites.

Olivine and low-Ca pyroxene are the dominant phases, and these occur with varying

abundance in olivine rich (PO, or type IA) to olivine- and pyroxene-rich (POP, or type

IAB) to pyroxene-rich (PP, or type IB) chondrules.

       Examples of type I chondrules from Kainsaz are shown in Figures 10 and 11.

Olivine is often poikilitically enclosed within low-Ca pyroxene grains. Ca-pyroxene

occurs as overgrowths on low-Ca pyroxene. Mesostasis is absent in some chondrules

(Figure 10), while in some it is present (Figure 11). When present, the mesostasis is either

a glassy phase or it consists of what appear to be quench-type crystals. Iron-nickel metal and sulfide grains are present as blebs throughout chondrules.

Examples of type I chondrules from ALHA77307 are shown in Figures 12 and 13. The textures observed in type I chondrules in ALHA77307 are the same as those observed in Kainsaz: olivine poikilitically enclosed in low-Ca pyroxene, and Ca-pyroxene overgrowths on low-Ca pyroxene. However, the mesostasis phases in ALHA77307 are difficult to study due to their extensive alteration.
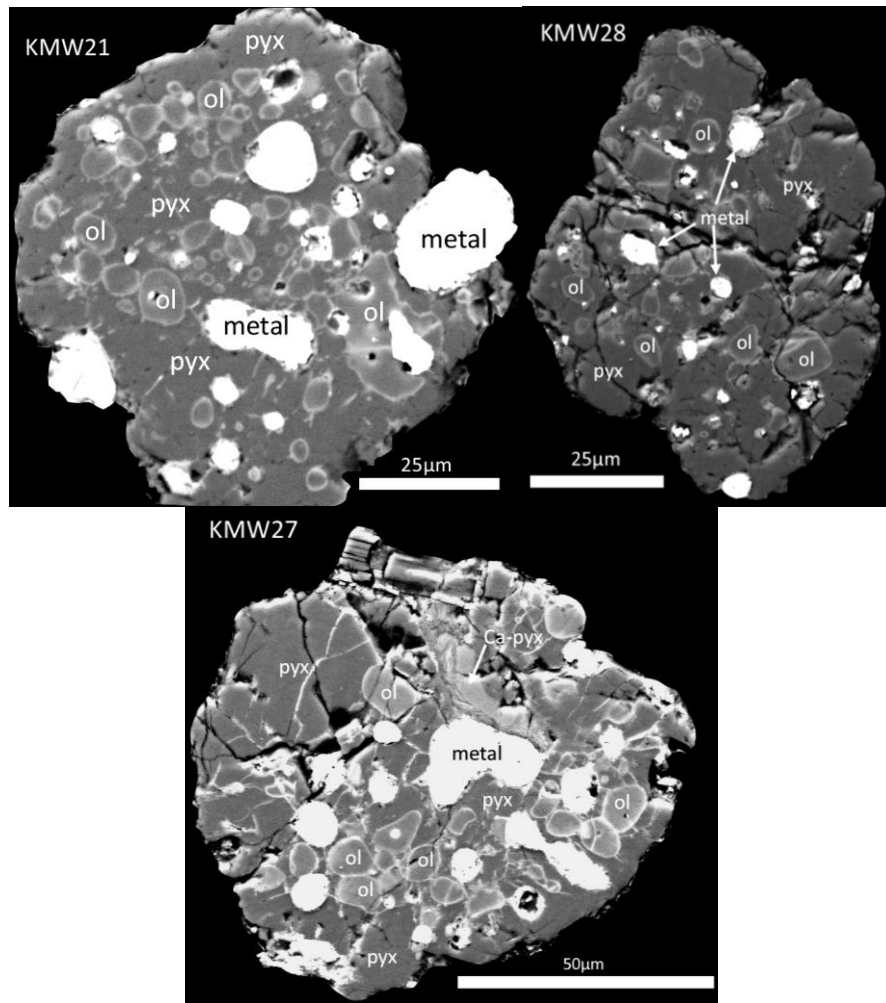
Figure 10: Three examples of type I chondrules from Kainsaz. Each chondrule exhibits olivine poikilitically enclosed within low-Ca pyroxene grains. In these chondrules, there is very little, if any mesostasis.
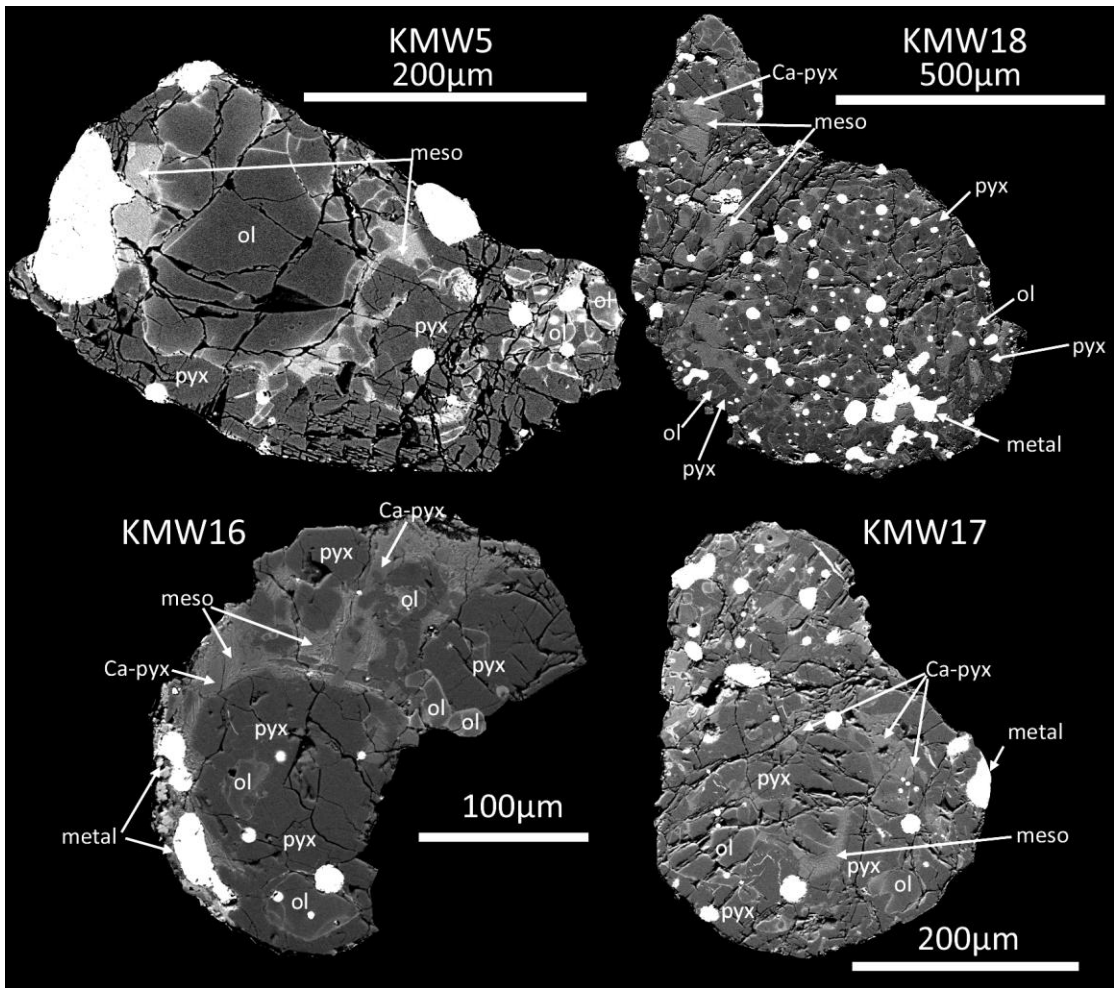
Figure 11: Four examples of type I chondrules from Kainsaz. These examples contain olivine, pyroxene, Ca-pyroxene, metal and sulfide grains, and a glassy mesostasis containing quench crystals.
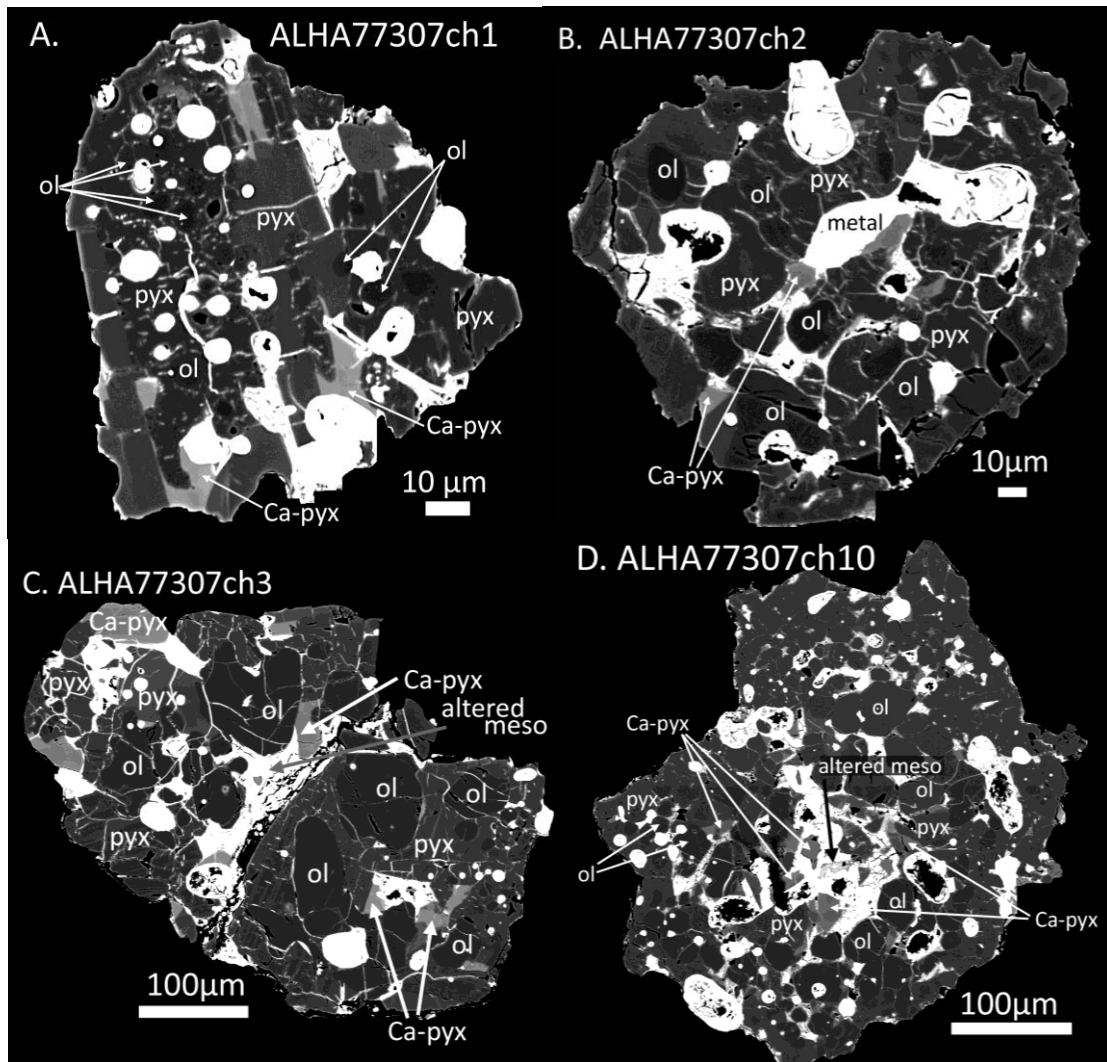
Figure 12: BSE images of four type I chondrules from ALHA77307. The dominant phases are olivine, low-Ca pyroxene, high-Ca pyroxene, and metal/sulfide. The mesostasis in these chondrules and most chondrules in ALHA77307 has been altered substantially due to terrestrial weathering.

Figure 13: BSE images of chondrule 8, a type I chondrule from ALHA77307. This chondrule contains olivine, pyroxene, and abundant Ca-pyroxene, which occurs as overgrowths on low-Ca pyroxene.
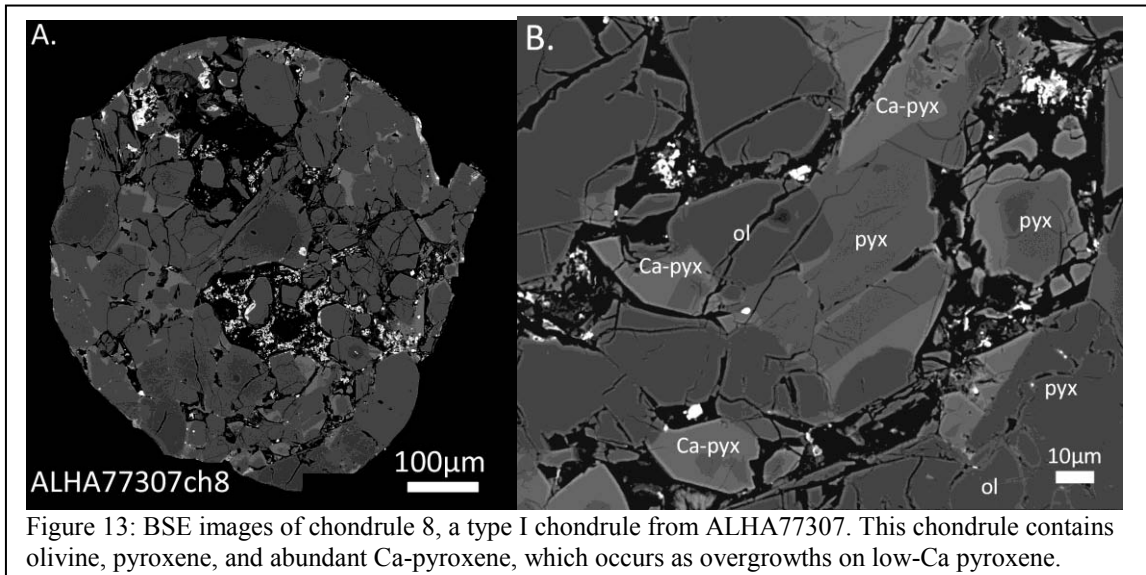
Kainsaz plagioclase-bearing chondrules: Textures

The textures observed in plagioclase-bearing chondrules are very similar to the textures observed in classic type I chondrules such as the plagioclase-free chondrules described above. Olivine, low-Ca pyroxene, and Ca-pyroxene are usually present. Olivine commonly is poikilitically enclosed within low-Ca pyroxene grains. Ca-pyroxene commonly occurs as overgrowths on low-Ca pyroxene. Metal and sulfide grains are dispersed throughout the chondrules. Plagioclase occurs as a mesostasis phase interstitial to olivine and pyroxene, often in the center of the chondrule. Typical textures of plagioclase-bearing chondrules are shown in Figures 14 to 16.

Plagioclase in type I chondrules commonly shows a reaction texture that indicates that it is being replaced by nepheline (nephelinization) (Figures 3, 15, and 16). This texture has been observed previously in CO chondrites, and has been attributed to secondary interaction with a Na-bearing fluid during the early stages of metamorphism

(e.g. Tomeoka and Itoh, 2004). The extent of nephelinization varies among chondrules and within individual chondrites.
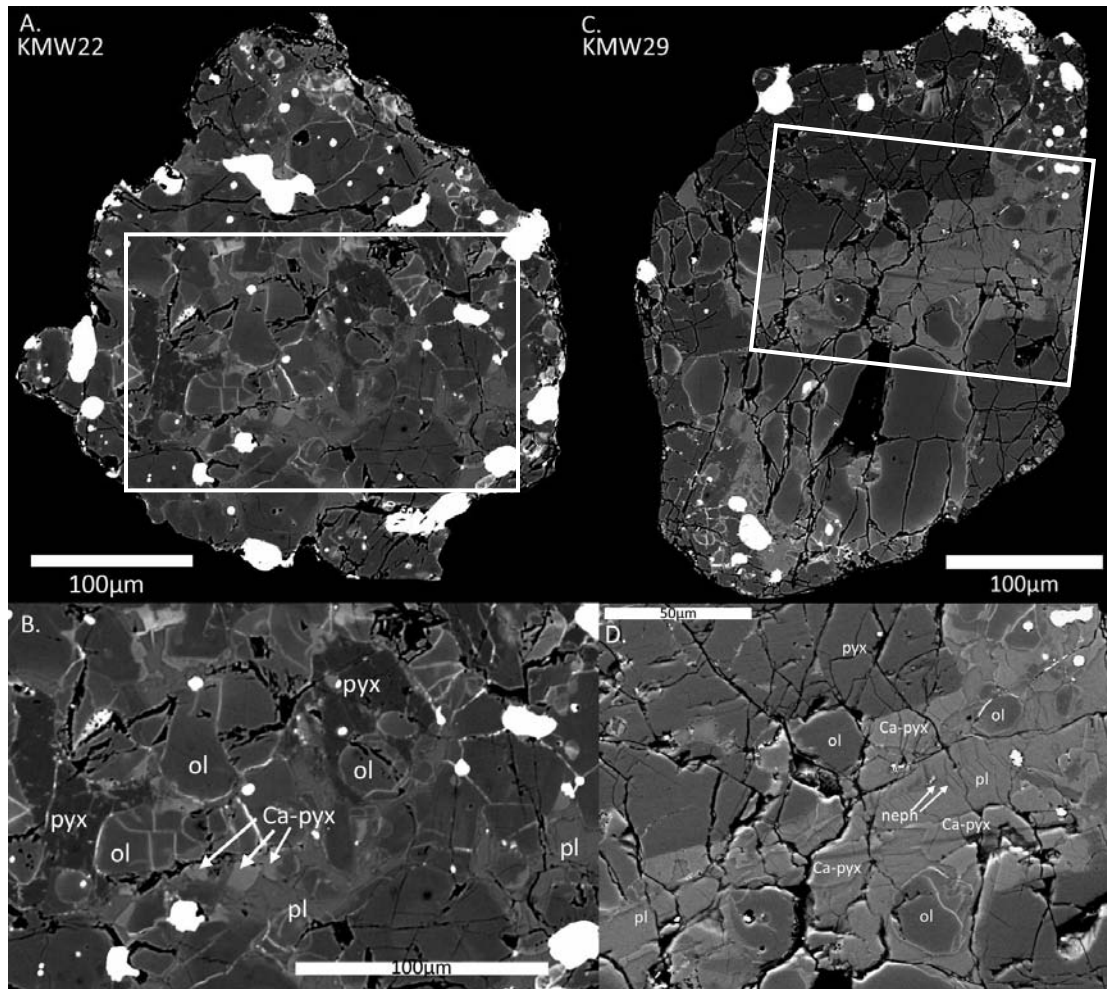
Figure 14: BSE images of two typical plagioclase-bearing chondrules in Kainsaz: (a,b) KMW22. High-magnification image (b) is the area outlined in (a), and shows olivine grains enclosed in low-Ca pyroxene grains, Ca-pyroxene overgrowths, and interstitial plagioclase. (c,d) KMW29. High-magnification image (d) is the area outlined in (c), and shows olivine and low-Ca pyroxene, extensive Ca-pyroxene overgrowths, and interstitial plagioclase. Plagioclase grains contain parallel lamellae of nepheline (darker gray).
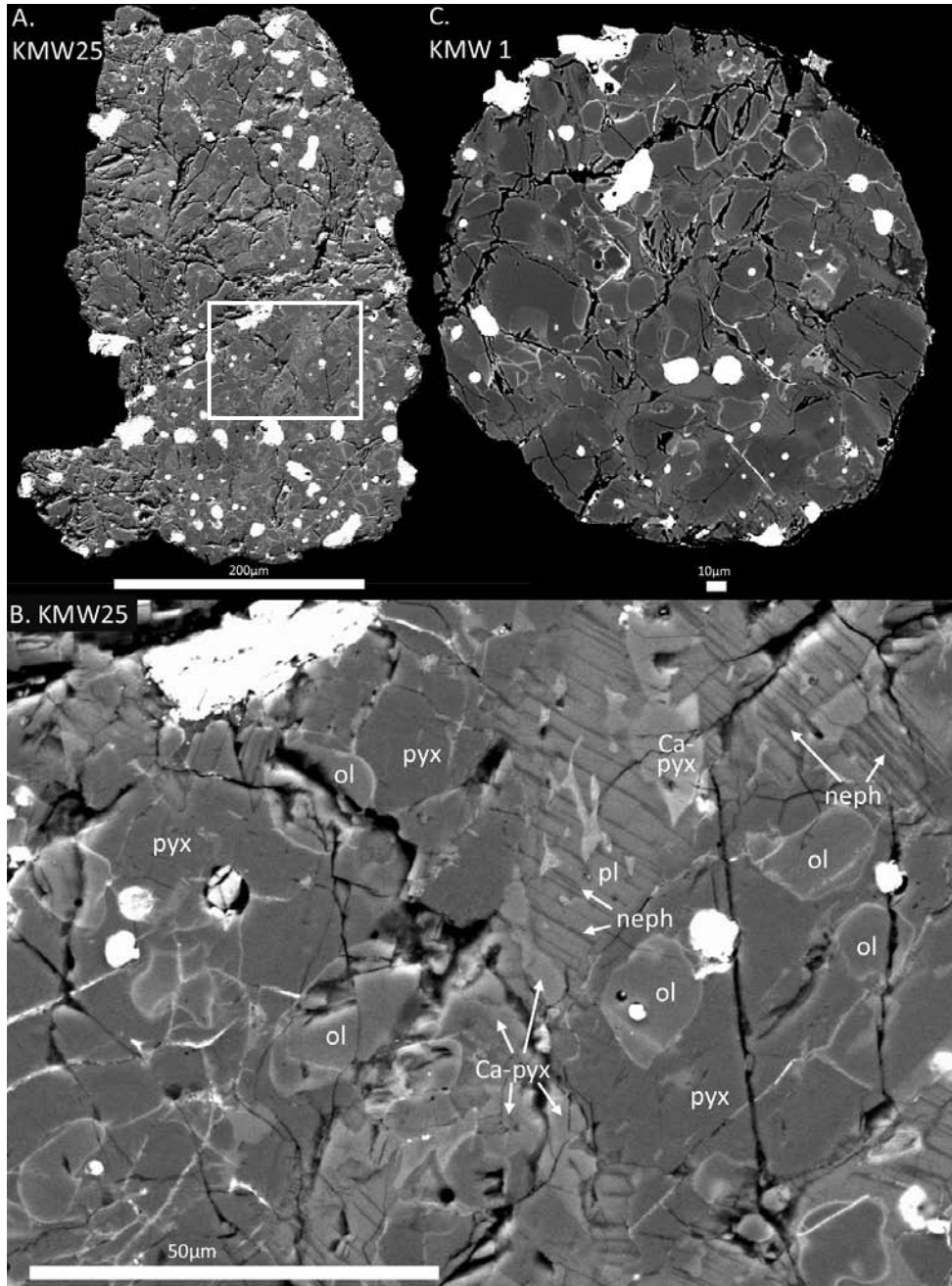
Figure 15: BSE images of Kainsaz plagioclase-bearing chondrules. (a) KMW25, a plagioclase-bearing type I chondrule. (b) High magnification image of KMW25 of area outlined in (a), containing olivine poikilitically enclosed in low-Ca pyroxene, Ca-pyroxene overgrowths, and interstitial plagioclase being replaced by nepheline. (c) KMW1, a plagioclase-bearing chondrule with interstitial plagioclase and low-Ca pyroxene containing poikilitically enclosed olivine grains.
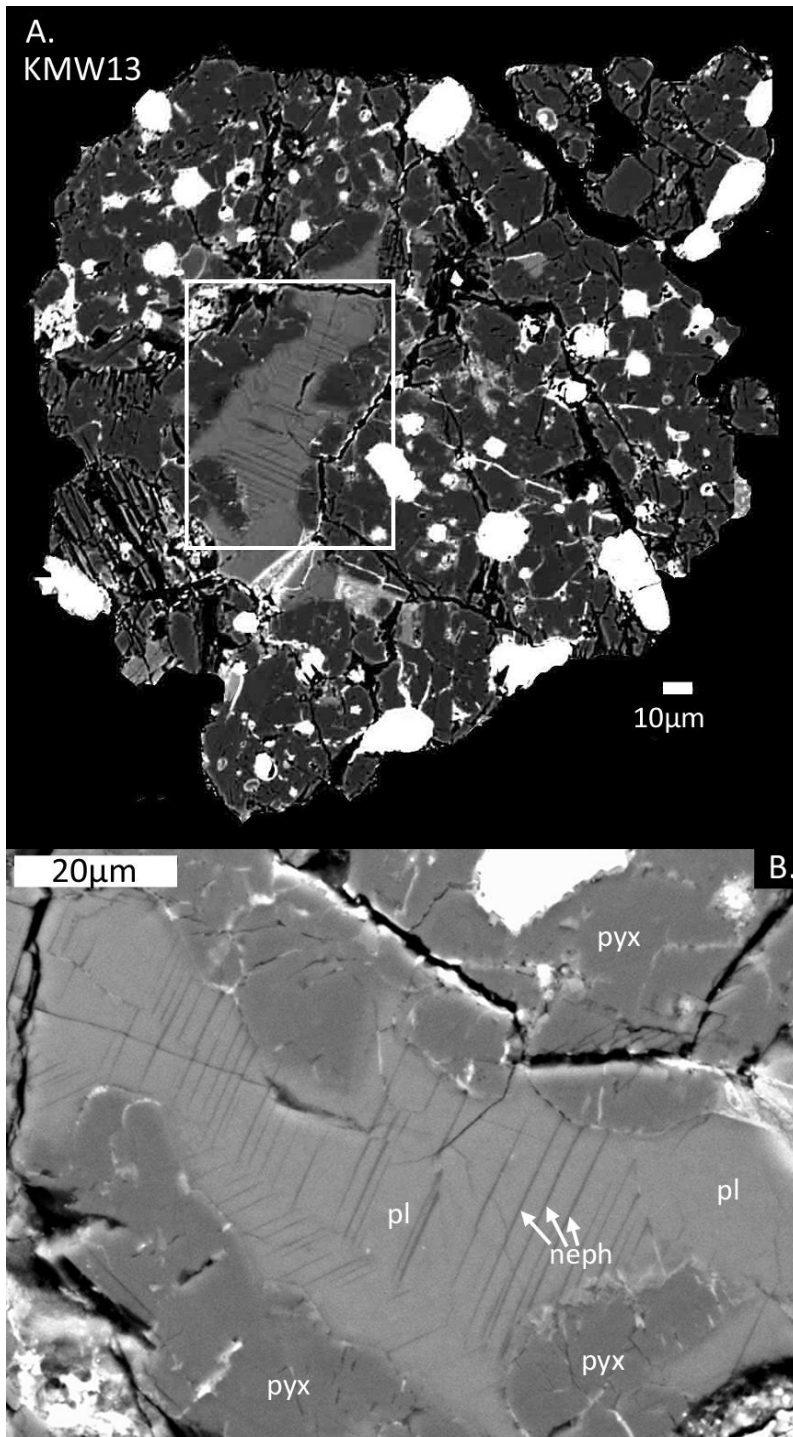
Figure 16: BSE images of Kainsaz plagioclase-bearing chondrule KMW13. (a) Entire chondrule. White phases are Fe,Ni metal and sulfide. Feldspar is concentrated at the center of the chondrule. (b) High-magnification image area outlined in (a), and rotated 90 degrees to the left. Nepheline can be observed as thin dark lamellae replacing the lighter plagioclase grains.

Kainsaz plagioclase-bearing chondrules: Mineral compositions and bulk silicate

chondrule compositions

Compositions of major silicate phases (olivine, low-Ca pyroxene, Ca-pyroxene, and plagioclase) of type I plagioclase-bearing chondrules were determined using electron microprobe microanalysis (Tables 2-5). Compositions are in most cases averages of several point analyses, the number of which is given for each chondrule. In some cases where secondary Fe-enrichment in olivine was extensive, a representative olivine analysis with the lowest Fe content was chosen. A representative analysis is also given in some cases where Ca-pyroxene grains are rare or very small.

In the table of plagioclase compositions (Table 5), we include the cation totals. Plagioclase cation totals are consistently imperfect, with totals that differ by 0.03 to 0.06 from the ideal stoichiometry of 5 cations per 8 oxygens. In many cases, secondary nepheline is observed replacing plagioclase (see Figures 15b and 16b). It occurs as thin plates, and can be quite extensive within plagioclase grains. Although we tried to avoid including nepheline in our analyses, we suspect that inclusion of small amounts of nepheline is the cause for imperfect cation totals.

Figure 17 (a,b) shows plots of minor element compositions for type I plagioclase-bearing chondrule olivine from Kainsaz, compared with literature data for Kainsaz plagioclase-free chondrules (Berlin, 2009) and plagioclase-free chondrules from ALHA77307 (Jones, 1992; Brearley & Jones, 1998; Noguchi, 1989). Because Kainsaz is slightly thermally metamorphosed, the Kainsaz olivine compositions on these plots show

Table 2: Olivine compositions for Kainsaz plagioclase-bearing chondrules					
Wt.% Oxides:	**KMW1**	**KMW2**	**KMW6**	**KMW13**	**KMW20**
SiO2	40.48 (0.09)	41.30 (0.45)	41.74 (0.40)	39.63	39.65
TiO2	BD	0.04 (0.02)	0.07 (0.02)	BD	0.00
Al2O3	0.02 (0.01)	0.13 (0.03)	0.16 (0.04)	0.04	0.03
Cr2O3	0.05 (0.03)	0.14 (0.08)	0.14 (0.13)	0.05	0.06
FeO	9.03 (0.38)	1.15 (0.67)	2.49 (1.34)	8.35	7.99
MnO	0.29 (0.02)	0.09 (0.03)	0.08 (0.02)	0.17	0.19
MgO	50.54 (0.33)	55.98 (0.54)	55.15 (0.94)	50.62	50.90
CaO	0.18 (0.01)	0.38 (0.16)	0.20 (0.04)	0.21	0.17
Total	100.61	99.23	100.05	99.05	99.02
Fo	91.0	99.0	97.5	91.6	91.9
Fa	9.0	1.0	2.5	8.4	8.1
No. of Analyses	6	6	9	R	R
Wt.% Oxides:	**KMW22**	**KMW25**	**KMW29**	**KMW30**	**KMW31**
SiO2	40.48 (0.26)	42.88	43.01 (0.21)	42.62 (0.14)	42.62 (0.33)
TiO2	BD	BD	0.04 (0.03)	BD	BD
Al2O3	BD	BD	0.09 (0.06)	0.01 (0.02)	0.04 (0.02)
Cr2O3	0.08 (0.09)	0.04	0.15 (0.09)	0.06 (0.04)	0.07 (0.04)
FeO	8.91 (0.88)	3.73	2.67 (1.45)	5.33 (1.25)	4.65 (0.75)
MnO	0.21 (0.04)	0.14	0.09 (0.04)	0.14 (0.05)	0.13 (0.02)
MgO	49.54 (0.51)	54.27	54.68 (0.69)	53.10 (1.12)	53.72 (0.82)
CaO	0.15 (0.02)	0.24	0.30 (0.09)	0.16 (0.04)	0.19 (0.04)
Total	99.42	101.33	101.08	101.46	101.43
Fo	90.8	68.5	97.3	94.7	95.4
Fa	9.2	31.5	2.7	5.3	4.6
No. of Analyses	6	R	8	10	10

Compositions are averages of the number of analyses given, or in some cases, one representative analysis was chosen (indicated by an R in the Analyses row). Values in parentheses are one standard deviation for that average. BD indicates concentration was below detection limits.

Table 3: Low-Ca Pyroxene Compositions for Kainsaz plagioclase-bearing chondrules					
Wt.%Oxides:	KMW1	KMW2	KMW6	KMW13	KMW20
SiO2	55.09 (1.53)	57.47 (0.42)	57.57 (0.43)	57.99 (0.27)	58.38 (0.31)
TiO2	0.22 (0.05)	0.18 (0.04)	0.25 (0.08)	0.12 (0.03)	0.1 (0.02)
Al2O3	3.69 (1.53)	1.32 (0.35)	1.41 (0.30)	0.85 (0.08)	0.86 (0.14)
Cr2O3	1.16 (0.22)	0.55 (0.14)	0.56 (0.11)	0.51 (0.04)	0.40 (0.02)
FeO	3.84 (0.11)	0.54 (0.03)	0.76 (0.36)	1.04 (0.31)	1.01 (0.26)
MnO	0.15 (0.04)	0.11 (0.03)	0.09	0.14 (0.01)	0.07 (0.02)
MgO	34.65 (0.88)	38.43 (0.40)	37.81	38.06 (0.46)	37.87 (0.26)
CaO	0.81 (0.09)	0.55 (0.15)	0.80	0.98 (0.49)	0.53 (0.09)
Na2O	BD	BD	0.07	0.03 (0.01)	0.05 (0.01)
Total	100.61	99.15	99.32	99.73	99.27
Fs	5.7	1.0	1.0	1.5	1.5
En	92.7	98.0	97.4	96.5	97.6
Wo	1.6	1.0	1.5	2.0	1.0
No. of Analyses	5	2	3	3	11
Wt.%Oxides:	KMW22	KMW25	KMW29	KMW30	KMW31
SiO2	57.11 (0.63)	58.95 (0.80)	58.94	59.72 (0.30)	59.98 (0.60)
TiO2	0.09 (0.03)	0.17 (0.05)	0.21	0.22 (0.07)	0.16 (0.12)
Al2O3	1.27 (0.51)	1.05 (0.25)	1.09	1.37 (0.34)	1.03 (0.56)
Cr2O3	0.85 (0.14)	0.55 (0.09)	0.42	0.48 (0.08)	0.57 (0.14)
FeO	4.00 (0.30)	1.35 (0.86)	0.35	0.90 (0.43)	0.91 (0.26)
MnO	0.14 (0.06)	0.15 (0.04)	0.03	0.12 (0.10)	0.11 (0.03)
MgO	34.83 (0.96)	38.42 (1.01)	39.27	38.24 (0.37)	37.97 (0.86)
CaO	0.92 (0.47)	1.02 (0.51)	0.56	0.62 (0.10)	0.74 (0.28)
Na2O	0.05 (0.02)	0.03 (0.02)	BD	0.04 (0.02)	BD
Total	99.22	101.73	100.86	101.72	101.51
Fs	5.9	1.9	0.5	1.3	1.3
En	92.3	96.2	98.5	97.6	97.3
Wo	1.8	1.8	1.0	1.1	1.4
No. of Analyses	24	6	R	9	6

Compositions are averages of the number of analyses given, or in some cases, one representative analysis was chosen (indicated by an R in the Analyses row). Values in parentheses are one standard deviation for that average. BD indicates concentration was below detection limits.

Table 4: Ca-pyroxene Compositions for Kainsaz plagioclase-bearing chondrules					
Wt.% Oxides:	**KMW1**	**KMW2**	**KMW6**	**KMW13**	**KMW20**
SiO2	49.17	51.96 (0.85)			
TiO2	3.22	0.96 (0.14)			
Al2O3	3.49	4.34 (0.52)			
Cr2O3	1.49	1.11 (0.13)			
FeO	3.85	0.61 (0.05)			
MnO	0.61	0.47 (0.08)			
MgO	17.12	21.17 (0.57)			
CaO	20.09	18.62 (0.70)			
Na2O	0.07	0.05 (0.03)			
Total	99.11	99.29			
Fs	6.3	1.0			
En	49.7	62.2			
Wo	43.9	36.8			
No. of Analyses	R	5			

Wt.% Oxides:	**KMW22**	**KMW25**	**KMW29**	**KMW30**	**KMW31**
SiO2		55.41	55.28 (0.90)	55.04	54.74
TiO2		0.63	0.80 (0.15)	0.74	0.99
Al2O3		2.68	2.63 (0.77)	5.28	3.62
Cr2O3		0.72	0.67 (0.06)	0.87	0.78
FeO		1.34	0.47 (0.09)	0.62	0.64
MnO		0.19	0.25 (0.03)	0.23	0.17
MgO		26.25	25.02 (3.12)	25.15	20.73
CaO		14.51	16.35 (3.90)	13.75	20.27
Na2O		0.04	0.06 (0.26)	0.05	0.08
Total		101.84	100.86	101.75	102.08
Fs		2.0	0.7	1.0	1.0
En		70.1	67.5	71.1	58.1
Wo		27.9	31.8	27.9	40.9
No. of Analyses		R	7	R	R

Compositions are averages of the number of analyses given, or in some cases, one representative analysis was chosen (indicated by an R in the Analyses row). Values in parentheses are one standard deviation for that average. BD indicates concentration was below detection limits. Blank columns indicate these chondrules contained insufficient Ca-pyroxene to analyze.

Table 5: Plagioclase compositions for Kainsaz plagioclase-bearing chondrules

Wt.% Oxides:	KMW1	KMW2	KMW6	KMW13	KMW20
SiO2	45.95 (0.29)	47.41 (0.51)	47.19 (0.45)	47.38 (1.13)	46.41
Al2O3	33.19 (0.41)	31.85 (0.22)	31.98 (0.29)	32.08 (0.90)	34.05
FeO	0.99 (0.20)	0.80 (0.10)	0.88 (0.25)	0.91 (0.38)	0.39
MgO	0.26 (0.05)	0.66 (0.12)	0.64 (0.10)	0.19 (0.07)	1.45
CaO	17.16 (0.27)	16.47 (0.29)	16.75 (0.39)	16.13 (1.29)	16.45
Na2O	2.02 (0.27)	2.60 (0.20)	2.34 (0.21)	2.69 (0.84)	1.84
K2O	0.05 (0.03)	0.11 (0.03)	0.06 (0.03)	0.06 (0.05)	0.11
Total	99.63	99.90	99.84	99.44	100.69
Cation Totals					
Si	2.13	2.19	2.18	2.20	2.13
Al	1.82	1.74	1.74	1.75	1.84
Fe	0.04	0.03	0.03	0.04	0.03
Mg	0.02	0.05	0.04	0.01	0.06
Ca	0.85	0.82	0.83	0.80	0.81
Na	0.18	0.23	0.21	0.24	0.16
K	0.00	0.01	0.00	0.00	0.01
Total	5.05	5.06	5.05	5.05	5.03
An	82.2	77.3	79.5	76.5	82.7
Ab	17.5	22.1	20.1	23.1	16.7
Or	0.3	0.6	0.4	0.3	0.6
No. of Analyses	5	7	8	5	R

Wt.% Oxides:	KMW22	KMW25	KMW29	KMW30	KMW31
SiO2	46.44 (0.28)	44.97 (0.47)	46.65 (0.76)	48.80 (0.59)	46.44 (0.49)
Al2O3	33.25 (0.30)	35.23 (0.63)	33.20 (0.46)	30.94 (0.39)	33.46 (0.78)
FeO	0.48 (0.24)	0.70 (0.16)	0.91 (0.15)	1.17 (0.28)	1.01 (0.27)
MgO	1.40 (0.07)	0.48 (0.47)	0.66 (0.15)	0.86 (0.27)	0.60 (0.26)
CaO	16.51 (0.32)	16.44 (0.85)	16.28 (0.50)	14.96 (0.18)	16.43 (0.32)
Na2O	2.09 (0.13)	2.74 (0.79)	2.43 (0.26)	3.15 (0.17)	2.23 (0.21)
K2O	0.08 (0.03)	0.09 (0.05)	0.12 (0.03)	0.07 (0.02)	0.10 (0.02)
Total	100.25	100.64	100.24	99.96	100.26
Cation Totals					
Si	2.14	2.07	2.15	2.25	2.14
Al	1.81	1.91	1.80	1.68	1.82
Fe	0.03	0.03	0.03	0.05	0.04
Mg	0.05	0.03	0.05	0.06	0.04
Ca	0.82	0.81	0.80	0.74	0.81
Na	0.19	0.24	0.22	0.28	0.20
K	0.00	0.01	0.01	0.00	0.01
Total	5.05	5.10	5.06	5.06	5.05
An	81.0	76.4	78.2	72.1	79.9
Ab	18.5	22.6	21.1	27.5	19.6
Or	0.5	0.9	0.7	0.4	0.6
No. of Analyses	7	8	7	7	3

Compositions are averages of the number of analyses given, or in some cases, one representative analysis was chosen (indicated by an R in the Analyses row). Values in parentheses are one standard deviation for that average. BD indicates concentration was below detection limits. Cation totals are based on 8 oxygen.

a trend towards higher Fe contents, while olivine compositions in ALHA77307 do not. On both of these plots, MnO and CaO versus FeO, Kainsaz plagioclase-bearing chondrule olivine is indistinguishable from Kainsaz plagioclase-free chondrule olivine.

Low-Ca pyroxene compositions are plotted in Figure 17 (c,d). FeO contents of low-Ca pyroxene in Kainsaz are low and comparable to ALHA77307, consistent with lower diffusion rates in pyroxene compared with olivine, hence a more limited response to mild thermal metamorphism. Cr_2O_3 and MnO contents of low-Ca pyroxene in Kainsaz plagioclase-bearing chondrules fall within the range of typical plagioclase-free type I chondrule compositions.

Ca-pyroxene compositions for plagioclase-bearing chondrules are shown in Figure 18, and compared to literature data for plagioclase-free chondrules from Kainsaz (Berlin, 2009), and type I plagioclase-free chondrules from ordinary chondrite (LL3.0) Semarkona (Jones & Scott, 1989; Huang, 1996; Matsunami, 1993; Ninagawa, 1992; Jones, 1994). Semarkona data was used for comparison because no literature data for Ca-pyroxenes in CO3.0 chondrites are available. From these plots we can see that the compositions of Ca-pyroxene in Kainsaz plagioclase-bearing chondrules is very similar to compositions in plagioclase-free type I chondrules, especially for Cr_2O_3 versus FeO and for MnO versus FeO. Al_2O_3 contents are generally lower than those in plagioclase-free chondrules, consistent with the presence of plagioclase which would be expected to compete with Ca-pyroxene for Al_2O_3.
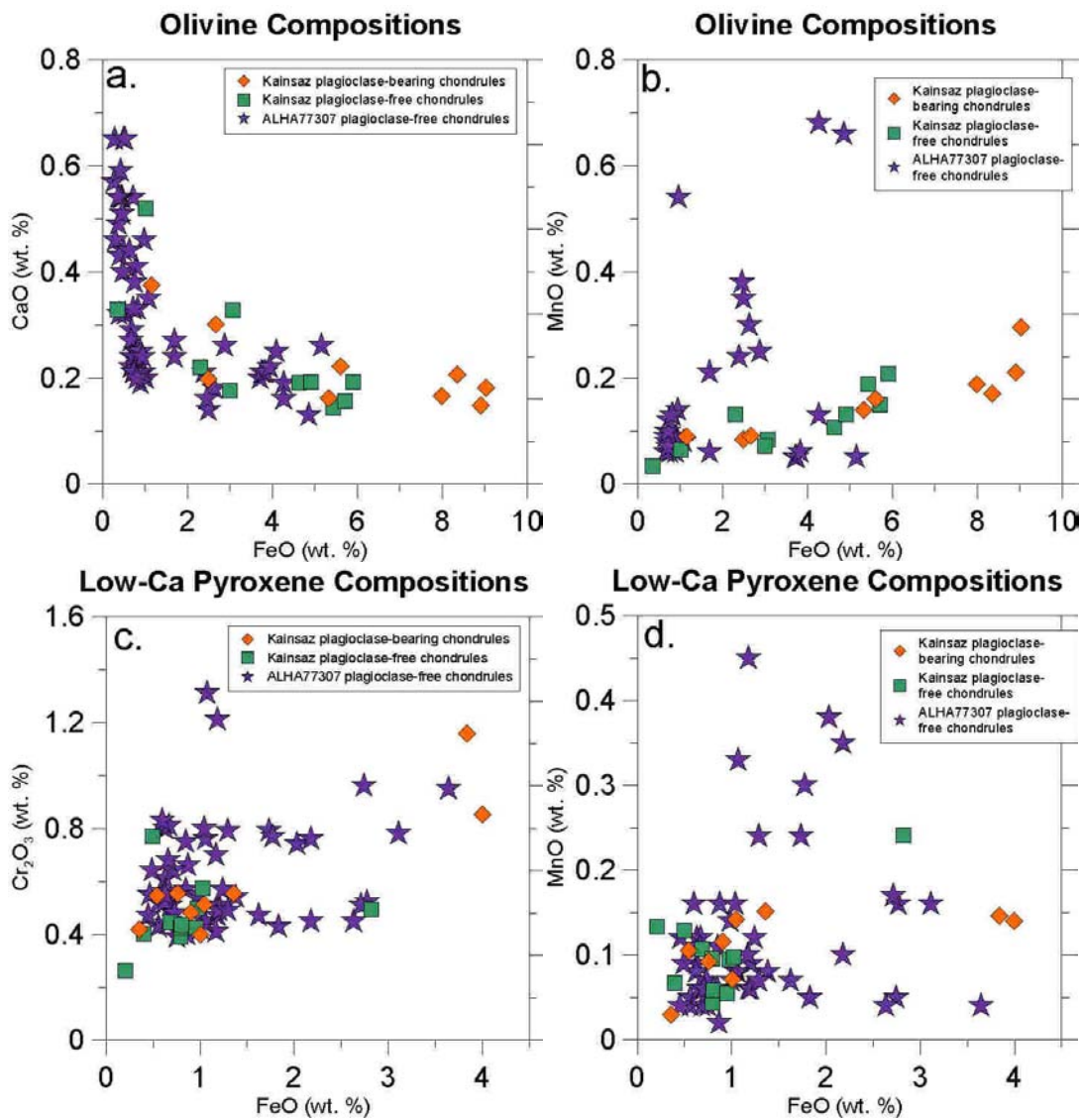
Figure 17: Minor element plots for olivine (a,b) and low-Ca pyroxene (c,d). Average or representative phase compositions (see Tables 2-3) from several Kainsaz (CO3.2) plagioclase-bearing chondrules are shown as orange diamonds, and are compared with Kainsaz plagioclase-free chondrules (Berlin, 2009), and ALHA77307 (CO3.0) chondrules (Jones, 1992; Brearley & Jones, 1998; Noguchi, 1989). Plagioclase-bearing chondrule olivine and low-Ca pyroxene compositions fall within the range of typical type I chondrule compositions.
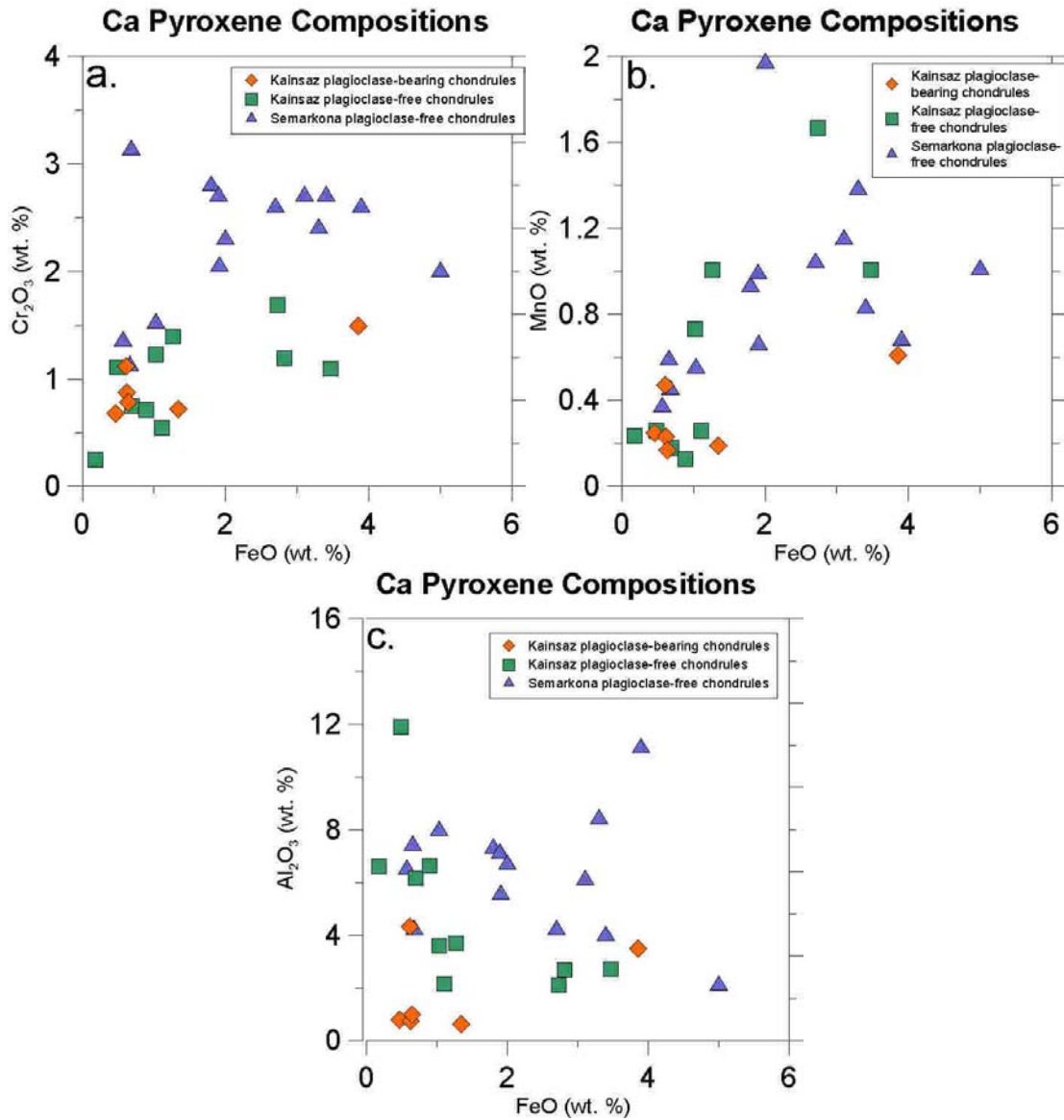
Figure 18: Minor element plots for Ca-pyroxene. Average or representative phase compositions (see Table 4) for several Kainsaz (CO3.2) plagioclase-bearing chondrules are shown as orange diamonds, and are compared with Kainsaz plagioclase-free chondrules (Berlin, 2009), and Semarkona (LL3.0) chondrules (Jones & Scott, 1989; Huang, 1996; Matsunami, 1993; Ninagawa, 1992; Jones, 1994). Plagioclase-bearing chondrule Ca-pyroxene compositions fall within the range of typical type I chondrule compositions.

The bulk silicate compositions of six plagioclase-bearing type I chondrules were determined using modal recombination analysis. Silicate-only bulk compositions were determined because we wanted to determine a bulk composition to use in experiments, where we were interested in reproducing only the silicate portion of the chondrules. Modal proportions of silicate phases were calculated using phase maps (Figure 19). The chondrules selected show the range of dominant mineralogy from olivine-rich to pyroxene-rich. The silicate bulk compositions determined are shown in Table 6, along with the modal proportions of the phases present. Silicate bulk compositions are very Mg-rich. We used MELTS (Ghiorso & Sack, 1995 and Asimow & Ghiorso, 1998) to model liquidus temperatures, which range from 1620°C to 1700°C (Table 6). The crystallization sequence predicted by MELTS is compared to the observed crystallization sequence in the Discussion.

ALHA77307 Plagioclase-bearing Chondrule:

One plagioclase-bearing chondrule (ch5) was identified in ALHA77307 (Figure 20). The texture of this chondrule is similar to the textures of plagioclase-bearing chondrules in Kainsaz. It contains olivine, low-Ca pyroxene, Ca-pyroxene, and plagioclase. Olivine is commonly poikilitically enclosed within low-Ca pyroxene. Plagioclase is interstitial to olivine, and pyroxene and does not contain any nepheline lamellae.
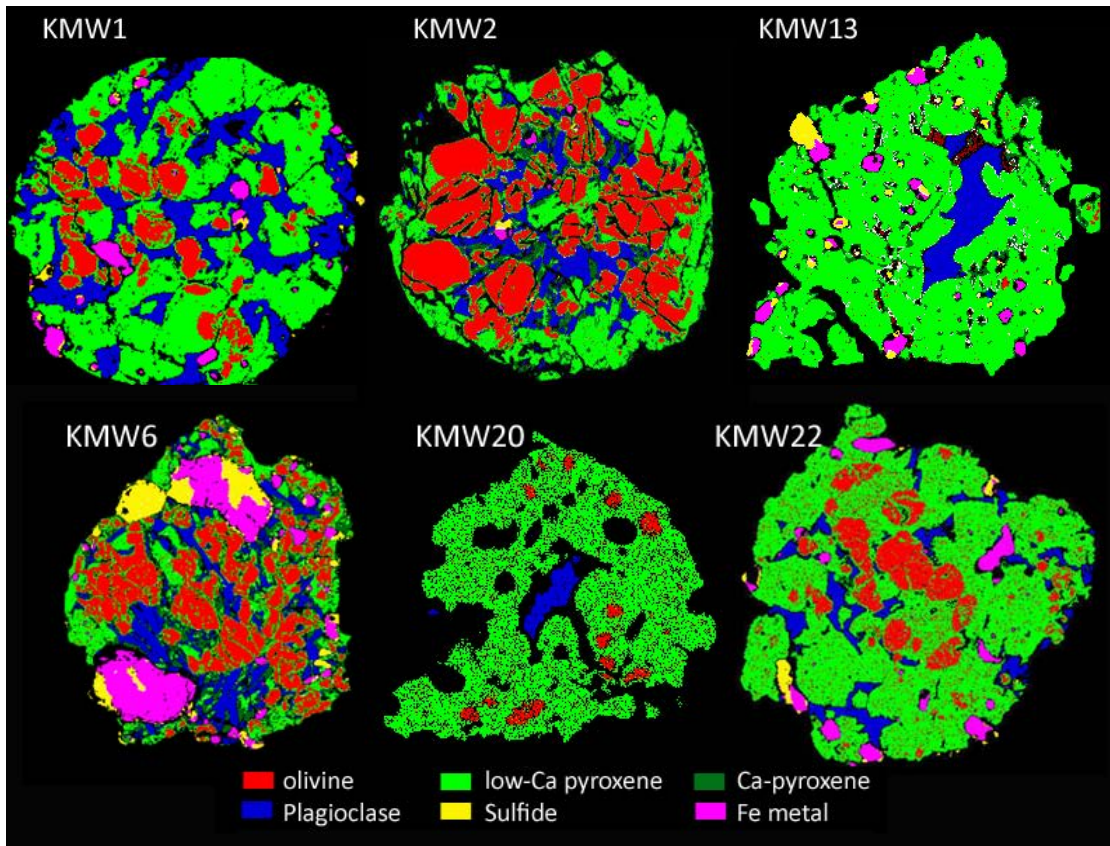
Figure 19: Modal phase maps of six plagioclase-bearing chondrules identified from Kainsaz.

Table 6: Bulk Silicate Compositions of Kainsaz Plagioclase-bearing Chondrules						
Wt% Oxides:	KMW1	KMW2	KMW6	KMW13	KMW20	KMW22
SiO2	51.01	49.13	50.31	57.15	56.64	53.33
TiO2	0.27	0.24	0.15	BD	0.09	0.06
Al2O3	8.88	4.17	5.66	3.04	2.02	4.61
Cr2O3	0.79	0.43	0.32	0.48	0.36	0.64
FeO	4.02	0.82	1.40	1.07	1.51	4.48
MnO	0.16	0.15	0.08	0.13	0.08	0.14
MgO	29.48	38.94	38.30	35.47	37.40	33.32
CaO	4.71	5.12	3.04	2.04	1.09	2.53
Na2O	BD	0.25	0.37	BD	0.12	0.27
Total	99.75	99.26	99.62	99.38	99.30	99.36
Modal Proportion of Silicate Phases						
Olivine	13.3	39.2	35.8	0.6	7.0	15.6
Low-Ca Pyroxene	62.3	32.8	48.8	92.4	89.4	73.3
Ca-Pyroxene	4.3	17.3	0.0	0.0	0.0	0.0
Plagioclase	19.4	10.6	15.4	7.0	3.7	11.1
Liquidus temperatures (℃) (MELTS)						
	1610	1700	1697	1670	1682	1645

BD indicates concentration is below detection limits.

Figure 20: BSE images of plagioclase-bearing chondrule ch5 from ALHA77307 (CO3.0). (a) The entire chondrule. (b) High-magnification image. The white phases are metal and sulfides.
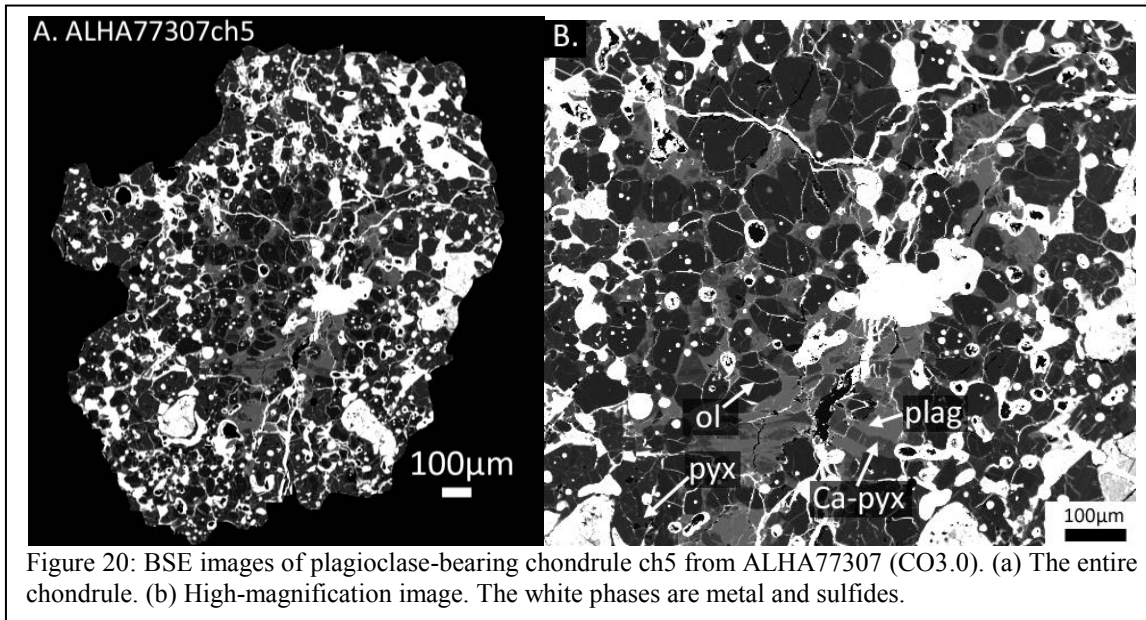
Experimental Results

1600˚C Peak temperature experiments

Eleven experiments were conducted with a peak temperature of 1600˚C, and with a range of linear cooling rates including 25˚C/hr, 10˚C/hr, and 5˚C/hr. Several experiments were cooled at a higher rate through the temperature range of 1600˚C to 1000˚C, followed by a slower cooling stage through the lower temperature range. Cooling histories of each experiment are illustrated in Figure 21 and details are given in Table 7. Linear cooling experiments were quenched at temperatures of 650°C to 1000°C. In addition, we ran a quench experiment in order to assess the state of the charge at the onset of cooling. This experiment was melted at 1600˚C for about 10 minutes, and then quenched in air.

Run products were 1 to 3mm across. Most experiments contain large vesicles. The result of the experiment quenched from 1600˚C is shown in Figure 22. The charge

consists mostly of elongate quench crystals of olivine. It contains only very few small

olivine crystals, and no residual starting materials. These features indicate that the charge

was very close to being completely melted after ten minutes at 1600˚C.

A range of porphyritic textures was observed in the dynamic cooling experiments,

examples of which are shown in Figures 22 to 26. The most common texture consists of

abundant olivine grains, some of which are poikilitically enclosed within large (~50μm to

500μm) low-Ca pyroxene grains. Olivine grain size ranges from several μm to 100μm.

Ca-pyroxene overgrowths on low-Ca pyroxene are common, and range in grain size from

~10μm to ~60μm. Glass is present in all run products: in two run products (exp12 and

exp14 – see Figure 25) the glass contains abundant quench crystals, while other runs
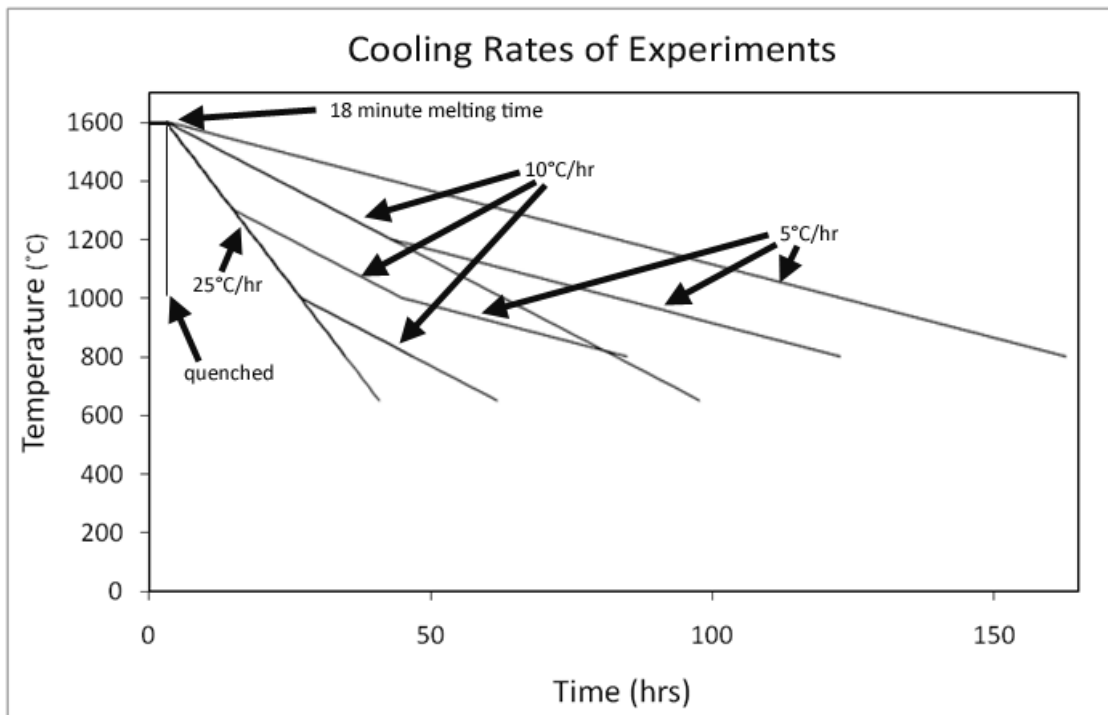
Figure 21: Schematic plot showing range of cooling histories of experiments.

Table 7: Cooling Rates for each Experiment			
Experiment	Segment 1	Segment 2	Segment 3
exp1	Quench		
exp2	25˚C/hr → 1000˚C		
exp6	25˚C/hr → 800˚C		
exp7	25˚C/hr → 1000˚C	10˚/hr → 800˚C	
exp8	25˚C/hr → 1300˚C	10˚/hr → 1000˚C	5˚/hr → 800˚C
exp9	25˚C/hr → 800˚C		
exp10	10˚C/hr → 1200˚C	5˚/hr → 800˚C	
exp11	25˚C/hr → 650˚C		
exp12	10˚C/hr → 650˚C		
exp13	25˚C/hr → 1000˚C	10˚/hr → 650˚C	
exp14	5˚C/hr → 800˚C		
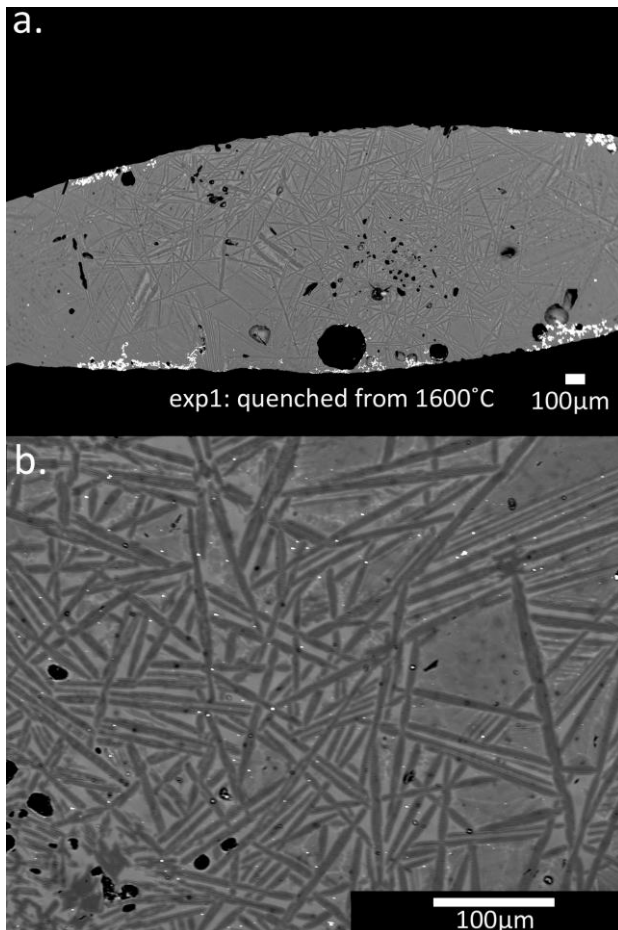
Figure 22: BSE image of exp1, which was quenched from 1600˚C. (a) Low-magnification image. (b) High-magnification image showing ubiquitous elongate quench crystals. White phase is Re ribbon which held the sample during the experiment.

contain a clean glass. Although the experiments were conducted at low fO_2, run products did not contain Fe metal.

Tables 8 to 12 show the average compositions of each phase present in the experiments. Plots showing compositional trends are included in the Discussion below. Most experiments contained glass, olivine, low-Ca pyroxene, and Ca-pyroxene. Many experiments also contained pyroxene grains with a calcium content intermediate to low-Ca pyroxene and Ca-pyroxene, with CaO contents of 1.8 wt. % to 4.0 wt. %. This phase is referred to here as "pigeonite" however its mineral structure has not been examined to actually determine if it is pigeonite. Not all experiments contain all of the phases discussed. An effort was made to ensure that the experimental charges were cut in order to observe the representative texture, avoiding such effects as crystal settling, but in some cases this may not have been achieved. In order to verify that all phases were accounted for, we made mixing plots (Figure 27) for experimental charges. These indicate that the sum of the observed phases add up to the bulk composition. However, this may not be the case for exp9 (not plotted on mixing plot in Figure 27). This experiment was very tiny and after polishing it, a very small amount was left at the very bottom of the sample. Therefore it is possible that we are seeing the early olivine crystals that settled to the bottom of the charge and other phases could have been present above this region.

In the two experiments (exp12, exp14) that contained extensive quench crystals instead of a clean glass, mesostasis was difficult to analyze. The analyses of the glass reported for these experiments in Table 12 were made on areas that did not contain
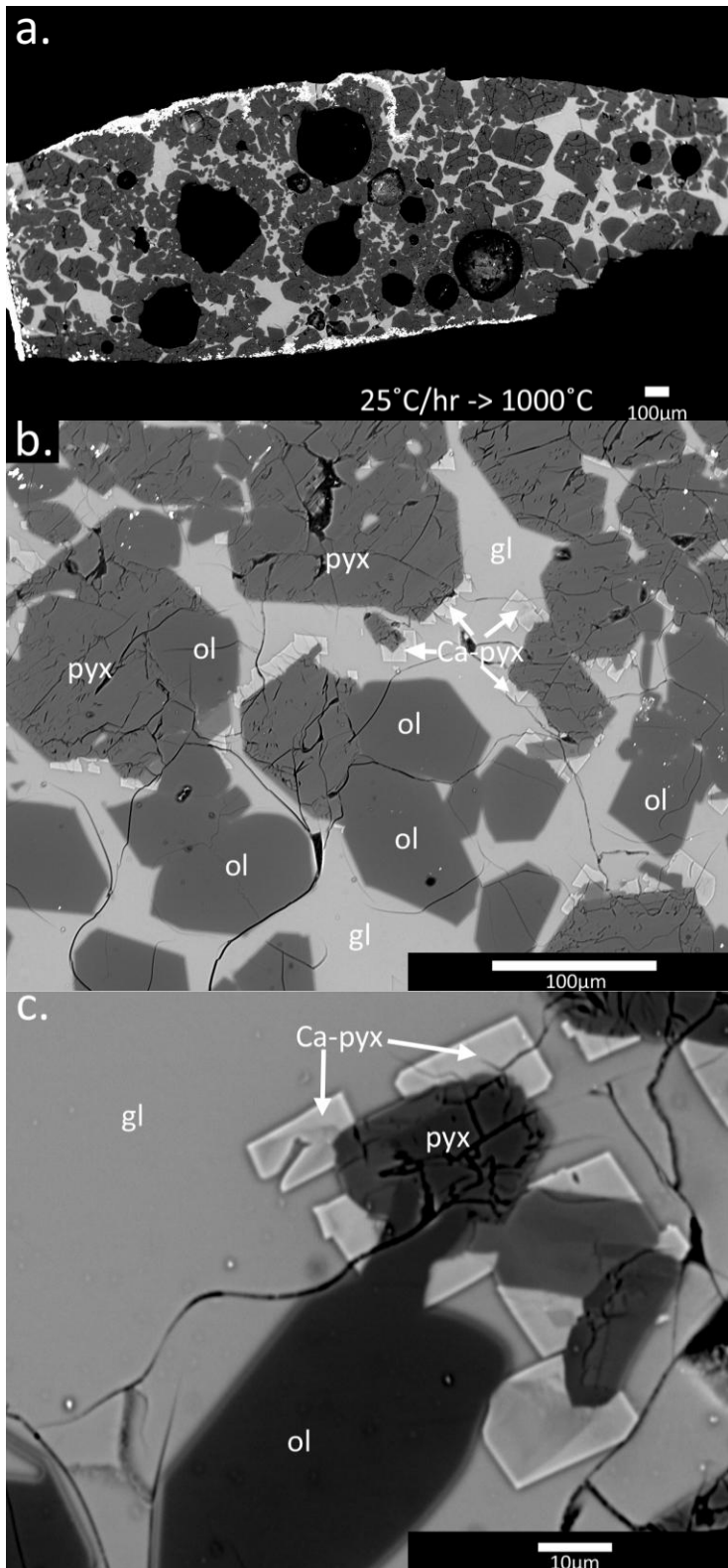
Figure 23: BSE images of exp2, which was heated to a peak T of 1600˚C, held for 18 minutes, and cooled at a rate of 25˚C/hr to 1000˚C before quenching. (a) The entire charge. (b) Representative image of the texture, consisting of olivine (ol) and low-Ca pyroxene (pyx) grains with Ca-pyroxene (Ca-pyx) overgrowths in a glass matrix (gl). (c) High-magnification image of Ca-pyroxene overgrowths on a low-Ca pyroxene grains.
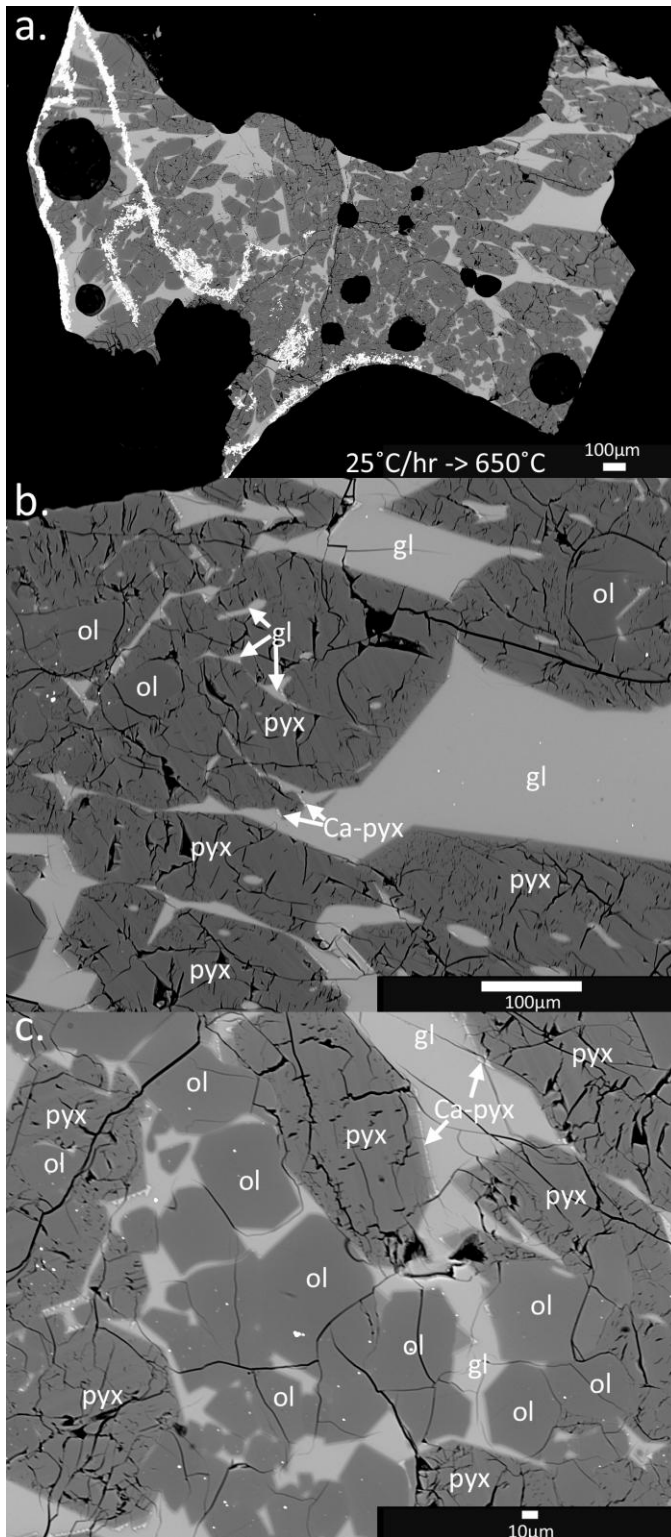
Figure 24: BSE images of exp11, which was heated to a peak T of 1600°C, held for 18 minutes, and cooled at a rate of 25°C/hr to 650°C before quenching. (a) The entire charge. (b,c) Representative images of the texture of exp11. Olivine (ol) grains are commonly poikilitically enclosed in large low-Ca pyroxene (pyx) grains with Ca-pyroxene (Ca-pyx) overgrowths in a glass matrix (gl). Pyroxene can be distinguished from olivine by the shrinkage cracks within pyroxene grains.
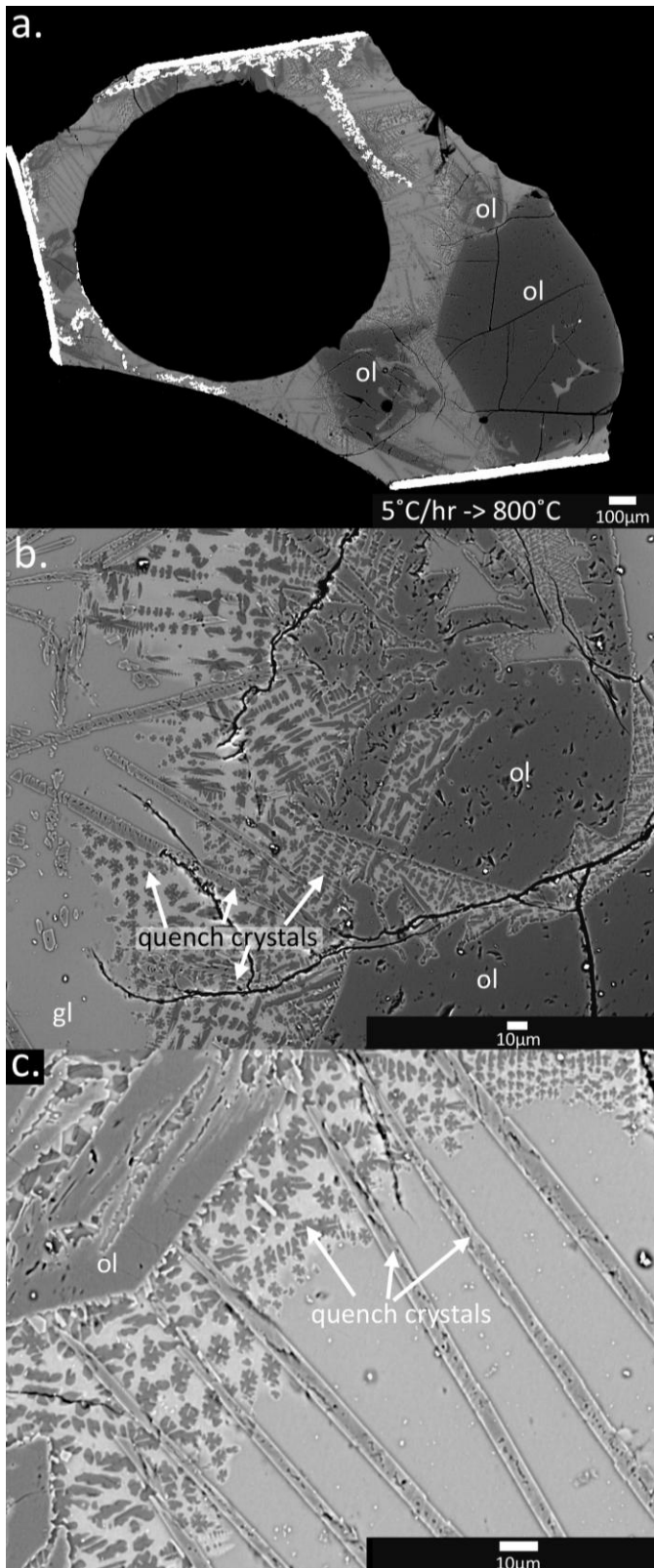
Figure 25: BSE images of exp14, which was heated to a peak T of 1600˚C, held for 18 minutes, and cooled at a rate of 5˚C/hr to 800˚C before quenching. (a) The entire charge, which contains a large vesicle and several large olivine grains. (b) Olivine (ol) grains with a hopper texture surrounded by quench crystals (c) High-magnification image of quench crystals.
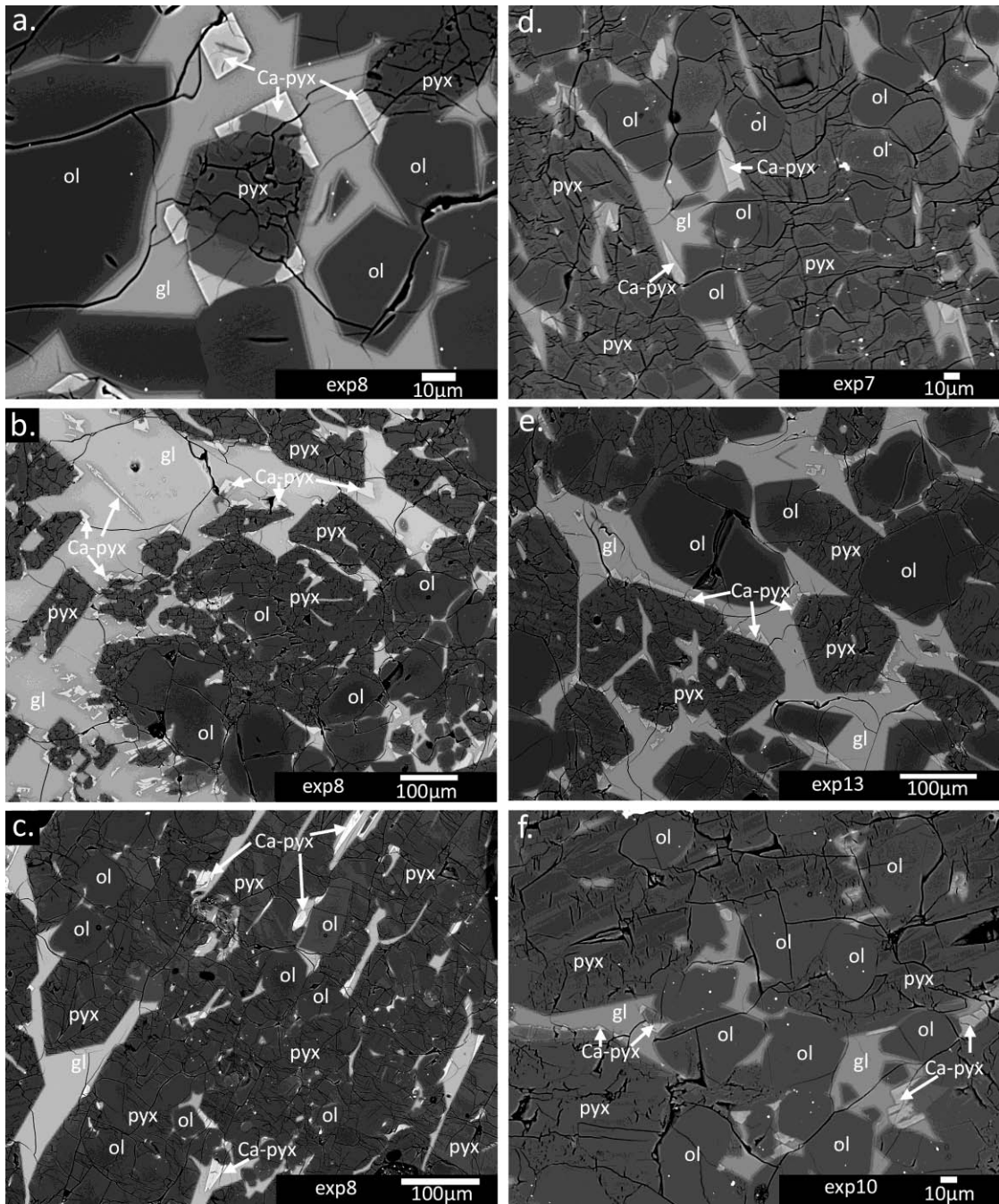
Figure 26: BSE images of typical textures from experimental runs. (a, b, c) exp8 (d) exp7. (e) exp13. (f) exp10. All of these experiments contained textures including olivine poikilitically enclosed within low-Ca pyroxene grains, and Ca-pyroxene overgrowths on low-Ca pyroxene grains.

Table 8: Olivine compositions from experiments

wt. % oxide	exp2	exp6	exp7	exp8	exp9
SiO2	41.57 (0.44)	42.12 (0.26)	42.60 (0.10)	43.27 (0.19)	42.50 (0.13)
TiO2	BD	BD	BD	BD	BD
Al2O3	0.03 (0.01)	BD	BD	BD	BD
Cr2O3	0.29 (0.02)	0.29 (0.02)	0.26 (0.02)	0.27 (0.04)	0.33 (0.05)
FeO	1.45 (0.28)	2.10 (0.25)	1.20 (0.50)	1.42 (0.49)	2.03 (0.30)
MnO	0.08 (0.02)	0.09 (0.02)	0.07 (0.02)	0.10 (0.03)	0.09 (0.01)
MgO	55.67 (0.45)	54.45 (0.36)	55.35 (0.45)	55.84 (0.60)	54.52 (0.35)
CaO	0.07 (0.02)	0.11 (0.03)	0.08 (0.03)	0.08 (0.02)	0.10 (0.02)
Na2O	BD	BD	BD	BD	BD
Total	99.16	99.17	99.60	100.98	99.59
Fo	98.56	97.89	98.79	98.59	97.95
Fa	1.44	2.11	1.21	1.41	2.05
Analyses	19	32	10	12	24

wt. % oxide	exp10	exp11	exp12	exp13	exp14
SiO2	42.65 (0.19)	41.7 (0.21)	41.55 (0.38)	41.94 (0.16)	42.41 (0.39)
TiO2	BD	BD	BD	BD	BD
Al2O3	0.03 (0.00)	0.04 (0.02)	0.04 (0.01)	0.04 (0.01)	BD
Cr2O3	0.26 (0.01)	0.30 (0.02)	0.28 (0.08)	0.29 (0.03)	0.24 (0.06)
FeO	2.22 (0.57)	1.41 (0.44)	1.58 (0.54)	1.17 (0.40)	2.22 (0.85)
MnO	0.08 (0.02)	0.09 (0.02)	0.07 (0.02)	0.08 (0.02)	0.06 (0.03)
MgO	55.05 (0.54)	56.66 (0.53)	56.54 (0.54)	56.93 (0.44)	55.11 (0.99)
CaO	0.08 (0.03)	0.07 (0.03)	0.08 (0.02)	0.08 (0.02)	0.11 (0.03)
Na2O	BD	BD	BD	BD	BD
Total	100.37	100.28	100.13	100.51	100.16
Fo	97.79	98.62	98.46	98.86	97.79
Fa	2.21	1.38	1.54	1.14	2.21
Analyses	12	19	23	14	31

Compositions are averages of the number of analyses given. Values in parentheses are one standard deviation for that average. BD indicates the value is below the detection limit.

Table 9: Low-Ca pyroxene compositions from experiments					
wt. % oxide	exp2	exp6	exp7	exp8	exp9
SiO2	56.32 (5.68)	59.06 (0.34)	59.35 (0.21)	58.52 (5.13)	
TiO2	BD	BD	BD	BD	
Al2O3	0.88 (0.81)	0.59 (0.13)	0.78 (0.15)	0.73 (0.40)	
Cr2O3	0.51 (0.12)	0.48 (0.06)	0.64 (0.09)	0.58 (0.15)	
FeO	1.07 (0.49)	1.11 (0.17)	1.13 (0.13)	1.21 (0.31)	
MnO	0.09 (0.03)	0.06 (0.01)	0.09 (0.02)	0.09 (0.02)	
MgO	40.08 (5.60)	37.83 (0.30)	37.74 (0.40)	39.71 (5.11)	
CaO	0.24 (0.15)	0.23 (0.05)	0.27 (0.03)	0.25 (0.11)	
Na2O	BD	BD	BD	BD	
Total	99.09	99.37	100.01	101.10	
Fs	1.40	1.62	1.64	1.67	
En	98.20	97.95	97.85	97.90	
Wo	0.41	0.43	0.51	0.43	
Analyses	16	8	13	11	
wt. % oxide	exp10	exp11	exp12	exp13	exp14
SiO2	59.18 (0.80)	58.23 (0.62)	57.38	58.51 (0.54)	
TiO2	BD	BD	0.05	BD	
Al2O3	0.97 (0.69)	0.78 (0.47)	2.55	0.67 (0.13)	
Cr2O3	0.51 (0.16)	0.58 (0.13)	1.67	0.55 (0.06)	
FeO	1.37 (0.30)	0.87 (0.19)	2.89	0.84 (0.13)	
MnO	0.07 (0.02)	0.08 (0.03)	0.20	0.09 (0.02)	
MgO	38.06 (0.46)	39.15 (0.47)	32.80	39.11 (0.39)	
CaO	0.23 (0.09)	0.20 (0.08)	2.64	0.22 (0.04)	
Na2O	BD	BD	0.05	BD	
Total	100.39	99.90	100.24	99.99	
Fs	1.97	1.23	4.46	1.18	
En	97.61	98.41	90.31	98.41	
Wo	0.42	0.36	5.22	0.40	
Analyses	15	13	R	11	

Compositions are averages of the number of analyses given, or in some cases, one representative analysis was chosen (indicated by an R in the Analyses row). Values in parentheses are one standard deviation for that average. For those experiments with no data, there was insufficient low-Ca pyroxene to analyze. BD indicates the value is below the detection limit.

Table 10: Pigeonite compositions from experiments

wt. % oxide	exp2	exp6	exp7	exp8	exp9
SiO2	55.66 (0.80)	55.21 (0.37)		57.65 (1.99)	
TiO2	0.03 (0.00)	0.07 (0.01)		0.05 (0.02)	
Al2O3	4.29 (0.82)	4.75 (0.33)		3.24 (2.48)	
Cr2O3	1.42 (0.18)	1.61 (0.04)		1.09 (0.37)	
FeO	1.69 (0.13)	1.74 (0.06)		2.10 (0.32)	
MnO	0.18 (0.02)	0.11 (0.01)		0.15 (0.02)	
MgO	33.81 (0.73)	33.68 (0.09)		34.61 (1.55)	
CaO	2.25 (0.24)	2.24 (0.14)		1.84 (0.61)	
Na2O	BD	BD		BD	
Total	99.31	99.41		100.71	
Fs	2.60	2.69		3.17	
En	92.95	92.87		93.27	
Wo	4.44	4.44		3.56	
Analyses	6	2		13	

wt. % oxide	exp10	exp11	exp12	exp13	exp14
SiO2	52.47 (1.23)	52.26 (0.79)		54.10 (1.12)	
TiO2	0.12 (0.04)	0.08 (0.02)		0.05 (0.02)	
Al2O3	10.02 (2.54)	8.11 (1.71)		6.74 (1.36)	
Cr2O3	1.19 (0.29)	1.70 (0.31)		1.84 (0.23)	
FeO	2.49 (0.30)	2.14 (0.24)		1.73 (0.35)	
MnO	0.13 (0.02)	0.21 (0.03)		0.17 (0.03)	
MgO	32.68 (1.16)	33.36 (0.64)		34.38 (1.10)	
CaO	1.85 (0.58)	2.14 (0.58)		2.13 (0.44)	
Na2O	BD	BD		BD	
Total	100.95	100.02		101.13	
Fs	3.94	3.33		93.23	
En	92.29	92.40		4.15	
Wo	3.77	4.27		97.37	
Analyses	9	13		7	

Compositions of pigeonite present in experiments. Values are averages of the number of analyses given. Values in parentheses are one standard deviation for that average. For those experiments with no data, there was insufficient pigeonite to analyze. BD indicates the value is below the detection limit.

wt. % oxide	exp2	exp6	exp7	exp8	exp9
SiO2	50.10 (1.69)	54.65 (2.23)	52.34 (1.18)	51.87 (2.40)	
TiO2	0.24 (0.07)	0.09 (0.05)	0.19 (0.06)	0.22 (0.10)	
Al2O3	9.75 (2.50)	3.88 (1.45)	5.62 (1.85)	7.63 (3.65	
Cr2O3	1.18 (0.34)	1.33 (0.26)	1.48 (0.62)	1.46 (0.52)	
FeO	1.17 (0.17)	1.81 (0.15)	1.58 (0.27)	1.63 (0.33)	
MnO	0.18 (0.02)	0.15 (0.02)	0.20 (0.03)	0.17 (0.04)	
MgO	17.97 (2.21)	19.85 (1.65)	18.49 (2.16)	18.31 (3.51)	
CaO	19.17 (1.62)	18.02 (2.32)	20.25 (1.75)	19.36 (3.08)	
Na2O	0.04 (0.02)	0.15 (0.03)	0.11 (0.02)	0.09 (0.03)	
Total	99.78	99.92	100.24	100.74	
Fs	2.02	3.00	2.61	2.764196043	
En	55.44	58.71	54.46	55.19102958	
Wo	42.54	38.29	42.93	42.04477438	
Analyses	15	4	18	22	

wt. % oxide	exp10	exp11	exp12	exp13	exp14
SiO2	47.97 (0.95)	47.16 (1.35)		47.73 (1.22)	
TiO2	0.49 (0.10)	0.35 (0.05)		0.34 (0.08)	
Al2O3	14.10 (2.14)	14.76 (2.41)		13.02 (2.03)	
Cr2O3	0.65 (0.52)	1.07 (0.56)		1.53 (0.38)	
FeO	1.98 (0.37)	1.32 (0.15)		1.07 (0.14)	
MnO	0.16 (0.03)	0.20 (0.02)		0.18 (0.03)	
MgO	15.71 (1.71)	16.87 (3.80)		16.04 (1.87)	
CaO	19.45 (1.08)	18.14 (2.74)		20.55 (1.25)	
Na2O	0.12 (0.10)	0.16 (0.05)		0.09 (0.04)	
Total	100.63	100.01		100.53	
Fs	3.61	0.84		1.92	
En	51.02	1.51		51.04	
Wo	45.37	97.65		47.04	
Analyses	5	11		16	

Table 11: Ca-Pyroxene compositions from experiments

Compositions of Ca-pyroxene present in experiments. Values are averages of the number of analyses given. Values in parentheses are one standard deviation for that average. For those experiments with no data, there was insufficient Ca-pyroxene to analyze. BD indicates the value is below the detection limit.

Table 12: Glass compositions from experiments

wt. % oxide	exp2	exp6	exp7	exp8	exp9	exp10
SiO2	55.51 (0.71)	60.55 (1.55)	61.48 (4.14)	60.4 (2.95)	70.62 (0.81)	56.87 (0.94)
TiO2	0.17 (0.01)	0.19 (0.01)	0.15 (0.02)	0.17 (0.03)	0.14 (0.03)	0.24 (0.01)
Al2O3	22.09 (1.16)	20.29 (1.69)	20.15 (3.41)	20.82 (2.62)	12.85 (0.16)	22.79 (0.64)
Cr2O3	0.06 (0.04)	0.06 (0.02)	BD	0.07 (0.04)	0.21 (0.02)	BD
FeO	1.43 (0.15)	1.50 (0.54)	1.79 (0.49)	2.30 (0.44)	0.90 (0.12)	2.37 (0.34)
MnO	0.13 (0.01)	0.07 (0.02)	0.08 (0.02)	0.11 (0.02)	0.05 (0.01)	0.09 (0.01)
MgO	5.36 (0.37)	3.40 (1.14)	2.99 (0.61)	3.35 (0.52)	3.01 (0.32)	3.6 (0.40)
CaO	14.03 (0.22)	10.81 (0.80)	10.79 (1.61)	11.48 (0.92)	9.04 (0.27)	12.06 (0.48)
Na2O	0.30 (0.02)	1.78 (0.11)	1.34 (0.13)	1.30 (0.10)	1.14 (0.06)	1.12 (0.07)
K2O	0.58 (0.04)	1.33 (0.10)	1.18 (0.12)	1.07 (0.08)	0.89 0.04)	1.09 (0.07)
P2O5	0.04 (0.01)	0.05 (0.01)	0.06 (0.01)	0.05 (0.01)	BD	BD
SO3	BD	BD	BD	BD	BD	BD
NiO	BD	BD	BD	BD	BD	BD
Total	99.71	100.02	100.00	101.05	98.86	100.26
Analyses	11	14	12	9	8	14

wt. % oxide	exp11	exp12	exp13	exp14	Normative Minerals	Wt% Norm Exp13
SiO2	57.25 (1.17)	72.06 (0.91)	57.58 (0.81)	72.08 (1.71)		
TiO2	0.20 (0.02)	0.19 (0.03)	0.18 (0.02)	0.2 (0.02)		
Al2O3	20.99 (1.15)	13.64 (1.05)	22.08 (1.29)	13.56 (0.88)	Quartz	16.48
Cr2O3	0.08 (0.04)	0.13 (0.08)	0.07 (0.04)	0.12 (0.05)	Plagioclase	61.03
FeO	1.96 (0.21)	1.10 (0.35)	1.69 (0.28)	0.72 (0.26)	Orthoclase	4.79
MnO	0.12 (0.02)	0.06 (0.01)	0.12 (0.01)	0.04 (0.01)	Diopside	8.46
MgO	4.61 (0.61)	2.94 (0.96)	4.28 (0.58)	1.89 (0.63)	Hypersthene	9.36
CaO	12.05 (0.45)	7.35 (0.73)	13.13 (0.39)	7.60 (2.57)	Ilmenite	0.34
Na2O	1.01 (0.07)	1.21 (0.23)	0.80 (0.04)	1.06 (0.46)	Magnetite	0.13
K2O	0.96 (0.04)	1.26 (0.34)	0.81 (0.06)	1.34 (0.56)	Apatite	0.09
P2O5	0.05 (0.01)	BD	0.04 (0.01)	NA	Chromite	0.15
SO3	BD	BD	BD	NA		
NiO	BD	BD	BD	NA		
Total	99.26	99.94	100.76	98.57		
Analyses	10	9	11	18	Total	100.83

Compositions of glass present in experiments. Values are averages of the number of analyses given. Values in parentheses are one standard deviation for that average. BD indicates the value is below the detection limit. Normative mineralogy of the glass from one representative experiment, exp13, is shown at the bottom right.

Figure 27: Mixing plot showing MgO vs SiO$_2$ compositions of each phase present in experiments. The sum of the phase compositions agrees with the bulk composition. Glass points with open symbols contained quench crystals; therefore these points are probably not representative of true liquid compositions.
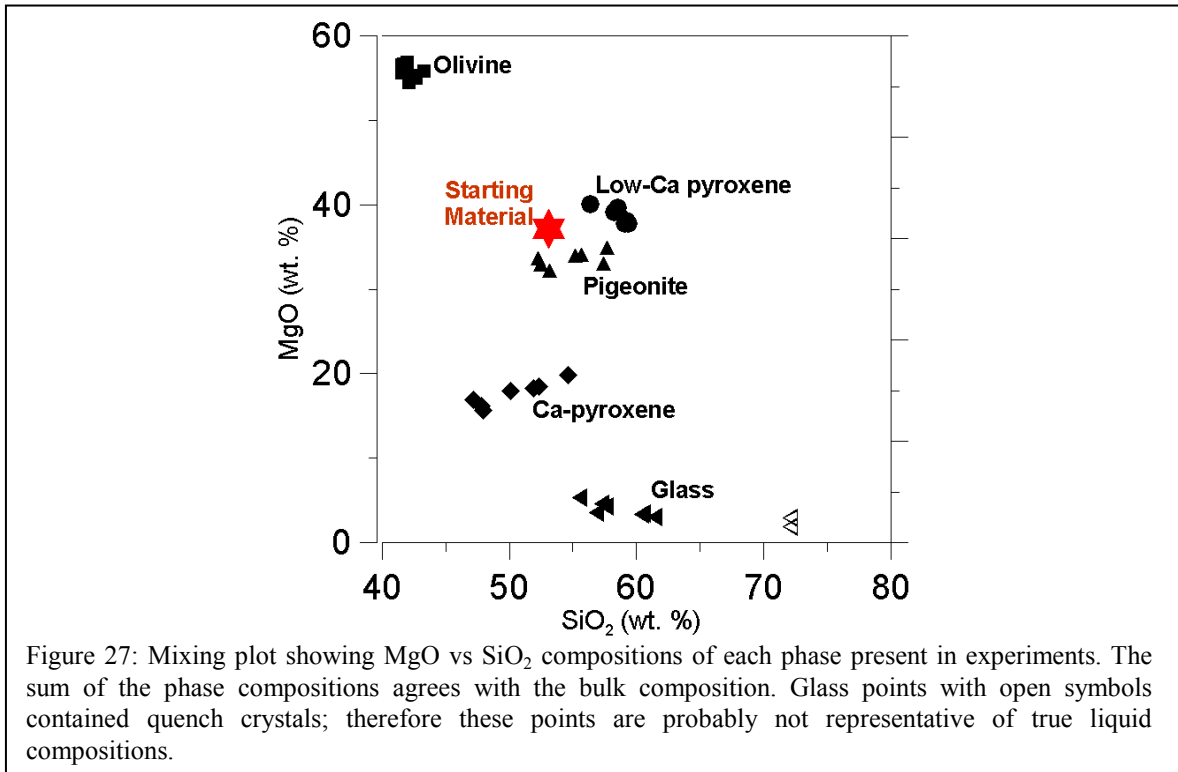
quench crystals. These compositions are probably not really representative of the residual liquid that was present at the quench temperature before the quench crystals formed.

All the experiments with peak temperatures of 1600˚C experienced Na-loss during the duration of the run, as the measured Na content of the glass is less than is expected based on the bulk Na$_2$O content of the starting material. The starting composition was 0.24 wt. % Na$_2$O, and virtually all Na$_2$O should go into the melt as it is incompatible in olivine and pyroxene. Therefore, for a typical experiment containing approximately 10 vol. % glass, the expected concentration of Na$_2$O in the glass should be ~2.4 wt%. The observed values however, are 0.3 wt. % to 1.8 wt. % Na$_2$O (Table 12).

Sodium-rich atmosphere experiments

Two experiments were conducted in the presence of a Na-rich atmosphere (nexp21, nexp22). These experiments were heated to a peak temperature of 1500°C and

then either quenched (nexp22), or cooled at a rate of 25°C/hour (nexp21). The quenched experiment (Figure 28) contained numerous small olivine crystals, suggesting that it was not completely melted at the peak temperature, and abundant dendritic quench crystals in a glassy matrix.

Experiment nexp21 was cooled at 25°C/hour from a peak temperature of 1500°C to a quench temperature of 900°C. This charge contains olivine, low-Ca pyroxene, Ca-pyroxene, and glass (Figure 29). Olivine grains are common and are typically 10 to 25 micrometers in diameter. Low-Ca pyroxene is coarser grained than olivine, typically hundreds of micrometers in diameter. Olivine grains are typically poikilitically enclosed within low-Ca pyroxene grains. Ca-pyroxene occurs as overgrowths on low-Ca pyroxene grains.

Compositions of major phases in nexp21 and nexp22 experiments are reported in Tables 13 and 14. These experiments contain very low Fe contents due to Fe loss to the Pt pocket. The Na content of the glass in the slow-cooled experiment nexp21, 4.04 wt. % Na_2O, is significantly higher than experiments conducted without a Na-rich atmosphere, 0.30 to 1.78 wt. % Na_2O (Table 12). The Na_2O content of the glass in the experiment that was quenched from 1500˚C was low, at 0.36 wt. % Na_2O. This is presumably due to the fact that the short melting time at the peak temperature was not long enough to allow the Na-rich atmosphere to equilibrate with the melt.

Anorthite seed experiments

Two experiments were conducted with a starting material containing anorthite seeds. Exp24 was heated to 1600°C and immediately quenched, and exp25 was heated to
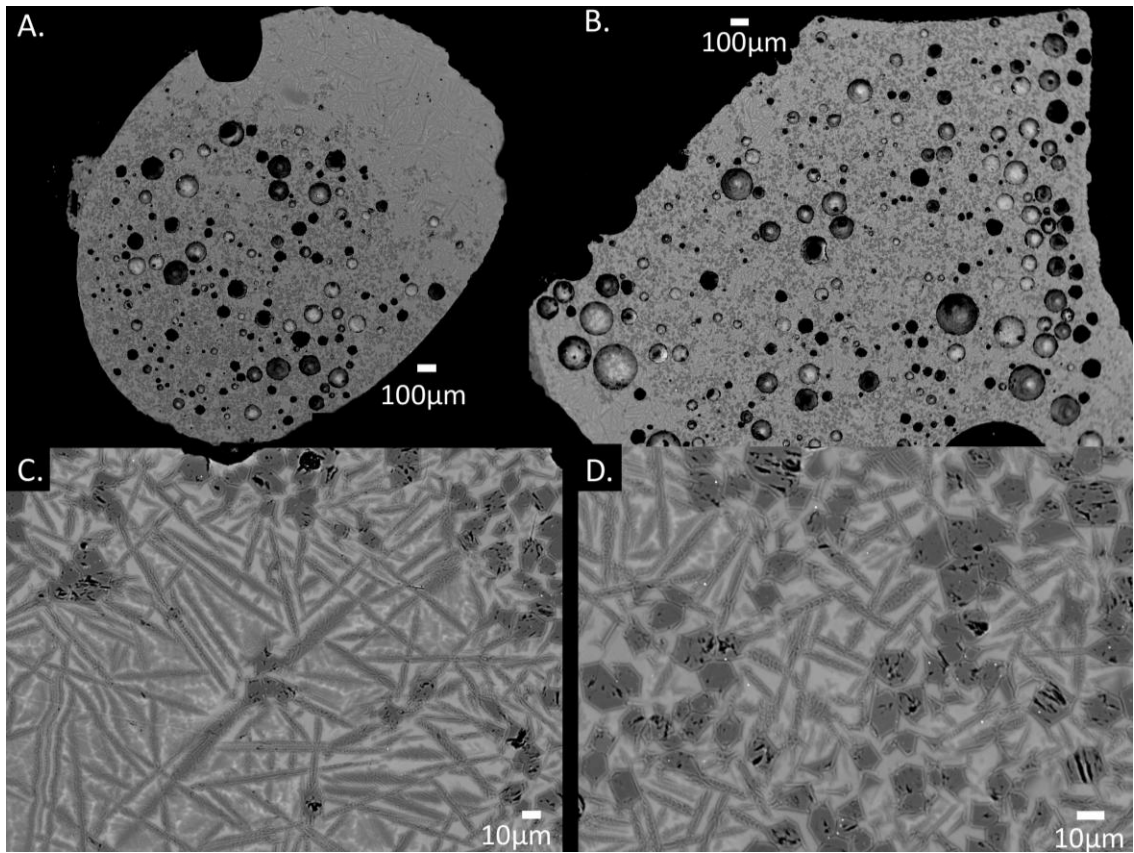
Figure 28: BSE images of nexp22, which was heated in a Na-rich atmosphere to a peak temperature of 1500°C and then quenched. (a,b) Low magnification images: dark spots are vesicles. (c,d) High-magnification BSE images of the texture. The experiment consists of small olivine crystals with abundant quench crystals.

1600°C, melted for 18 minutes, and then cooled at 25°C/hour to a quench temperature of

800°C. Figure 30 shows exp24, the quench experiment. The quench experiment

contained elongate skeletal olivine crystals that presumably grew during quenching.

Exp24 also contained finer grained olivines that probably are grains that grew during

heating. Anorthite seed crystals are not present in this experiment, indicating that the

anorthite seeds were melted completely either during heating or during the time spent at

the peak temperature.

Exp25 (Figure 31 and 32) contains large olivine grains hundreds of micrometers in

diameter. Neither pyroxene nor plagioclase was observed. The matrix consists of glass

and abundant quench crystals. Compositions of olivine and glass in exp25 are given in

Table 15. Glass analyses were obtained on areas of clean glass with no quench crystals,

therefore they probably do not represent the composition of the true melt at the time of

quenching.
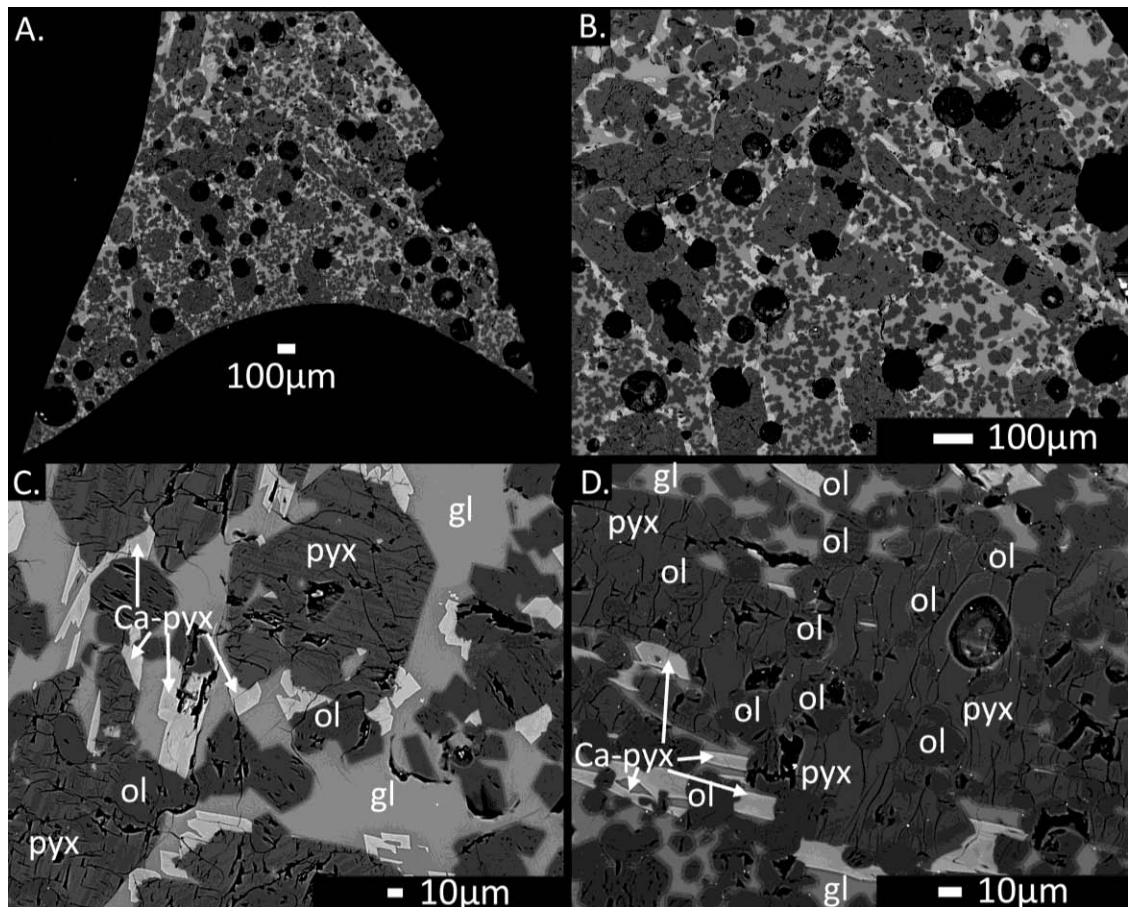
Figure 29: BSE images of nexp21, which was cooled in a Na-rich atmosphere at 25°C/hour from a peak temperature of 1500°C to a quench temperature of 900°C. (a,b) Low-magnification BSE images of the charge. Dark spots are vesicles. The coarse-grained phase is low-Ca pyroxene, the fine-grained phase is olivine, and the light grey phase is glass. (c,d) High-magnification BSE images of the texture, including fine-grained olivine poikilitically enclosed in coarse-grained pyroxene.

Table 13: Compositions of exp22 phases		
wt. % oxide	Olivine	Glass
SiO2	42.74 (0.73)	57.18 (0.70)
TiO2	BD	0.06 (0.01)
Al2O3	0.29 (0.25)	6.67 (0.30)
Cr2O3	0.29 (0.05)	0.45 (0.08)
FeO	0.14 (0.05)	0.11 (0.08)
MnO	0.07 (0.02)	0.15 (0.01)
MgO	55.70 (1.18)	30.32 (1.35)
CaO	0.20 (0.15)	5.08 (0.24)
Na2O	BD	0.36 (0.05)
K2O	NA	0.06 (0.01)
Total	99.41	100.44
	Fo 99.89	
	Fa 0.11	
Analyses	4	4
C.R.	quench	
Peak T	1500°C	

Each composition is an average of four individual analyses. Values in parentheses are one standard deviation for that average. Mesostasis composition is from a broad-beam (30μm) analysis of glass plus quench crystals. BD indicates concentration is below the detection limit. NA indicates this element was not analyzed.

Table 14: Compositions of exp21 phases					
wt. % oxide	Olivine	Low-Ca Pyx	Pigeonite	Ca-pyroxene	Glass
SiO2	42.00 (0.41)	59.00 (0.43)	57.64 (1.02)	53.99 (1.91)	64.93 (1.96)
TiO2	BD	BD	BD	0.09 (0.04)	0.11 (0.03)
Al2O3	0.09 (0.17)	0.50 (0.23)	3.01 (2.96)	3.44 (1.34)	18.78 (1.23)
Cr2O3	0.09 (0.06)	0.15 (0.06)	0.09 (0.02)	0.28 (0.19)	BD
FeO	BD	BD	BD	BD	BD
MnO	0.07 (0.02)	0.05 (0.02)	BD	0.07 (0.03)	0.05 (0.01)
MgO	58.19 (0.41)	40.34 (0.57)	35.57 (3.17)	24.68 (5.18)	3.08 (0.71)
CaO	0.18 (0.13)	0.43 (0.17)	4.02 (0.99)	16.99 (3.96)	9.01 (0.84)
Na2O	BD	BD	0.17 (0.16)	0.21 (0.10)	4.04 (0.21)
K2O	NA	NA	NA	NA	0.44 (0.15)
Total	100.63	100.48	100.56	99.74	100.43
	Fo 99.99	Fs 0.02	Fs 0.02	Fs 0.05	
	Fa 0.01	En 99.22	En 92.47	En 66.76	
		Wo 0.77	Wo 7.51	Wo 33.19	
Analyses	12	15	2	17	18
C.R.	25°C/hr -> 900				
Peak T	1500°C				

Compositions are averages of the number of individual analyses given. Values in parentheses are one standard deviation for the average. BD indicates concentration is below the detection limit. NA indicates that this element was not analyzed.
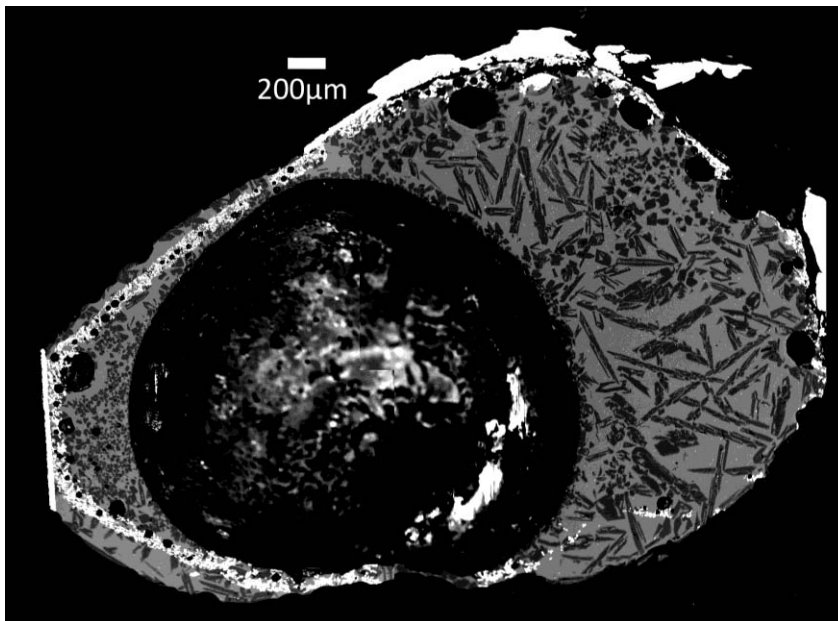
Figure 30: BSE image of exp24, the seeding experiment, which was heated to 1600°C and immediately quenched. The white material is Re ribbon which held the charge, the light phase is glass, the dark phase is olivine, and the large round spot in the center is a vesicle.
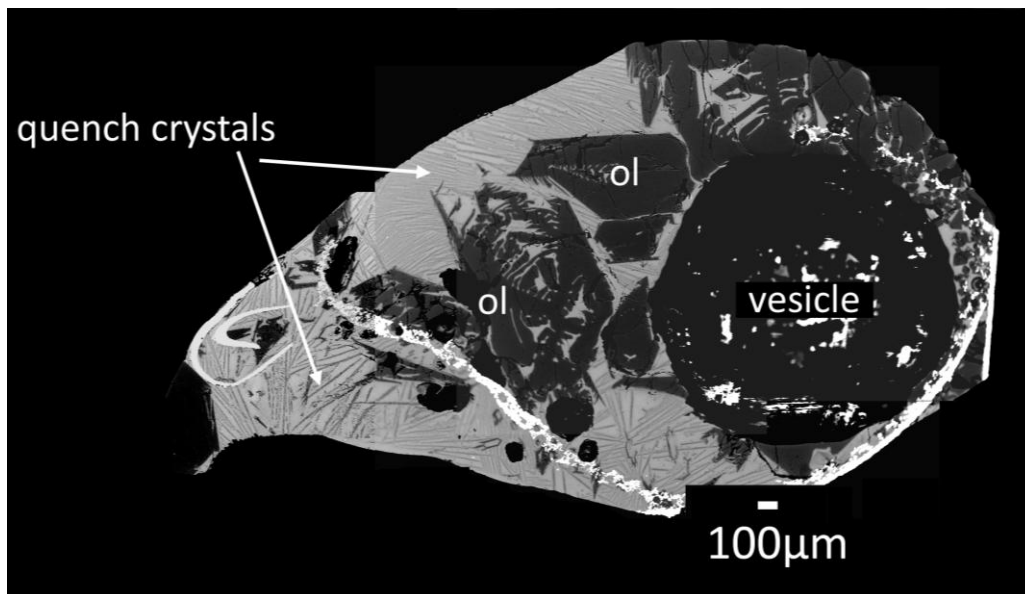
Figure 31. BSE image of exp25. Very bright phase is Re ribbon that held the charge during the experiment. Dark phase is olivine in a lighter matrix of fine grained quench crystals.
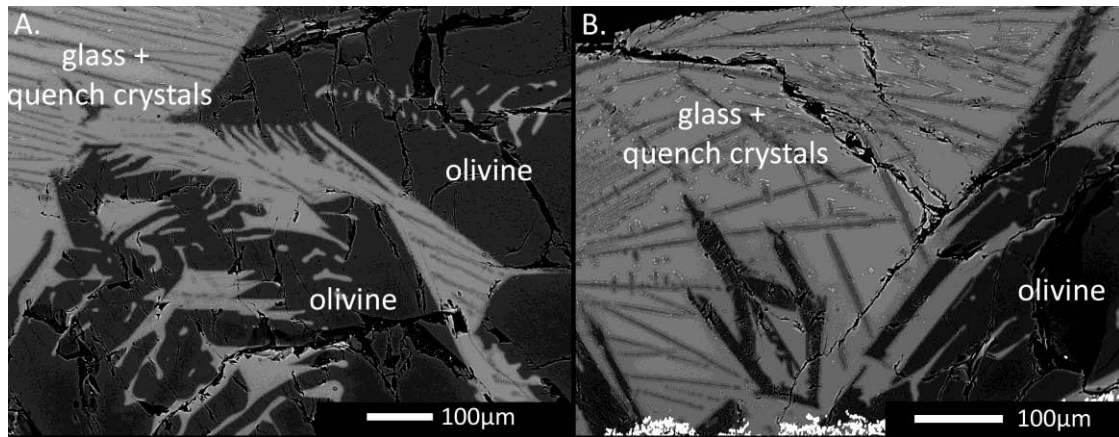
Figure 32. High-magnification BSE images of exp25, which was cooled at 25°C/hour from a peak temperature of 1600°C to a quench temperature of 800°C. Olivine is present in a matrix of glass and fine-grained quench crystals.

Table 15: Compositions of exp25 phases		
wt. % oxide	Olivine	Glass
SiO2	42.27 (0.33)	69.53 (0.32)
TiO2	BD	0.08 (0.01)
Al2O3	0.02 (0.01)	9.87 (0.25)
Cr2O3	0.37 (0.13)	0.45 (0.03)
FeO	1.47 (0.56)	0.69 (0.01)
MnO	0.10 (0.03)	0.10 (0.71)
MgO	55.33 (0.65)	6.38 (0.71)
CaO	0.11 (0.01)	10.64 (0.18)
Na2O	BD	0.18 (0.01)
K2O	NA	0.17 (0.00)
Total	99.67	98.10
	Fo 98.53	
	Fa 1.47	
Analyses	18	2
C.R.	25°C/hr -> 900	
Peak T	1600°C	

Compositions of phases present in exp25, which contained anorthite seeds in the starting material. Each is an average composition based on the number of individual analyses given. Values in parentheses are one standard deviation. Glass analyses were made on areas of clean glass with a 10μm beam diameter.

CHAPTER 4:

DISCUSSION

There have been many previous experimental studies of chondrules, most of which have investigated the reproduction of a wide range of chondrule textures, in order to determine cooling rates and peak temperatures experienced by chondrules (Hewins et al., 2005). A few of these studies have provided detailed descriptions of compositions, but most have focused on texture. Very few studies have focused on type IAB chondrules: Radomsky and Hewins (1990) investigated these compositions but did not discuss mineral compositions in detail, and did not give detailed descriptions of the textures they produced. Porphyritic olivine (PO) and porphyritic olivine and pyroxene (POP) textures have been reproduced experimentally at cooling rates of 10°C/hr and higher for peak temperatures below the liquidus. However, cooling rates of 100°C/hr to 1000°C/hr have been suggested as probable cooling rates for porphyritic chondrules in general (Hewins et al., 2005). It has also been suggested that porphyritic chondrules require peak heating temperatures below the liquidus in order to preserve sufficient nuclei for a porphyritic texture to develop. If complete melting takes place, seeding with dust is necessary to produce porphyritic textures (Radomsky & Hewins, 1990; Connolly & Hewins, 1995).

None of the previous experimental studies of chondrules have investigated the presence of plagioclase in type I chondrules. Because the presence of plagioclase may place specific constraints on formation conditions, we have investigated textures and compositions of natural type I chondrules, especially those containing primary plagioclase. We also studied experimental chondrule analogs, in order to constrain the

formation conditions of type I chondrules in general, and the conditions required for the formation of plagioclase in particular. In the following discussion, we will consider the relationship between plagioclase-bearing and plagioclase-free type I chondrules, then discuss the constraints that the textures and compositions of our experiments can put on chondrule formation. This is followed by a discussion of the occurrence of plagioclase in type I chondrules, and the constraints our experiments can put on its nucleation and growth in type I chondrules. We then investigate how the results of this study fit with current chondrule formation models.

Relationship between natural plagioclase-bearing chondrules and plagioclase-free chondrules

Plagioclase is observed commonly in type I chondrules in CO chondrites, in about 10% of chondrules (Jones, 1997). It occurs as single crystals that are visible optically. This plagioclase is most likely igneous. Although Kainsaz is thermally metamorphosed, plagioclase is also present in the unequilibrated chondrites ALHA77307 (CO3.0), and Yamato 81020 (CO3.0) (Tomeoka & Itoh, 2004), indicating it is indeed a primary mineral. Plagioclase is also predicted on the equilibrium crystallization sequence of a melt of type I chondrule composition by the MELTS software (Ghiorso & Sack, 1995 and Asimow & Ghiorso, 1998), as we discuss in more detail below. Type IAB chondrules that contain plagioclase and type I chondrules that do not contain plagioclase display a similar range of textures: both contain olivine often poikilitically enclosed in low-Ca pyroxene, and Ca-pyroxene overgrowths on low-Ca pyroxene (Figures 10 – 16). In order to understand what controls the presence or absence of plagioclase, we first

71

consider the compositional relationship between plagioclase-bearing and plagioclase-free chondrules.

A difference in bulk silicate composition could be responsible for the production of plagioclase in some chondrules and not others. Figure 33 compares our plagioclase-bearing type I chondrule bulk silicate compositions with plagioclase-free chondrule bulk silicate compositions of Berlin (2009), and a plagioclase-rich chondrule (PRC) (Berlin, 2009). The bulk silicate compositions of plagioclase-bearing chondrules are very similar to bulk silicate compositions of type I chondrules that do not contain plagioclase. The most significant difference between plagioclase-bearing chondrules and plagioclase-free chondrules is the Al:Ca ratio. This value is primarily greater than 1 for plagioclase-bearing chondrules (with one exception), while it is primarily less than 1 for plagioclase-free chondrules. This difference in composition may affect plagioclase nucleation, because the Al:Ca ratio of plagioclase is also greater than 1. However, there are exceptions to this trend, so this must not be the only factor. Chromium contents are also slightly different for plagioclase-bearing chondrules (slightly greater than CI) compared to plagioclase-free chondrules (slightly less than CI). However, there is no obvious reason why this difference would control the appearance of plagioclase.

Figure 33 also shows the bulk composition of a plagioclase-rich chondrule (PRC). The plagioclase-bearing type I chondrules are clearly distinct in composition from plagioclase-rich chondrules.

Figure 33: Abundance of elements in bulk silicate compositions relative to CI values (Anders & Grevesse, 1989) plotted in order of increasing volatility (except for Fe), for plagioclase-bearing chondrules (black lines, this study) compared to plagioclase-free chondrules (gray lines, Berlin, 2009) and one plagioclase-rich chondrule (dashed line, Berlin, 2009).
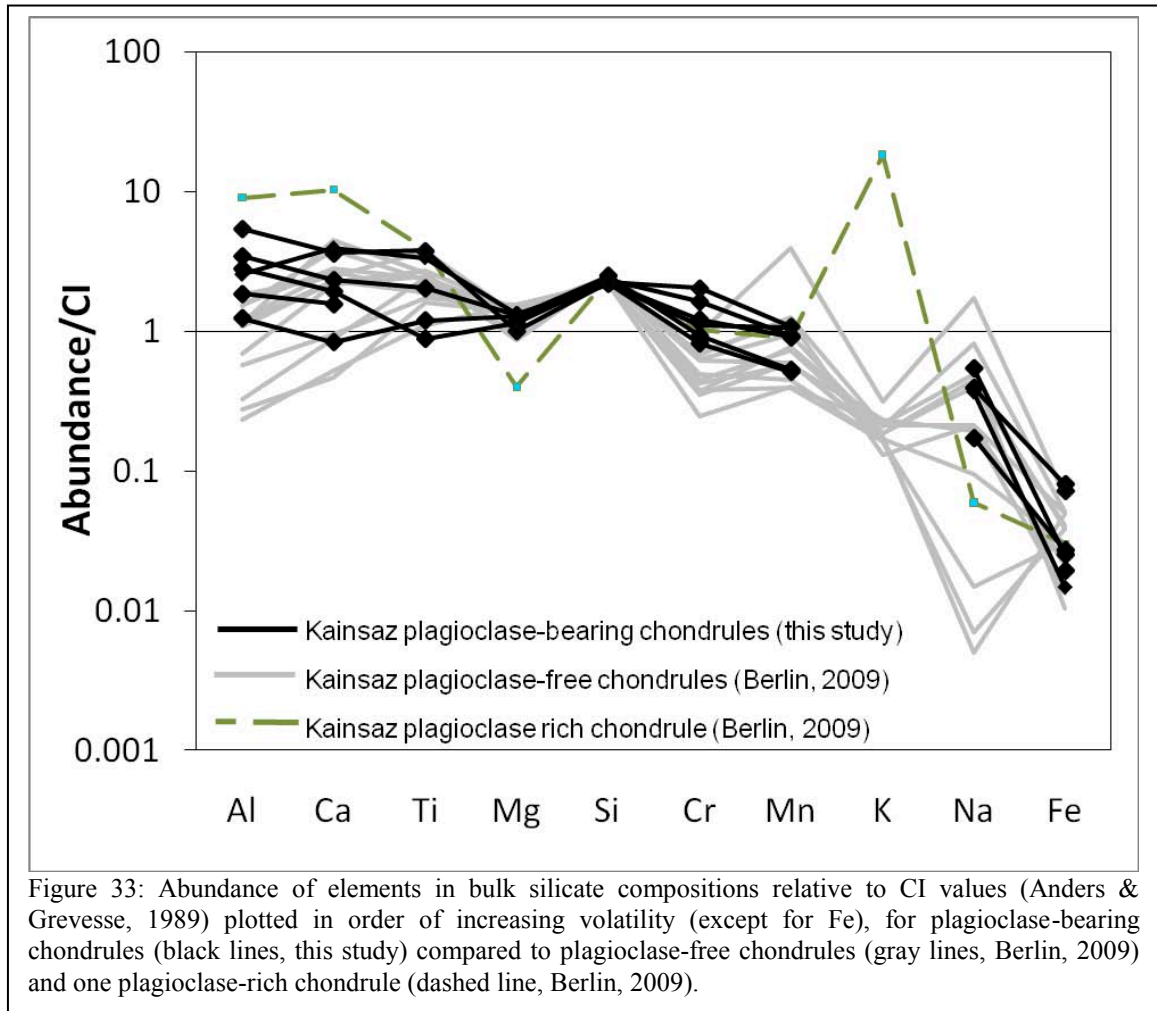
Mineral compositions in plagioclase-bearing type I chondrules are very similar to those in plagioclase-free chondrules. Figures 17 and 18 show that compositions of minor elements in olivine, low-Ca pyroxene, and Ca-pyroxene in type I plagioclase-bearing chondrules fall within the range of variation of plagioclase-free type I chondrules. Thus, the only significant difference between plagioclase-bearing chondrules and plagioclase-free chondrules appears to be that plagioclase-bearing chondrules generally have a bulk composition with a higher Al:Ca ratio than chondrules that have a glassy mesostasis.

73

Experimental reproduction of type I chondrule textures and mineral compositions

Our experiments were run at conditions we considered optimized for plagioclase nucleation: cooling rates of 5°C/hr to 25°C/hr and minimum temperatures as low as 650°C. While they did not produce plagioclase, our experiments contained overall textures that are very similar to the porphyritic textures observed in natural plagioclase-bearing and plagioclase-free type I chondrules. Figure 34 illustrates some of the essential textural similarities of our experiments (all of which had peak temperatures of 1600°C) to natural chondrules. Both experiments and natural chondrules contain a dominant mineral assemblage of olivine, low-Ca pyroxene, and Ca-pyroxene. The experiments also contain a small amount of pyroxene of intermediate composition, probably pigeonite, which we do not commonly observe in chondrules.

A common texture observed in both experiments and natural samples is olivine poikilitically enclosed in low-Ca pyroxene, and Ca-pyroxene overgrowths on low-Ca pyroxene. The range of features observed in the experiments are very similar to the range of textures observed in natural type I chondrules (Figure 34). Although we commonly attribute the range of olivine / pyroxene ratios we observe in natural chondrules to differences in bulk compositions, we also see a range of olivine / pyroxene ratios in our experiments, which all had the same starting composition (see Figure 34). It is possible that due to crystal settling during the experiments, some chemical fractionation may have occurred, leading to differences in chemical compositions in different parts of the experimental charges. As a consequence, the way the chondrules and experiments are sectioned can give slightly variable apparent bulk compositions. Three experiments in

particular had significantly different textures from the rest of the experiments. Exp12

(cooled at 10˚C/hr to 650˚C), exp 14 (cooled at 5˚C/hr to 800˚C, Figure 25), and exp25
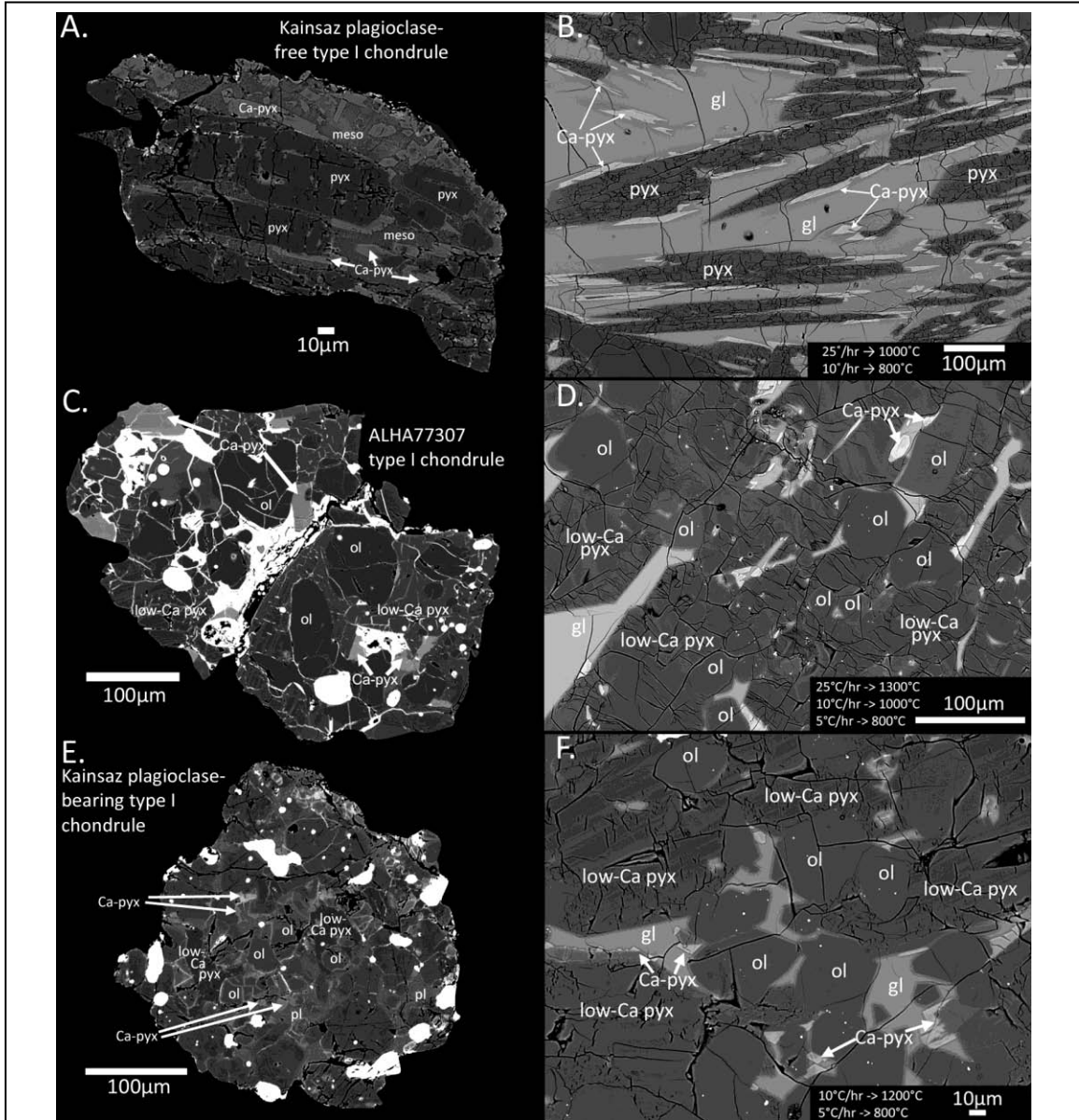
Figure 34: Comparison of textures present in natural type I chondrules (at left) and in slow-cooled experiments (at right). Experiment cooling rates are given in bottom right of each BSE image. (a) Type I plagioclase-free chondrule from Kainsaz (CO3.2), courtesy of Berlin (2009). Chondrule contains large low-Ca pyroxene grains with Ca-pyroxene overgrowths in a glassy mesostasis. (b) Exp7, a slow-cooled experiment containing low-Ca pyroxene and Ca-pyroxene overgrowths. (c) Type I chondrule from ALHA77307 (CO3.0). (d) Exp8, a slow-cooled experiment. (e) Type I plagioclase-bearing chondrule from Kainsaz. (f) Exp10, a slow-cooled experiment. (c,d,e,f) contain olivine poikilitically enclosed within low-Ca pyroxene and Ca-pyroxene overgrowths on low-Ca pyroxene.

(cooled at 25˚C/hr to 800˚C) contained large olivine grains, glass with quench crystals present, and no pyroxene. It is unclear what is controlling the difference between these experiments and the rest of the experiments.

Previous studies have suggested that poikilitic olivine grains in chondrules represent unmelted precursor relict grains (Nagahara, 1983). However, here, we show that poikilitic olivine textures can be produced using a starting material that does not contain crystalline olivine grains. Therefore, we show that poikilitic olivine in natural chondrules does not require incomplete melting and can grow from the melt.

The simplest explanation of the textures observed in chondrules and experiments is that olivine is the liquidus phase, followed by low-Ca pyroxene and then Ca-pyroxene at a late stage. We modeled the equilibrium crystallization of our experimental bulk composition using MELTS software (Ghiorso & Sack, 1995 and Asimow & Ghiorso, 1998). Although MELTS may not be very reliable for the very Mg-rich compositions or the low oxygen fugacities relevant to type I chondrules, it provides a reasonable prediction of crystallization at high temperatures compared to our observations (Figure 35). MELTS predicts a liquidus temperature of 1678°C, olivine on the liquidus, and low-Ca pyroxene crystallization beginning around 1350°C, along with the resorption of olivine. Ca-pyroxene begins to crystallize around 1200°C. Spinel is predicted by MELTS to be present in very low abundance starting around 1525°C, however it was not observed in our experiments. The MELTS model also predicts the appearance of plagioclase at ~1200°C, which was not observed in our experiments. According to the model, the solidus is reached at a temperature of 1180°C. This is quite different from what was

observed in our experiments, which still contain glass even though they were cooled to temperatures as low as 650°C. It is possible that some of the experiments cooled through the glass transition temperature before we quenched them.

Figure 35: MELTS model of grams of phases (total is 100) versus temperature through the crystallization temperature interval for the experiment starting composition.
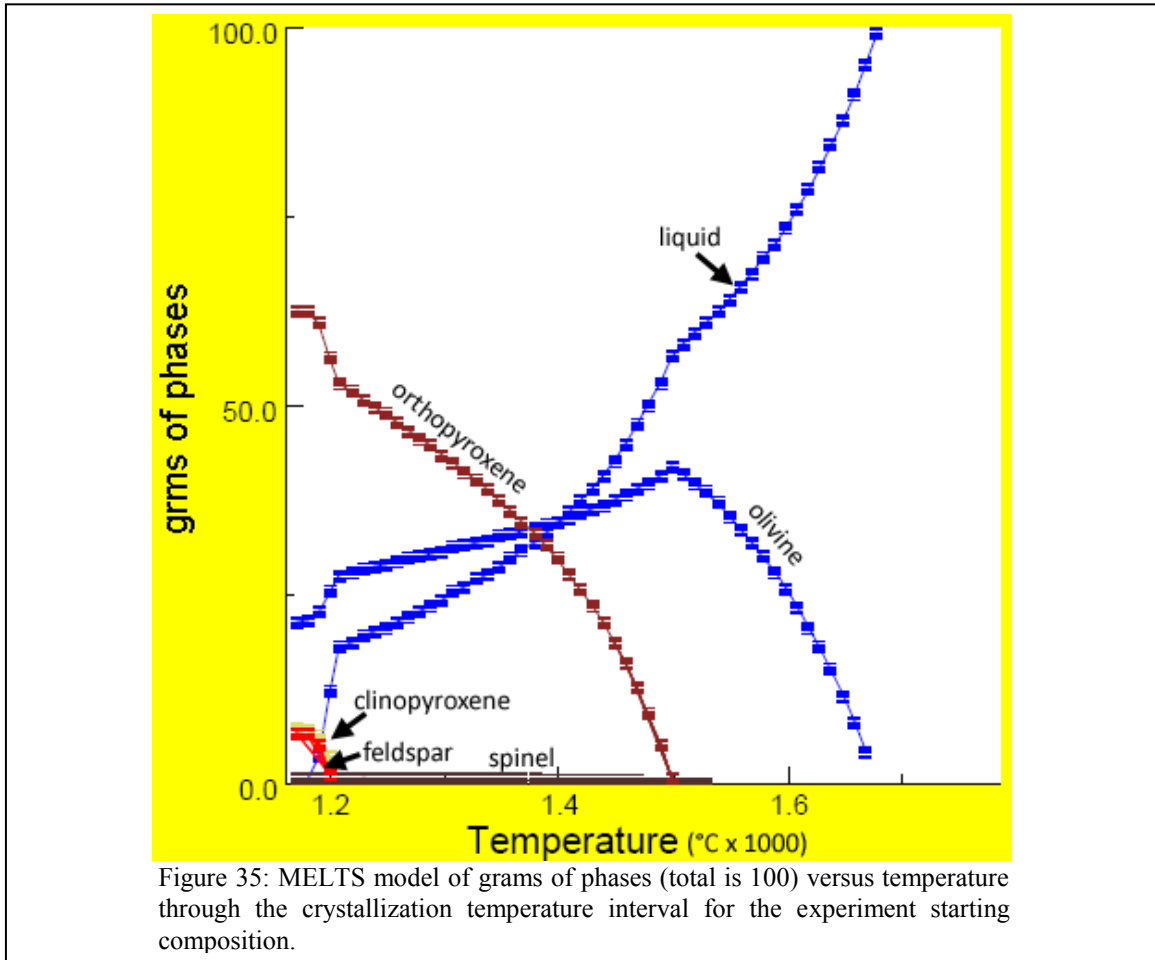
In addition to the experiments with peak temperatures of 1600°C, we also conducted two experiments with peak temperatures of 1500°C. The difference in peak temperature had a large effect on the textures observed. The experiment that was heated to 1500°C for ~10 minutes and then quenched (nexp22, Figure 28) contained numerous small olivine crystals, showing that the charge was probably not completely melted at the onset of cooling. The slow-cooled experiment that had a peak temperature of 1500°C

(nexp21, Figure 29) contained the same dominant mineralogy as the slow-cooled experiments that had a peak temperature of 1600°C. However, the experiments with the lower peak temperature contained more abundant, fine-grained olivine crystals than the experiments with a high peak temperature. This can be attributed to the higher number of nuclei present in the melt at the onset of cooling, due to the lower peak temperature and lower degree of melting. Low-Ca pyroxene occurs as larger, less abundant grains, consistent with nucleation and growth at a later stage in the cooling path. The last phase to crystallize is Ca-pyroxene which grew on low-Ca pyroxene grains just as in experiments with a 1600°C peak temperature.

Some type I chondrules display a texture including large grains of low-Ca pyroxene poikilitically enclosing finer grained olivine grains, analogous to the experiment with the lower peak temperature (1500°C), as illustrated in Figure 36. Other chondrules display a texture containing olivine and low-Ca pyroxene of similar grain size, with olivine poikilitically enclosed in low-Ca pyroxene, more analogous to the experiments conducted with a peak temperature of 1600°C (Figure 34c and d). Hence, we can infer that for short melting times, the peak temperatures experienced by type I chondrules could have ranged from as low as 100°C below the liquidus to super-liquidus temperatures, and that differences in grain size can be related to differences in peak temperatures.

Our experiments at cooling rates of 5 – 25°C/hr produced a range of textures similar to the range of textures observed in type I chondrules. Cooling rates on the order of 5 – 25°C/hr are therefore plausible for the formation conditions of type I chondrules.

78
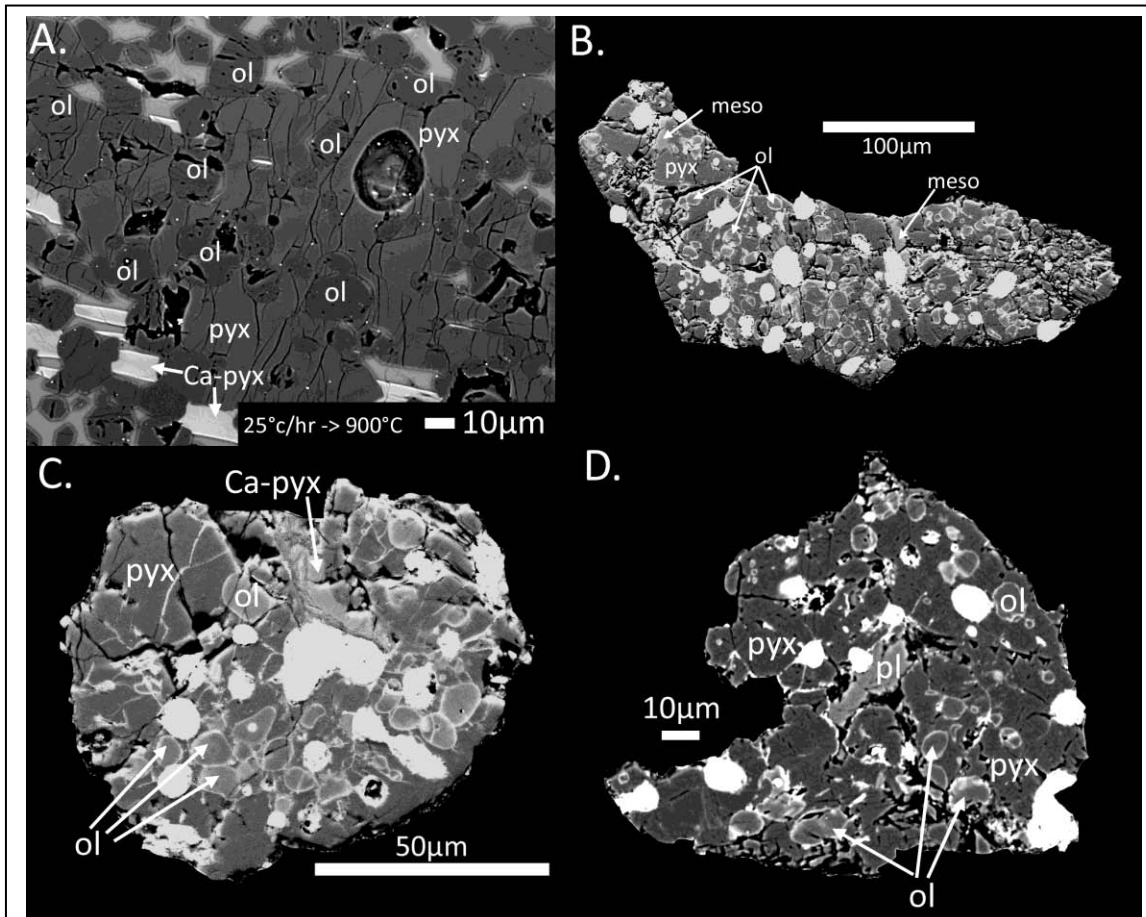
Figure 36: BSE images of nexp21 compared to chondrules. (a) Nexp21, an experiment conducted in the presence of a Na-rich atmosphere, heated to a peak temperature of 1500°C and cooled at 25 °C/hr to quench temperature of 900°C. (b) Plagioclase-free type I chondrule from Kainsaz (CO3.0). (c) Plagioclase-free type I chondrule from Kainsaz. (d) Plagioclase-bearing type I chondrule from Kainsaz. Experiment and natural chondrules both contain coarse-grained low-Ca pyroxene poikilitically enclosing finer grained olivine crystals.

Low-Ca pyroxene in our experiments displays a lamellar texture (Figure 37) that also has been observed in natural type I chondrules (Jones, 2004): pyroxene grains show light and dark streaks in backscattered-electron images. Lamellae are not aligned throughout the sample, and other phases do not display this texture. Compositional zoning within grains was not observed in x-ray maps of streaky pyroxene from experiments, as shown in Figure 38. In many cases, streaks terminate or shift at a small crack normal to the direction of the streaks (e.g. Figure 35). These small cracks are due to

shortening of the c-axis during conversion from the high temperature phase,

protoenstatite, to clinoenstatite twins (e.g. Yasuda et al., 1983). Streaks may be attributed

to twin planes present in clinoenstatite. This texture has not been reported in experiments

previously, and may be useful for constraining chondrule cooling rates if it is only

produced at slow cooling rates like those of our experiments.
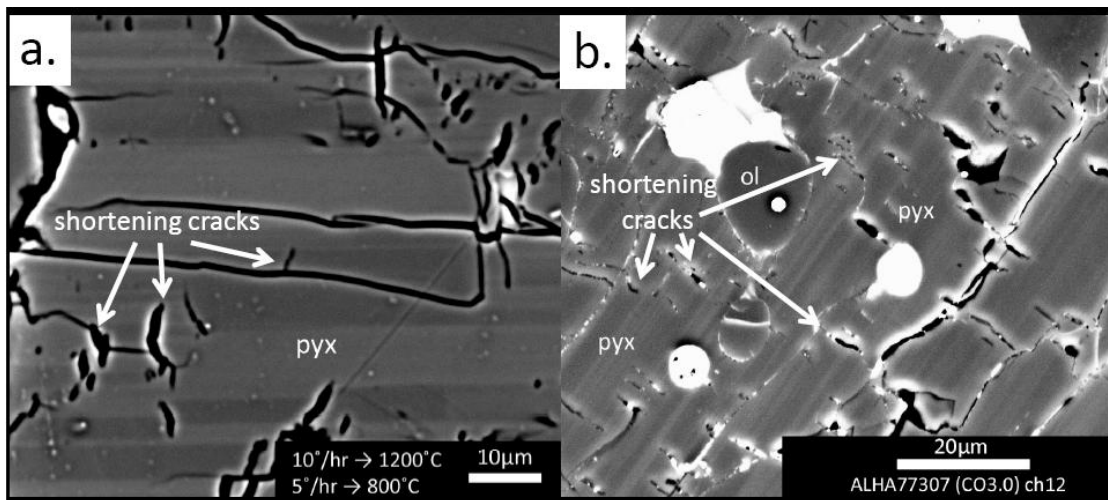
Figure 37: (a) BSE image of "streaky" pyroxene in exp10. Lamellae can be observed in the E-W direction, while shortening cracks are observed in the N-S direction. (b.) BSE of lamellar pyroxene texture in chondrule (ch12) from ALHA77307. Lamellae can be observed in the NE-SW direction, with shortening cracks in the NW-SE direction.
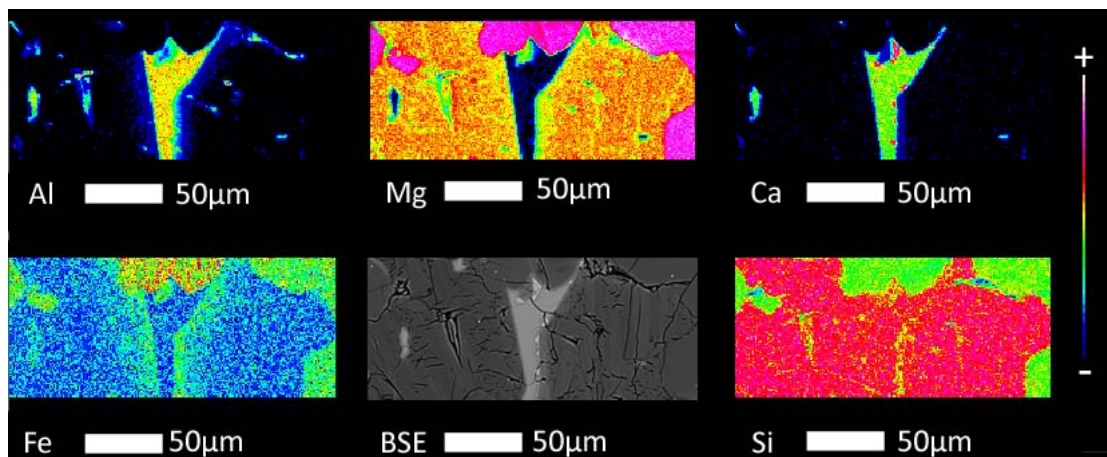
Figure 38: BSE image and major and minor element x-ray maps of low-Ca pyroxene with streaky texture in exp10. No apparent zoning correlates with the streaks in the pyroxene.

In addition to reproducing the textures of natural samples, compositions of minerals produced in our experiments were also very similar to natural plagioclase-bearing and plagioclase-free type I chondrules. Compositions of olivine and low-Ca pyroxene in the experiments with peak temperatures of 1600°C are plotted in Figure 39, where they are compared to Kainsaz plagioclase-bearing and plagioclase-free chondrules (Berlin, 2009), and ALHA77307 (CO3.0 chondrules) (Jones, 1992; Brearley & Jones, 1998; Noguchi, 1989). For olivine, the experiments reproduced the MnO content of type I chondrules well, but the CaO content of the experiments was slightly lower than natural type I chondrules. The source of elevated CaO contents in chondrules is currently debated in the literature, and a consensus has not been reached (Pack & Palme, 2003). Compositions of minor elements Cr_2O_3 and MnO in low-Ca pyroxene from experiments are within the range of natural type I chondrules.

Figure 39 shows minor element variation plots for Ca-pyroxene. For comparison, Kainsaz plagioclase-bearing and plagioclase-free chondrules (Berlin, 2009) are plotted, as well as Semarkona (LL3.0) type I chondrules (Jones & Scott, 1989; Huang, 1996; Matsunami, 1993; Ninagawa, 1992; Jones, 1994). MnO and Cr_2O_3 contents of experimental Ca-pyroxene (Figure 40a and b) are within the range of natural type I chondrule compositions. The Al_2O_3 contents of Ca-rich pyroxene in experiments match plagioclase-free chondrule compositions (Figure 40c). However the, Al_2O_3 contents of Ca-pyroxene in plagioclase-bearing chondrules are significantly lower than plagioclase-free chondrule compositions. This is consistent with igneous plagioclase crystallization because plagioclase takes up Al_2O_3. This also supports our interpretation that the

81

plagioclase in type I chondrules is primary. Previous studies have found that Al_2O_3

content of pyroxenes in basalts increases at faster cooling rates (e.g., Grove and Bence,

1977). This trend has been used to estimate cooling rates experienced by natural samples.

At faster cooling rates, suppression of the plagioclase appearance temperature is larger,

which results in higher concentrations of Al in the melt because it is not being

incorporated into plagioclase. The higher concentration of Al in the melt results in

pyroxene taking up more Al. The Ca-pyroxene compositions in our experiments are very

Al_2O_3 rich and vary significantly. However, even if the upper limit of Ca-pyroxene

compositions in experiments with the same quench temperatures are compared, Al

contents of pyroxenes are not correlated with cooling rates in this series of experiments.

For example, an experiment with a cooling rate of 25°C/hr (exp6) contains Ca-pyroxene

with lower Al_2O_3 contents than an experiment with a cooling rate of 5°C/hr (exp8).

Figure 40d shows Al_2O_3 versus CaO compositions of glass from experiments

compared to mesostasis glass from plagioclase-free chondrules in Kainsaz (Berlin, 2009),

ALHA77307 (Jones, 1992; Brearley & Jones, 1998; Noguchi, 1989), and Semarkona

(Jones & Scott, 1989; Huang, 1996; Matsunami, 1993; Ninagawa, 1992; Jones, 1994).

The composition of glass from experiments is indistinguishable from natural chondrule

mesostasis glass compositions.

Based on textural and compositional similarities between the experiments and

natural chondrules, the range of cooling rates used in these experiments, 5°C/hr to

25°C/hr, is a plausible range for cooling rates experienced by type I chondrules. The

range of 100°C/hr to 1000°C/hr (Radomsky & Hewins, 1990) stated earlier for
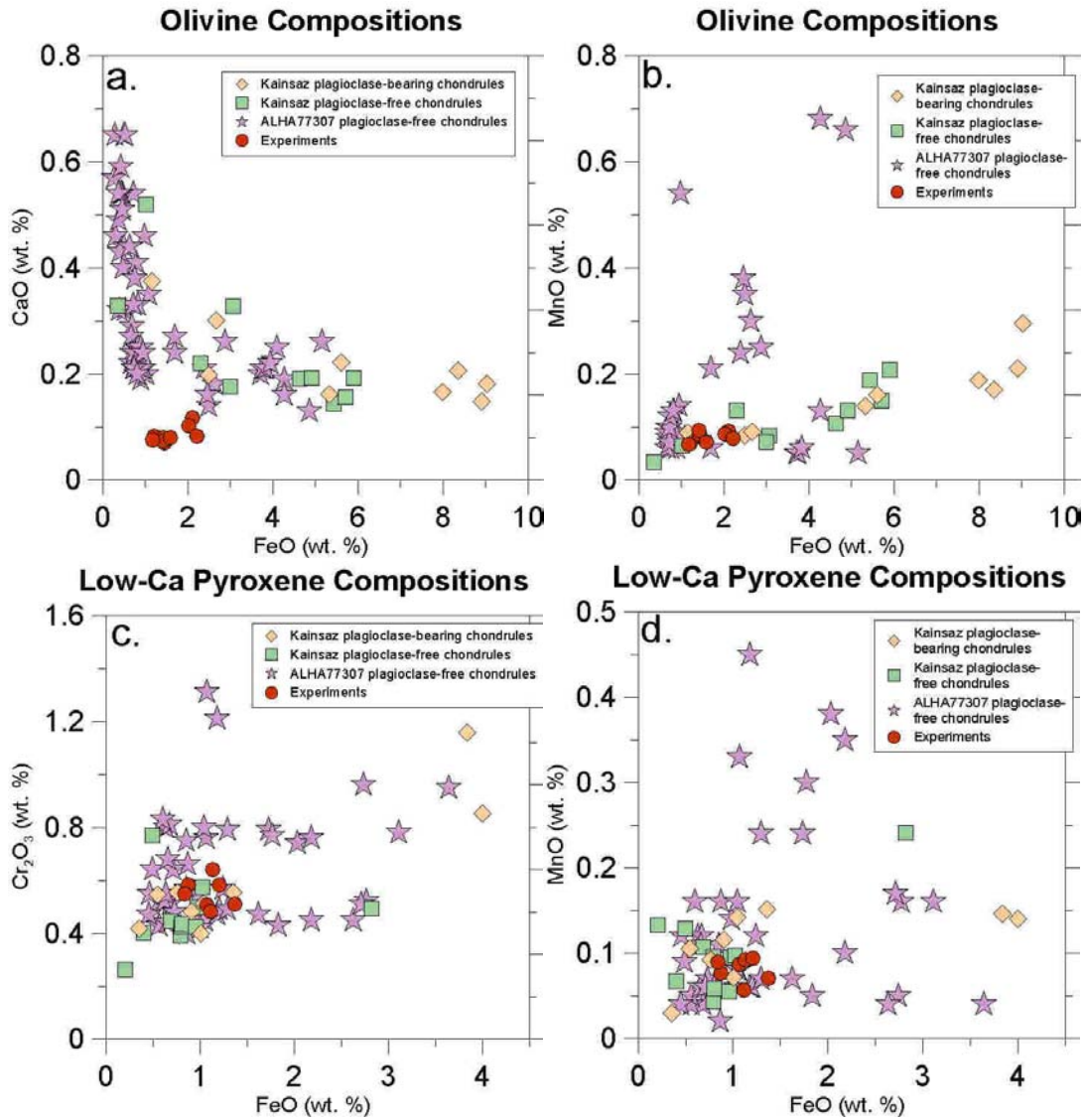
Figure 39: Minor element plots for olivine (a,b) and low-Ca pyroxene (c,d) from experiments. Each circle is the average or representative composition (see Tables 8 – 9) for the phase from one experiment. Plotted for comparison are plagioclase-free chondrules from Kainsaz (Berlin, 2009) and ALHA77307 (Jones, 1992; Brearley & Jones, 1998; Noguchi, 1989).
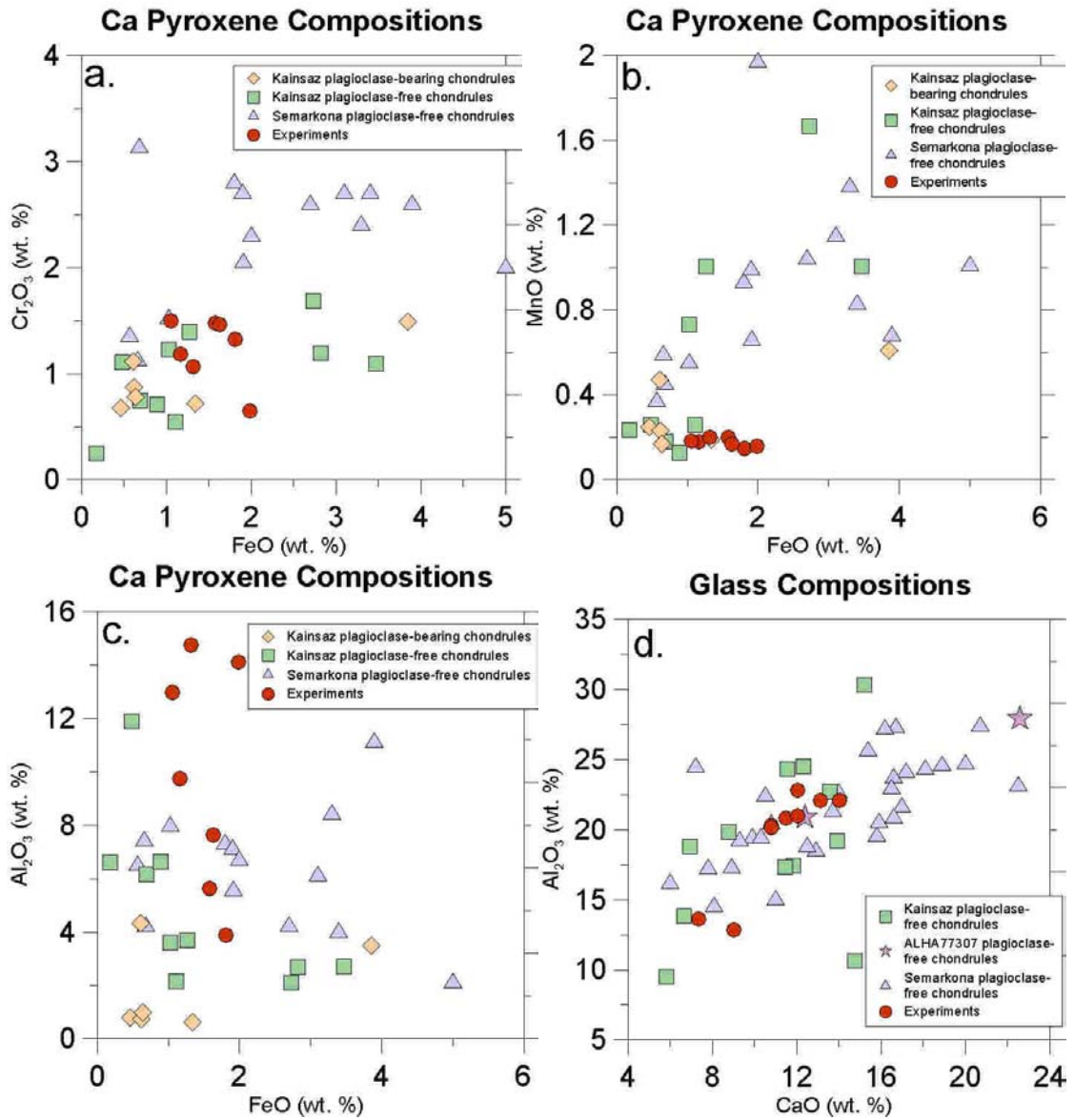
Figure 40: Minor element plots for Ca-pyroxene (a -c) and glass (d) from experiments. Each circle is the average or representative composition (see Tables 11 – 12) for the phase from one experiment. Plotted for comparison are plagioclase-free chondrules from Kainsaz (Berlin, 2009), ALHA77307 (Jones, 1992; Brearley & Jones, 1998; Noguchi, 1989), and Semarkona (LL3.0) (Jones & Scott, 1989; Huang, 1996; Matsunami, 1993; Ninagawa, 1992; Jones, 1994).

84

porphyritic chondrules should be extended to include these slower cooling rates. The majority of our experiments were melted for 18 minutes at 1600°C. Quench experiments indicate complete or nearly complete melting at this temperature. Porphyritic textures were produced, indicating that peak temperatures significantly below the liquidus are not required to produce porphyritic textures at slow cooling rates. We cannot say whether slow cooling rates would allow olivine to nucleate and porphyritic textures to be produced if peak temperatures are above the liquidus.

Occurrence of plagioclase in type I chondrules

The purpose of our experiments was to investigate the conditions required for plagioclase nucleation and growth in type I chondrules. Because homogenous nucleation of plagioclase is known to be kinetically impeded (e.g. Gibb, 1974), we attempted to optimize conditions for plagioclase nucleation by adjusting several parameters. In comparison with previous experiments, we used a plagioclase-bearing type IAB bulk composition, slower cooling rates, and lower quench temperatures. We also ran experiments with a Na-rich atmosphere, and experiments seeded with plagioclase crystals. We discuss these parameters below. Despite investigation of these parameters, we did not observe plagioclase in any experiments. This illustrates that plagioclase nucleation is quite difficult and further illustrates the importance of understanding its crystallization in order to put constraints on the formation of chondrules.

Bulk composition

It is possible that the occurrence of plagioclase depends on the bulk composition of the precursor material. We determined the bulk silicate compositions of six

plagioclase-bearing type I chondrules, and chose a bulk silicate composition intermediate to a PO chondrule and a PP chondrule for our experiments. This type IAB composition is shown relative to plagioclase-bearing chondrules (this study) and plagioclase-free chondrules in Figure 41. While the starting composition did not have an Al:Ca ratio greater than 1, the overall composition of the starting material was within the range of compositions seen in plagioclase-bearing chondrules, and contains elevated values of Al and Cr relative to plagioclase-free chondrules, as is observed in plagioclase-bearing chondrules.

Figure 41: Abundance of elements in bulk silicate compositions (see Table 6) relative to CI values (Anders & Grevesse, 1989) versus elements arranged in order of increasing volatility (except for Fe). The starting composition for our experiments is shown by a black dashed line, and compared to plagioclase-bearing chondrules in dark gray (this study) and plagioclase-free chondrules in light gray (Berlin, 2009) – see also Figure 33.

Slow cooling rates

We tested the hypothesis that slow-cooling a chondrule composition from peak temperatures could facilitate plagioclase nucleation. Previous experiments have been conducted at various cooling rates for the purpose of constraining the formation conditions of a broad range of chondrule textures (e.g. 10-1000°C/hr, Radomsky & Hewins, 1990) However, as plagioclase is a complex tectosilicate, it does not nucleate easily, and we would not expect it to nucleate at fast cooling rates due to kinetic barriers. Therefore, we used only a range of slow cooling rates of 5°C/hr to 25°C/hr for our experiments. Since these rates did not result in plagioclase formation, it is clear that the kinetic barriers to nucleation are indeed significant.

Low quench temperatures

In the slow-cooled experiments, we also cooled the experiments to low quench temperatures. According to the MELTS model for equilibrium crystallization (Ghiorso & Sack, 1995 and Asimow & Ghiorso, 1998), plagioclase is expected to appear at a temperature of 1200°C. However, experimental work on plagioclase nucleation has shown that plagioclase requires a large amount of supercooling to nucleate homogeneously (Gibb, 1974). Previous experiments on a PO chondrule composition cooled to temperatures in the range of 800°C to 1200°C, and annealed for up to one week, did not nucleate plagioclase (Lofgren, 1989). Therefore, to test the possibility that the experiments needed further supercooling in order to nucleate plagioclase, we slow-cooled our experiments to final temperatures as low as 650°C. These experiments contained a

glassy interstitial phase, and no plagioclase. It is possible that the experiments passed through the glass transition while cooling.

Role of sodium

Because our main sequence of experiments, which were cooled slowly to low temperatures, did not produce plagioclase, we decided to investigate the role of Na in plagioclase nucleation. Because Na is a network modifier, increasing its concentration in the melt would increase the NBO/T (non-bridging oxygen over tetrahedral) ratio and de-polymerize the melt, which may facilitate plagioclase nucleation. Glass compositions of our slow-cooled experiments had high SiO_2 contents (55 wt. % to 61 wt. %) and consequently have a very low value of NBO/T of ~0.25. Thus, these melts are highly polymerized. Polymerization of a melt is known to slow diffusion in the melt and thus also slow the nucleation rates, since nucleation depends on the diffusion of required elements to the nucleation (e.g., Henderson et al., 1985)

Natural type I chondrules in CO chondrites can contain up to 10 wt. % Na_2O in the mesostasis (Berlin, 2009). Additionally, plagioclase in plagioclase-bearing type I chondrules has anorthite compositions of An_{75} to An_{83}, which corresponds to 1.8-2.1 wt. % Na_2O in the plagioclase. Because there is very little mesostasis present in these chondrules, the melts from which this plagioclase grew must have contained at least ~2 wt% Na_2O. Clearly, Na was present in the melt, and in turn this requires a mechanism that preserved sodium, normally a moderately volatile element, in the melt.

As discussed previously, experiments have shown that Na can be preserved in silicate melt under oxidizing conditions, at very fast cooling rates, or in a high solid

density environment (e.g., Hewins et al., 2005). In the case of plagioclase-bearing type I chondrules, conditions were clearly not oxidizing, and the porphyritic textures and large plagioclase grains are not likely to have formed at rapid cooling rates. It has been suggested that chondrules formed in regions of high solid densities, based on Na zoning in olivine (Alexander et al., 2008, Borisov et al., 2008). Regions of high solid density could be created by turbulence in the solar nebula. Na is present in the cores of olivine grains, illustrating that it was present at the onset of crystallization at very high temperatures (Alexander et al., 2008). Also, the zoning of Na in olivine grains in type I and type II chondrules correlates with Cr, Mn, and Ca (Alexander et al., 2008). Borisov et al. (2008) also investigated the partition coefficient (K_D) of Na for olivine and melt. An equilibrium partition coefficient is the concentration of an element in the mineral divided by concentration in the melt when a system is at equilibrium, and an apparent K_D is the measured partition coefficient for a system that may or may not be in equilibrium. The apparent K_D for Na in chondrule olivine is in agreement with the experimentally determined equilibrium K_D, indicating that Na was partitioned into olivine during equilibrium crystallization and that Na was not evaporating from the melt during this time (Borisov et al., 2008). In order to prevent Na from evaporating from the chondrule melt at high temperatures, formation in a region of high solid density has been suggested (Alexander, et al., 2008; Borisov et al., 2008). The presence of Na in primary plagioclase in type I chondrules supports this argument.

We ran a set of experiments in the presence of a Na-rich atmosphere in order to preserve Na in the melt, and thus to test the hypothesis that the presence of Na in the melt

during cooling could facilitate plagioclase nucleation (experiments nexp21 and nexp22: see Figures 28 – 29 and Tables 13 – 14). Na_2O was indeed elevated in the residual melt of these experiments relative to the main set of experiments: the glass had a Na_2O content of 4.04 wt. %, compared with values of 0.3 wt. % to 1.8 wt. % Na_2O in experiments where Na was not controlled (Table 12). This abundance is higher than the amount that we predict is needed to crystallize plagioclase with composition An_{75} – An_{85} (2 wt. %), as discussed above. The NBO/T ratio of this melt is 0.17. This value is lower than that of the experiments conducted without the presence of a Na-rich atmosphere, which may be due in part to Fe loss that occurred during the course of the experiment to the Pt foil packet that held the sample. The loss of ~2 wt. % FeO may have an impact on the polymerization of the melt. However, it appears as though the presence of Na_2O in the melt also has more complicated consequences. Figure 42a. shows that experiments with higher glass Na_2O contents also have higher contents of SiO_2 in the glass. As expected, the polymerization of the melt is well correlated with SiO_2 content of the glass (Figure 42b). Therefore, at higher Na_2O contents and thus at higher SiO_2 contents of the glass, NBO/T is very low. Although the presence of 2 wt % FeO in the melt would raise the NBO/T, it appears that the addition of Na to the melt does not simply increase the network modifiers in the melt and increase the NBO/T, it also changes the phase relations and has an effect on the melt composition, which has a more significant effect on the NBO/T value.

Figure 42: Experiment glass compositions are plotted in (a) of Na_2O versus SiO_2 for all experiments except exp12 and exp14, which were left out because their measured SiO_2 contents are not representative of the true glass composition at the time of quenching due to the presence of quench crystals. Boxes indicate main series experiments, while a diamond symbol indicates an experiment conducted in the presence of a Na-rich atmosphere. Na_2O content of melt appears to be correlated with increasing SiO_2 in the melt. Plot (b) shows NBO/T values for experiment glass versus SiO_2 content. Higher NBO/T values are correlated with lower SiO_2 values.

Seeding experiments

The starting material for our experiments was a mixture of oxide powders, therefore there were no preexisting plagioclase nuclei in the mixture. Since plagioclase has a complex network structure it has been suggested that it predominantly undergoes homogeneous nucleation from a silicate melt (e.g. Lofgren, 1983). Since homogeneous nucleation is very slow for the complex plagioclase structure, we decided to investigate whether having anorthite present in the starting material could provide the necessary heterogeneous nucleation sites for plagioclase growth from the melt. We conducted two seeding experiments with ground anorthite added to the starting material (exp24, exp25: see Figures 30 – 31 and Tables 14 – 15). The anorthite added to the starting material had

91

a grain size of ~3μm to ~80μm, which is in agreement with the expected typical grain size of chondrule precursors of ~tens of micrometers across (Hewins et. al., 2005). The anorthite seeds had a composition close to endmember anorthite. This experiment had a similar peak temperature and cooling rate to our main series of experiments. It was melted for 18 minutes at a peak temperature of 1600°C, and then cooled at a rate of 25°C/hr to a minimum temperature of 800°C. No plagioclase was observed in the run product, either as un-melted anorthite (with the starting composition of the seeds) or as melt-grown grains.

It is very likely that all anorthite nuclei were completely dissolved during melting and did not survive to the point when anorthite crystallization was thermodynamically favored. Dissolution rates for anorthitic plagioclase ($An_{52.5}$) in a basaltic melt at 1300°C are 5.657 x 10^{-2}μm/s (Edwards and Russell, 1996). If this value is similar for endmember anorthite in the mafic melt of our experiments, even the largest (~80 μm) crystals would be completely dissolved after 24 minutes at 1300°C. At the cooling rate of 25˚C/hr in this experiment, after heating to 1600˚C, the experiment spent 12 hours above 1300˚C, therefore the anorthite seeds should be long dissolved. Furthermore, no anorthite seeds were observed in the quench experiment, which was melted for just ~1 minute at 1600°C, indicating that they had probably completely dissolved even before cooling began, as the dissolution rate at 1600˚C is likely much higher than at 1300˚C. If the peak temperature of these experiments were lower (for example 1500˚C, as in the Na-rich experiments) perhaps the anorthite seeds could persist in the melt and anorthite would be observed, depending on the true dissolution rate of anorthite in this system. This could be tested in

future experiments. Long melting times at a lower temperature may also destroy anorthite seeds. The mechanism for facilitating plagioclase nucleation during chondrule formation must agree with high peak temperatures. Larger seeds would also persist longer in the melt, however coarser grains would be in disagreement with the predicted grain size for chondrule precursors. Based on the limited number of seeding experiments we conducted, it appears that the addition of seeds to the starting material cannot explain the presence of plagioclase in type I chondrules.

How does primary plagioclase form?

Plagioclase was not produced in chondrule analog experiments by slow cooling, continuous cooling to low temperatures, or by seeding with anorthite crystals in the starting material. The presence of plagioclase in a significant portion of type I chondrules in CO chondrites clearly does not have a simple explanation.

There are several possibilities for future work to constrain plagioclase crystallization conditions. First, it is possible that the cooling rates used in this study were not slow enough. Alternatively, for cooling rates similar to those used in this study, annealing may be required at low temperatures, giving the system extra time to move closer to equilibration and nucleate plagioclase. Further experiments at various slow cooling rates in the presence of a Na-rich atmosphere with an experimental set-up that did not allow Fe-loss would help determine if having a network modifying cation present in the melt helps facilitate plagioclase nucleation. Also, we only performed a limited number of seeding experiments in this study. It is possible that anorthite seed grains of a coarser grain size would be large enough to persist at high degrees of melting and provide

nuclei for plagioclase growth. If plagioclase nucleation still did not occur once these factors are tested, we might consider the role of water in plagioclase nucleation. The presence of water in the system would be expected to lower the NBO/T and allow for higher mobility in the melt, and also lower the liquidus temperature, and this could have a significant effect on plagioclase nucleation. Because formation of chondrules in the presence of a water pressure would be very difficult to explain with current chondrule-forming models, the problem of how plagioclase forms in chondrules is an important question to resolve.

Models for chondrule formation

We can explore how our experimental results compare with current models for chondrule formation. Currently the most prevalent model in the literature for the transient heating event that melted chondrules is the shock wave model (e.g., Desch & Connolly, 2002). A shock wave is a front of hot, compressed high-speed gas that moves through a region of cooler, less dense, slower-moving gas. In this model, chondrule dust-ball precursors encounter a shock front and are heated, compressed, and accelerated very rapidly and then cooled quickly (Connolly & Love, 1998). Potential sources for shock waves include irregular accretion of interstellar gas onto the protoplanetary disk, spiral arm instabilities in the disk, bow shocks from eccentric planetesimals moving at hypersonic speeds through the protoplanetary disk, and gravitational interactions with passing stars (Connolly and Love, 1998, Desch & Connolly, 2002).

While cooling rates of chondrules predicted by the shock wave model are non-linear, we can compare the cooling rates through the temperatures where the majority of

crystallization is occurring to the cooling rates constrained by our experiments. A canonical one-dimensional shock was modeled by Desch & Connolly (2002). The canonical simulation used parameters that are currently accepted for the solar nebula: Chondrules are assumed to make up 75% of the solid mass, and the mass of the solids is 0.005 of the mass of the gas. Chondrules are spherical and have radii of 300μm. The ambient density and temperature of the midplane at 2.5 AU are used: 1×10^{-9} g/cm^3 and 300K, respectively. The shock velocity is 7 km/s. For canonical shock, the shock wave model predicts a peak temperature of 1583°C (1856K), which is similar to the peak temperature of our experiments. The model predicts a cooling rate of between 35°C/hr and 50°C/hr for the temperature interval of 1427°C (1700K) to 1127°C (1400K) (Figure 42). Slower cooling occurs at temperatures below this interval, where plagioclase would be expected to nucleate and grow.

One problem of significance to plagioclase crystallization in the Desch & Connolly (2002) model was that the chondrules cool only through a temperature of 1200˚C. This is due to simplified boundary conditions for post-shock temperatures (Morris & Desch, personal communication). A more recent study (Morris & Desch, currently submitted to Astrophysical Journal) has taken post-shock heat transfer conditions into account, as well as improving several other parameters, including a more accurate calculation of the temperature at which dust effectively evaporates, and a more accurate consideration of the effect of molecular line cooling, or the cooling of a gas by emissions of photons by trace molecules in the gas like CO and H_2O. The canonical case modeled by Morris & Desch (Morris & Desch, currently submitted to Astrophysical

Journal) includes the same conditions described above, except that the shock velocity is 8 km/s, and the total chondrule density is ten times the values used previously. For this canonical case, the predicted cooling rates through the temperature interval of 1427°C (1700K) to 1127°C (1400K) agree well with the results of this study: 15˚C/hr – 45˚C/hr (Figure 43). The peak temperature is slightly higher at 1727˚C (2000K). In this case, at low temperatures, where plagioclase would crystallize, the chondrules continue to cool slowly to lower temperatures.

It is possible for the density of chondrules in the solar nebula to vary, as turbulence could concentrate a higher density of chondrules in certain regions. Desch & Connolly (2002) show that changes in the density of chondrules have a large impact on peak temperatures and cooling rates experienced by chondrules in the post-shock region. For high chondrule densities, chondrules experience higher cooling rates of 100°C/hr and greater. In the model of Morris and Desch (currently submitted to Astrophysical Journal), however, the increase in chondrule cooling rates with chondrule density is less significant, with a cooling rate of 22˚C/hour to 80˚C/hour with a chondrule density 50 times the canonical value. However, more significant is perhaps the change in peak temperature to >2000˚C, effectively evaporating the chondrules, with an increase in chondrule density to 50 times the canonical value. An increase in chondrule density could be important for explaining retention of Na in chondrules, as discussed above (Alexander et al., 2008; Borisov et al., 2008).

Overall, the cooling rates and peak temperatures of our experiments are consistent with predictions of the shock wave model for chondrule formation.
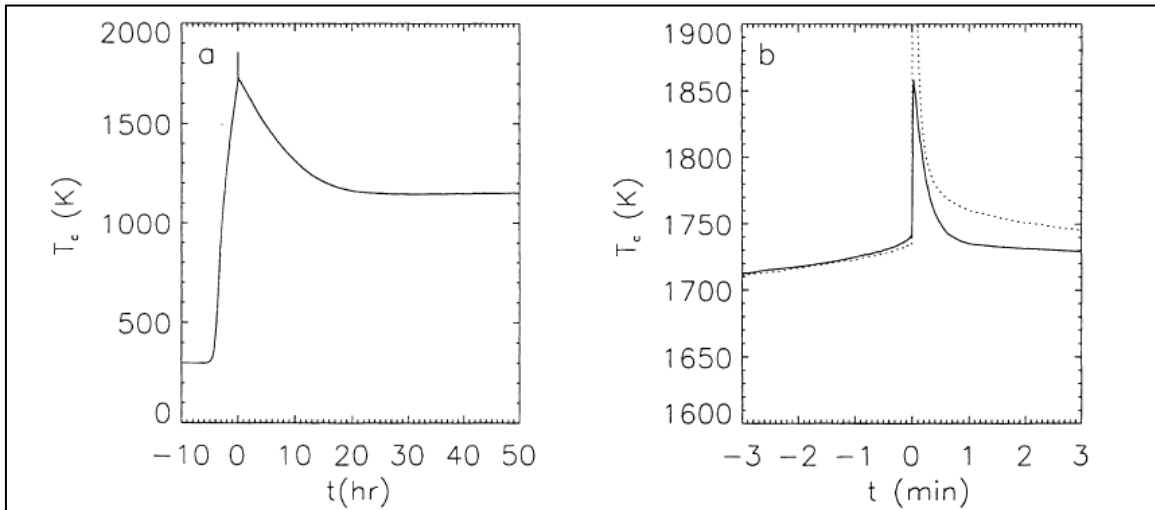
Figure 43: After Desch & Connolly (2002). Thermal history of a chondrule in canonical shock. The chondrule's temperature over the course of hours (solid line) is shown in (a), and over the course of the first few minutes of shock in (b). The dotted line is the temperature of the gas. Chondrules are heated by radiation behind the approaching shock wave before they reach the shock front. Cooling rates are fastest at high temperature and slower through crystallization temperatures.
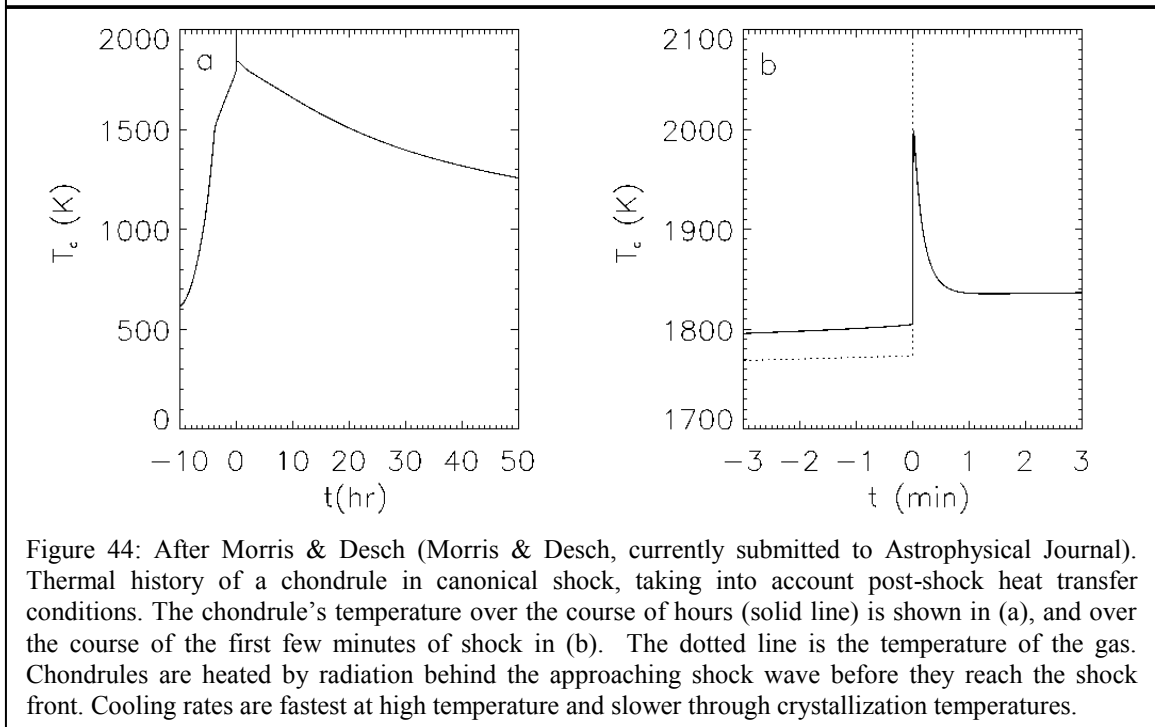
Figure 44: After Morris & Desch (Morris & Desch, currently submitted to Astrophysical Journal). Thermal history of a chondrule in canonical shock, taking into account post-shock heat transfer conditions. The chondrule's temperature over the course of hours (solid line) is shown in (a), and over the course of the first few minutes of shock in (b). The dotted line is the temperature of the gas. Chondrules are heated by radiation behind the approaching shock wave before they reach the shock front. Cooling rates are fastest at high temperature and slower through crystallization temperatures.

Conclusions:

1. Type I chondrules containing plagioclase are not genetically different from most type I chondrules as they contain the same textures, mineral compositions, and very similar bulk compositions regardless of whether the interstitial phase is glass or plagioclase.

2. Experiments conducted at cooling rates of 5°C/hr to 25°C/hr produce charges with textures and compositions analogous to natural porphyritic type I chondrules, therefore the range of cooling rates experienced by chondrules during their formation could extend to as low as 5°C/hr. Low cooling rates are in agreement with predictions of current shock wave models.

3. Peak temperatures in our experiments were 1500°C to 1600°C, close to the liquidus of ~1600°C for the type IAB composition used in this study. Textures produced were very similar to natural chondrule textures; therefore these peak temperatures are also plausible for chondrule formation. Incomplete melting may not be a requirement to produce porphyritic textures in slow-cooled chondrules. Lower peak temperatures relative to the liquidus produced fine-grained olivine poikilitically enclosed in olivine compared to the coarser grained olivine observed when peak temperatures are closer to the liquidus.

4. The presence of Na in plagioclase in type I chondrules supports the suggestion, based on the abundance of Na in olivine, that chondrules formed in a region of high solid density.

5. In our chondrule analog experiments, plagioclase nucleation was not enhanced by factors that are expected to optimize plagioclase nucleation, including slow cooling through low temperatures or having a starting material containing anorthite seeds. The formation conditions required to produce plagioclase-bearing type I chondrules are still unconstrained.

REFERENCES

Alexander C. M. O'D., Grossman J. N., Ebel D. S., and Ciesla F. J. (2008) The Formation conditions of chondrules and chondrites. *Science* 320, 1617 – 1619.

Amelin Y., Krot A. N., Hutcheon I. D., and Ulyanov A. A. (2002) Lead isotopic ages of chondrules and calcium-aluminum-rich inclusions. *Science* 6, 1678 – 1683.

Anders E. and Grevesse N. (1989) Abundances of the elements: Meteoritic and solar. *Geochimica et Cosmochimica* Acta 53, 197 – 214.

Asimow P. D., and Ghiorso M. S. (1998) Algorithmic modifications extending MELTS to calculate subsolidus phase relations. *American Mineralogist* 83, 1127 – 1131.

Berlin J. (2009) Mineralogy and bulk chemistry of chondrules and matrix in petrologic type 3 chondrites: Implications for early solar system processes. Ph.D. thesis, University of New Mexico.

Borisov A., Pack A., Kropf A., and Palme H. (2008) Partitioning of Na between olivine and melt: An experimental study with application to the formation of meteoritic Na_2O-rich chondrule glass and refractory forsterite grains. *Geochimica et Cosmochimica Acta* 72, 5558 – 5573.

Brearley A. J., and Jones R. H. (1998) Chondritic Meteorites. In: *Planetary Materials* (ed. J.J. Papike). Reviews in Mineralogy 36, 3-1 to 3-398.

Chambers J. E. (2004) Planetary accretion in the inner Solar System. *Earth and Planetary Science Letters* 223, 241 – 252.

Chizmadia L., Rubin A. E., and Wasson J. T. (2002) Mineralogy and petrology of amoeboid olivine inclusions in CO3 chondrites: Relationship to parent-body aqueous alteration. *Meteoritics and Planetary Science* 37, 1781 – 1796.

Cohen B. A., Hewins R. H., and Alexander C. M. O'D. (2004) The formation of chondrules by open-system melting of nebular condensates. *Geochimica et Cosmochimica Acta* 68, 1661 – 1675.

Connolly H. C. Jr., and Desch S. J. (2002) A model of the thermal processing of particles in solar nebula shocks: Application to the cooling rates of chondrules. *Meteoritics and Planetary Science* 37, 183 – 207.

Connolly H. C. Jr., and Hewins R. H. (1995) Chondrules as products of dust collisions with totally molten droplets within a dust-rich nebular environment: An experimental investigation. *Geochimica et Cosmochimica Acta* 59, 3231 – 3246.

Connolly H. C. Jr., and Love S. G. (1998) The formation of chondrules: Petrologic tests of the shock wave model. *Science* 3, 62 – 67.

Deer W. A., Howie R. A., and Zussman J. (1992) *An Introduction to the Rock-Forming Minerals*, 2nd Edition. Essex: Pearson Education Limited.

Edgar A. D. (1973) *Experimental Petrology, Basic Principles and Techniques*. London: Oxford University Press.

Edwards B. R., and Russell J. K. (1996) A review and analysis of silicate mineral dissolution experiments in natural silicate melts. *Chemical Geology* 130, 233 – 245.

Ghiorso M. S., and Sack R. O. (1995) Chemical mass transfer in magmatic processes. IV. A revised and internally consistent thermodynamic model for the interpolation and extrapolation of liquid-solid equilibria in magmatic systems at elevated temperatures and pressures. *Contributions to Mineralogy and Petrology* 119, 197 – 212.

Gibb F. G. F. (1974) Supercooling and the crystallization of plagioclase from a basaltic magma. *Mineralogical Magazine* 39, 641 – 653.

Grove T. L., and Bence A. E. (1977) Experimental study of pyroxene-liquid interaction in quartz-normative basalt 15597. *Proceedings of the 8th Lunar Science Conference*, 1549 – 1579.

Grove T. L., and Walker D. (1977) Cooling histories of Apollo 15 quartz-normative basalts. *Proceedings of the 8th Lunar Science Conference*, 1501 – 1520.

Henderson P., Nolan J., Cunningham G. C., and Lowry R. K. (1985) *Contributions to Mineralogy and Petrology* 89, 263 – 272.

Hewins R. H. (1997) Chondrules. *Annual Review of Earth and Planetary Sciences* 25, 61 – 83.

Hewins R. H., Connolly H. C. Jr., Lofgren G. E., and Libourel G. (2005) Experimental constraints on chondrule formation. In *Chondrites and the Protoplanetary Disk* (eds. A. N. Krot, E. R. D. Scott and B. Reipurth). Astron. Soc. Pacific Conference Series 341, 286 – 316 .

Hezel D. (1997) A model for calculating the errors of 2D bulk analysis relative to true 3D bulk composition of an object, with application to chondrules. *Computers and Geosciences* 33, 1162 – 1175.

Huang S., Lu J., Prinz M., Weisberg M. K., Benoit P. H., and Sears D. W. G. (1996) Chondrules: Their diversity and the role of open-system processes during their formation. *Icarus* 122, 316 – 346.

Huss G. R., MacPherson G. J., Wasserburg G. J., Russell S. S., and Srinivasan G. (2001) Aluminum-26 in calcium-aluminum-rich inclusions and chondrules from unequilibrated ordinary chondrites. *Meteoritics and Planetary Science* 36, 975 – 997.

Jones R. H. (1990) Petrology and mineralogy of Type II, FeO-rich chondrules in Semarkona (LL3.0): Origin by closed-system fractional crystallization, with evidence for supercooling. *Geochimica et Cosmochimica Acta* 54, 1785 – 1802.

Jones R. H. (1992) On the relationship between isolated and chondrule olivine grains in the carbonaceous chondrite ALHA77307. *Geochimica et Cosmochimica Acta* 56, 467 – 482.

Jones R. H. (1994) Petrology of FeO-poor, porphyritic pyroxene chondrules in the Semarkona chondrite. *Geochimica et Cosmochimica Acta* 58, 5325 – 5340.

Jones R. H. (1997) Ubiquitous anorthitic plagioclase in type I chondrules in CO3 chondrites: Implications for chondrule formation and parent body metamorphism. *Meteoritics and Planetary Science* 32, A67.

Jones R. H., and Scott E. R. D., (1989) Petrology and thermal history of type IA chondrules in the Semarkona (LL3.0) chondrite. *Proceedings of the 19th Lunar and Planetary Science Conference*, 523 – 536.

Kita N. T., Nagahara H., Togashi S., and Morishita Y. (2000) A short duration of chondrule formation in the solar nebula: Evidence from ^{26}Al in Semarkona ferromagnesian chondrules. *Geochimica et Cosmochimica Acta* 64, 3913 – 3922.

Kleine T., Münker C., Mezger K., and Palme H. (2002) Rapid accretion and early core formation on asteroids and the terrestrial planets from Hf-W chronometry. *Nature* 418, 952 – 955

Kleine T., Mezger K., Palme H., Scherer E., and Münker C. (2005) Early core formation in asteroids and late accretion of chondrite parent bodies: Evidence from ^{182}Hf-^{182}W in CAIs, metal-rich chondrites, and iron meteorites. *Geochimica et Cosmochimica Acta* 69, 5805 – 5818.

Krot A. N., Keil K., Goodrich C. A., Scott E. R. D. and Weisberg M. K. (2003) Classification of meteorites. In *Meteorites, Comets and Planets* (ed. A.M. Davis) Vol. 1,*Treatise on Geochemistry* (eds. H.D. Holland and K.K. Turekian), pp. 83-128. Oxford: Elsevier.

Kunihiro T., Rubin A. E., McKeegan K. D., and Wasson J. T. (2004) Initial ^{26}Al/^{27}Al in carbonaceous-chondrite chondrules: Too little ^{26}Al to melt asteroids. *Geochimica et Cosmochimica Acta* 68, 2947 – 2957.

Lewis R. D., Lofgren G. E., Franzen H. F., and Windom K. E. (1993) The effect of Na vapor on the Na content of chondrules. *Meteoritics* 28, 622 – 628.

Libourel G., Krot A. N., and Tissandier L. (2006) Role of gas-melt interaction during chondrule formation. *Earth and Planetary Science Letters* 251, 232 – 240.

Lofgren G. (1974) An experimental study of plagioclase crystal morphology: Isothermal crystallization. *American Journal of Science* 274, 243 – 273.

Lofgren G. (1983) Effect of heterogeneous nucleation on basaltic textures: A dynamic crystallization study. *Journal of Petrology* 24, 229 – 255.

Lofgren G. (1989), Dynamic crystallization of chondrule melts of porphyritic olivine composition: Textures experimental and natural. *Geochimica et Cosmochimica Acta* 53, 461 – 470.

Maharaj S. V. and Hewins R. H. (1994). Clues to chondrule precursors: An investigation of vesicle formation in experimental chondrules. Geochimica et Cosmochimica Acta 58, 1335 – 1342.

Matsunami S., Ninagawa K., Nishimura S., Kubono N., Yamamoto I., Kohata M., Wada T., Yamashita Y., Lu J., Sears D. W. G., and Nishimura H., (1993) Thermoluminescence and compositional zoning in the mesostasis of a Semarkona group A1 chondrule and new insights into the chondrule-forming process. *Geochimica et Cosmochimica Acta* 57, 2101 – 2110

Nagahara H. (1983) Chondrules formed through incomplete melting of pre-existing mineral clusters and the origin of chondrules. In: *Chondrules and their Origins* (ed: Elbert A. King) 211 – 222.

Ninagawa K., Nishimura S., Kubono N., Yamamoto I., Kohata M., Wada T., Yamashita Y., Lu J., Sears D. W. G., Matsunami S., and Nishimura H. (1992) Thermoluminescence of chondrules in primitive ordinary chondrites, Semarkona and Bishunpur. *Proceedings of the NIPR Symposium on Antarctic Meteorites* 5, 281 – 289.

Noguchi T. (1989) Texture and chemical composition of pyroxenes in chondrules in carbonaceous and unequilibrated ordinary chondrites. *Proceedings of the NIPR Symposium on Antarctic Meteorites* 2, 169 – 199.

Pack A., and Palme H. (2003) Partitioning of Ca and Al between forsterite and silicate melt in dynamic systems with implications for the origin of Ca, Al-rich forsterites in primitive meteorites. *Meteoritics & Planetary Science* 38, 1263 – 1281.

Radomsky P. M. and Hewins R. H. (1990) Formation conditions of pyroxene-olivine and magnesian olivine chondrules. *Geochimica et Cosmochimica Acta* 54, 3475 – 3490.

Scherer P., and Schultz L. (2000) Noble gas record, collisional history and pairing of CV, CO, CK and other carbonaceous chondrites. *Meteoritics and Planetary Science* 35, 145 – 153.

Scott E. R. D. and Jones R. H. (1990) Disentangling nebular and asteroidal features of CO3 carbonaceous chondrite meteorites. *Geochimica et Cosmochimica Acta* 54, 2485 – 2502.

Scott E. R. D., and Krot A. N. (2005) Chondritic meteorites and the high-temperature nebular origins of their components. In *Chondrites and the Protoplanetary Disk* (eds. A. N. Krot, E. R. D. Scott and B. Reipurth). Astron. Soc. Pacific Conference Series 341, 15 – 53.

Tomeoka K., and Itoh D. (2004) Sodium-metasomatism in chondrules in CO3 chondrites: Relationship to parent body thermal metamorphism. *Meteoritics & Planetary Science* 39, 1251 – 1416.

Tronche E., Hewins R. H., and MacPherson G. J. (2007) Formation conditions of aluminum-rich chondrules. *Geochimica et Cosmochimica Acta* 71, 3361 – 3381

Van Schmus W. R., and Wood J. A. (1967). A chemical-petrologic classification for the chondritic meteorites. *Geochimica et Cosmochimica Acta* 31, 747 – 765.

Weisberg M. K., McCoy T. J., and Krot A. N. (2006) Systematics and Evaluation of Meteorite Classification. In *Meteorites and the Early Solar System II.* (eds. Lauretta D. S., & McSween H. Y. Jr.) Tuscon, Arizona: University of Arizona Press.

Yasuda M., Kitamura M., and Morimoto N. (1983) Electron microscopy of clinoenstatite from a boninite and a chondrite. *Physics and Chemistry of Minerals* 9, 192 – 196

Yin Q., Jacobsen S. B., Yamashita K., Blichert-Toft J., Telouk P., and Albarede F. (2002) A short timescale for terrestrial planet formation from Hf-W chronometry of meteorites. *Nature* 418 949 – 952.

Yu Y., Hewins R. H., and Zanda B. (2005) Sodium and sulfur in chondrules: Heating time and cooling curves. In *Chondrites and the Protoplanetary Disk* (eds. A. N. Krot, E. R. D. Scott and B. Reipurth). Astron. Soc. Pacific Conference Series 341, pp. 213 – 219.